

# The subarcsecond mid-infrared view of local active galactic nuclei: II. The mid-infrared–X-ray correlation

D. Asmus,<sup>1,2,3\*</sup> P. Gandhi,<sup>4,5,6</sup> S. F. Hönig,<sup>4,7,8</sup> A. Smette<sup>1</sup> and W. J. Duschl<sup>3,9</sup>

<sup>1</sup>European Southern Observatory, Casilla 19001, Santiago 19, Chile

<sup>2</sup>Max-Planck-Institut für Radioastronomie, Auf dem Hügel 69, 53121 Bonn, Germany

<sup>3</sup>Institut für Theoretische Physik und Astrophysik, Christian-Albrechts-Universität zu Kiel, Leibnizstr. 15, 24098 Kiel, Germany

<sup>4</sup>School of Physics & Astronomy, University of Southampton, Hampshire SO17 1BJ, Southampton, United Kingdom

<sup>5</sup>Department of Physics, Durham University, South Road, Durham, DH1 3LE, United Kingdom

<sup>6</sup>Institute of Space and Astronautical Science (ISAS), Japan, Aerospace Exploration Agency, 3-1-1 Yoshinodai, chuo-ku, Sagami-hara, Kanagawa 252-5210, Japan

<sup>7</sup>Dark Cosmology Center, Niels Bohr Institute, University of Copenhagen, Juliane Maries Vej 30, 2100 Copenhagen, Denmark

<sup>8</sup>UCSB Department of Physics, Broida Hall 93106-9530, Santa Barbara, CA, USA

<sup>9</sup>Steward Observatory, The University of Arizona, 933 N. Cherry Ave, Tucson, AZ 85721, USA

Received July 31, 2015; accepted August 20, 2015

## ABSTRACT

We present an updated mid-infrared (MIR) versus X-ray correlation for the local active galactic nuclei (AGN) population based on the high angular resolution 12 and 18  $\mu\text{m}$  continuum fluxes from the AGN subarcsecond mid-infrared atlas and 2–10 keV and 14–195 keV data collected from the literature. We isolate a sample of 152 objects with reliable AGN nature and multi-epoch X-ray data and minimal MIR contribution from star formation. Although the sample is not homogeneous or complete, we show that our results are unlikely to be affected by significant biases. The MIR–X-ray correlation is nearly linear and within a factor of two independent of the AGN type and the wavebands used. The observed scatter is  $< 0.4$  dex. A possible flattening of the correlation slope at the highest luminosities probed ( $\sim 10^{45}$  erg/s) towards low MIR luminosities for a given X-ray luminosity is indicated but not significant. Unobscured objects have, on average, an MIR–X-ray ratio that is only  $\leq 0.15$  dex higher than that of obscured objects. Objects with intermediate X-ray column densities ( $22 < \log N_{\text{H}} < 23$ ) actually show the highest MIR–X-ray ratio on average. Radio-loud objects show a higher mean MIR–X-ray ratio at low luminosities, while the ratio is lower than average at high luminosities. This may be explained by synchrotron emission from the jet contributing to the MIR at low luminosities and additional X-ray emission at high luminosities. True Seyfert 2 candidates and double AGN do not show any deviation from the general behaviour. Finally, we show that the MIR–X-ray correlation can be used to verify the AGN nature of uncertain objects. Specifically, we give equations that allow to determine the intrinsic 2–10 keV luminosities and column densities for objects with complex X-ray properties to within 0.34 dex. These techniques are applied to the uncertain objects of the remaining AGN MIR atlas, demonstrating the usefulness of the MIR–X-ray correlation as an empirical tool.

**Key words:** galaxies: active – galaxies: Seyfert – infrared: galaxies – X-rays: galaxies

## 1 INTRODUCTION

Supermassive black holes in the centres of galaxy grow through various phases of accretion during the cosmic evolution. During these phases large amounts of radiation are emitted by the infalling material leading to dramatic brightening of the galaxy cores, which are then called active galactic nuclei (AGN). Observing this emission allows us to study the structure of the objects up to the highest redshifts known for galaxies. The primary emission from the hot

gas accretion disk peaks in the ultraviolet (UV) and then is partly reprocessed and reemitted at other wavelengths. In particular, it is commonly assumed that at least in radio-quiet AGN part of the UV is reprocessed in a hot corona above the accretion disk, where the X-ray emission is produced through Compton up-scattering of the UV photons (Haardt & Maraschi 1993). Part of the UV emission from the accretion disk is absorbed by the dust in the material at larger distances (beyond the sublimation radius). This dust reemits the absorbed emission thermally in the infrared. Usually the mid-infrared (MIR) spectra of AGN are dominated by a warm component approximately consistent with a black body of a temperature

\* E-mail: dasmus@eso.org

$\sim 300$  K (e.g., Edelson & Malkan 1986). In total, these processes explain the observed spectral energy distributions (SEDs) of AGN, which often peak in the X-ray and MIR regimes in the  $\nu F_\nu$  units (e.g., Prieto et al. 2010).

Furthermore, the common origin of the MIR and X-ray emission from reprocessed UV emission, lets us expect a correlation between the luminosities at both wavelengths. The exact relation will depend heavily on the structure of obscuring dust. Usually a thick disk or torus-like geometry is assumed for the latter. Such structures introduce an orientation dependence for the obscuration, and we thus expect the MIR emission to be at least mildly anisotropic (Pier & Krolik 1992). Specifically unobscured, type I, objects should have higher MIR luminosities compared to obscured, type II, objects at the same intrinsic power. At the same time, the X-ray emission is likely also anisotropic, depending on the corona geometry (e.g., Liu et al. 2014). Furthermore, the amount of obscuration or opening angle of the torus possibly decreases with increasing accretion disk luminosity because the dust is sublimated, or pushed to larger distances by the radiation pressure. These effects would lead to a decrease of the ratio of the MIR to bolometric luminosity with increasing bolometric luminosity. Finally, in radio-loud objects, a strong jet is present in addition to the other components. The synchrotron emission of this jet might contribute or even dominate both the X-ray emission and the mid-infrared for low accretion rates (e.g., Falcke, Körding & Markoff 2004; Yuan & Cui 2005; Perlman et al. 2007). Therefore, radio-loud objects should behave differently in the MIR–X-ray plane than the radio-quiet objects.

For the reasons mentioned above, measuring the relation between MIR and X-ray emission can constrain the proposed scenarios and reveal information about the structure of the AGN. Apart from the AGN physics, this relation is also relevant for studying the connection between the AGN contributions to the infrared and X-ray cosmological background (e.g., Gandhi & Fabian 2003).

Indeed, a correlation between the MIR and X-ray emission was already found observationally by Elvis et al. (1978) and Glass, Moorwood & Eichendorf (1982) based on ground-based MIR bolometer observations of small sample of local AGN and the first generation of X-ray telescopes. Krabbe, Böker & Maiolino (2001) then remeasured the correlation using one of the first ground-based MIR imagers, MANIAC, mounted on the ESO MPI 2.2 m to obtain nuclear  $N$ -band ( $\sim 10 \mu\text{m}$ ) photometry of a sample of eight nearby AGN. The X-ray fluxes were in the 2–10 keV energy band and absorption corrected, from *ASCA*, *BeppoSAX*, and *Ginga*. Krabbe, Böker & Maiolino attempted to correct for extinction in the MIR, which is possibly significant in many of the Compton-thick (CT) objects. The MIR–X-ray correlation was then investigated with a much larger sample by Lutz et al. (2004) and Ramos Almeida et al. (2007) using low angular resolution MIR data ( $> 1$  arcsec) from *ISO* and 2–10 keV measurements also from *XMM-Newton* and *Chandra*. The former work decomposed the *ISO* spectra to isolate the AGN continuum emission at  $6 \mu\text{m}$ , still a large scatter affected their correlation results as in the latter work. In parallel, a number of other works made use of the now available MIR instruments on eight-meter class telescopes like VISIR and T-ReCS to study the MIR–X-ray correlation at subarcsecond resolution at  $\sim 12 \mu\text{m}$  (Horst et al. 2006, 2008; Gandhi et al. 2009; Levenson et al. 2009; Hönig et al. 2010). Isolating the AGN emission to a much better degree, these works found, in general, a very small scatter in the correlation ( $\sim 0.3$  dex). In particular, Gandhi et al. (2009) demonstrated that even the CT obscured AGN follow the same correlation as the unobscured AGN without large offsets or scatter. This made the

MIR–X-ray correlation the tightest among the other multiple wavelength correlations found for AGN and especially intriguing because of its applicability to all different AGN types. Using *Spitzer*, the correlation was at the same time extended towards higher luminosities (Fiore et al. 2009; Lanzuisi et al. 2009) and shown to be valid even for radio-loud AGN (Hardcastle, Evans & Croston 2009). Further high angular resolution imaging allowed then to extend the correlation into the low-luminosity regime (Asmus et al. 2011; Mason et al. 2012), where some indication was found that radio-loud low-luminosity objects show on average higher MIR–X-ray emission ratios. Finally, with the advent of the X-ray telescopes *Swift* and *INTEGRAL*, sensitive to very hard X-rays, the correlation could be shown to extend also the 14–195 keV X-ray regime (Mullaney et al. 2011; Matsuta et al. 2012; Ichikawa et al. 2012; Sazonov et al. 2012). These works mainly used low angular resolution MIR data from *IRAS*, *Spitzer*, *AKARI*, and *WISE* and could demonstrate that the correlation also extends towards longer wavelengths in the MIR. Mullaney et al. (2011) and Sazonov et al. (2012) applied spectral decomposition to isolate the AGN continuum at 12 and  $15 \mu\text{m}$  respectively. They found rather shallow slopes for the MIR–X-ray correlation in particular at odds with Fiore et al. (2009) and Lanzuisi et al. (2009). In general, the findings of all these works remained inconclusive or contradicting with respect to the predictions of the models described above, owing to either small sample sizes, selection effects or the lack of sufficient angular resolution. Therefore, the correlation needs to be investigated at high angular resolution for a large sample covering the whole luminosity range of AGN.

The first paper of this series (Asmus et al. 2014) presented high angular resolution MIR photometry for a large number of local AGN obtained with ground-based instruments on eight-meter class telescopes. Here, we use this large well suited data set to accurately redetermine the MIR–X-ray correlation and address the still open issues with a detailed analysis.

## 2 DATA ACQUISITION & SAMPLE SELECTION

We start with the total sample from the AGN MIR atlas of 253 objects (Asmus et al. 2014). Note that sample is a combination of a hard X-ray (14–195 keV) selected and a quasi MIR selected sample as explained in Asmus et al. (2014). Thus, this combined sample does not suffer from any obvious (single) bias against highly obscured sources. The fraction of Compton-thick obscured sources is 18 per cent (confirmed plus candidates). We adopt optical classifications, distances (using the same cosmology) and the MIR continuum fluxes at 12 and  $18 \mu\text{m}$ ,  $F^{\text{nuc}}(12 \mu\text{m})$  and  $F^{\text{nuc}}(18 \mu\text{m})$  from Asmus et al. (2014). As done in that work we also divide the various AGN types into the following rough optical groups to facilitate discussion:

- **type I:** Seyferts with broad unpolarised emission lines (includes Sy 1, Sy 1.2, Sy 1.5, Sy 1/1.5 and Sy 1.5/L);
- **NLS1:** (narrow-line Sy 1);
- **type II:** intermediate type Seyferts (includes Sy 1.8, Sy 1.9 and Sy 1.5/2);
- **type II:** Seyferts without broad emission lines (in unpolarised light; includes Sy 1.8/2, Sy 1.9/2 and Sy 2:);
- **LINERs:** low-ionization nuclear emission line regions (includes L, L:);
- **AGN/SB comp:** AGN/starburst composites (includes Cp, Cp:, and L/H; see Yuan, Kewley & Sanders 2010).

Here, for example Sy 1.8/2 means that the object has both Sy 1.8 and Sy 2 classifications in the literature, i.e. the existence of broad emission line components is controversial. Note that different to Asmus et al. (2014), we keep the NLS1 as an individual class. There are four clear NLS1 in the atlas sample (IZw 1, IRAS 13349+2438, Mrk 1239, and NGC 4051).

The MIR continuum fluxes are the unresolved nuclear fluxes extracted from ground-based multi-filter photometry obtained with the instruments VISIR (Lagage et al. 2004), T-ReCS (Telesco et al. 1998), Michelle (Glasse, Atad-Etchedgui & Harris 1997), and COMICS; (Kataza et al. 2000). The angular resolution of these data is of the order of  $0.35''$  or 120 pc for the median sample distance of 72 Mpc at 12  $\mu\text{m}$ .

We collect observed 14–195 keV fluxes,  $F^{\text{obs}}(14\text{--}195\text{ keV})$ , measured with *Swift*/BAT by combining the data of the 54 and 70 month source catalogues with preference for the latter (Cusumano et al. 2010; Baumgartner et al. 2013). Of the 253 AGN, 120 are in the 70 month catalogue, comprising about  $\sim 20$  per cent of all known AGN detected by *Swift*/BAT after 70 months. Six additional sources missing in the 70 month are in the 54 month catalogue (3C 98, ESO 500-34, NGC 4579, PG 0844+349 and UGC 12348). For all 127 sources without any detection in the BAT catalogues, we adopt an upper limit on  $F^{\text{obs}}(14\text{--}195\text{ keV})$  equal to the nominal sensitivity limit of the 70 month catalogue ( $\log F^{\text{obs}}(14\text{--}195\text{ keV}) = -10.87$ ; Baumgartner et al. 2013).

In addition, we search the literature for the 2–10 keV properties of the individual objects using the most recent X-ray observations with satellites like *Chandra*, *XMM-Newton*, *Suzaku*, and *NuSTAR*. In particular, we compile observed and intrinsic 2–10 keV fluxes,  $F^{\text{obs}}(2\text{--}10\text{ keV})$  and  $F^{\text{int}}(2\text{--}10\text{ keV})$ , and hydrogen column densities,  $N_{\text{H}}$  based upon X-ray spectral modelling (compiled in Table 2). In case of multiple measurements, the average of all detections is used, while for multiple upper limits, the lowest upper limit is taken. For 19 objects we analysed in addition archival *Swift*/XRT data (Burrows et al. 2005) as further described in Appendix A. In order to avoid non-AGN contamination, we exclude all objects optically classified as uncertain (38 objects) or AGN/starburst composites (18 objects; see Asmus et al. 2014) and discuss these separately in the Appendices B3 and B2. Of the remaining 197 object from the atlas, no 2–10 keV properties could be collected or computed for three objects (NGC 3166, PKS 1932-46, and UGC 12348), mainly because of the lack of suitable observations. For further 42 objects, the X-ray data turned out to be problematic because of too few counts for reliable analysis, contradicting results ( $> 1$  dex difference in  $L^{\text{int}}(2\text{--}10\text{ keV})$ ), or Compton-thick obscured objects, for which no recent pointed hard X-ray observations with satellites like *XMM-Newton*, *Suzaku* and *NuSTAR* are available. These objects are referred to as "X-ray unreliable". All these unobserved or problematic sources are excluded from the general analysis and are further discussed as a group in Appendix B1 and individually in Appendix B4. This leaves 152 reliable AGN for the general analysis, called the "reliable" sample. It contains 55 type I, 4 NLS1, 14 type II, 58 type III, 19 LINERs, and 2 unclassified (NGC 4992 and NGC 6251; see Asmus et al. 2014). The individual objects and the relevant properties mentioned above are listed in Table 2.

For objects with at least three independent epochs of X-ray data (100 objects), we use the standard deviation (STDDEV) between the individual measurements as uncertainty for  $F^{\text{obs}}(2\text{--}10\text{ keV})$  and  $F^{\text{int}}(2\text{--}10\text{ keV})$  in logarithmic space (similarly for the luminosities). For the other objects, we use the median + STDDEV of all 100 uncertainties above as flux uncertainty

(0.3 dex) unless they are CT obscured, in which case we use 0.6 dex as uncertainty for  $F^{\text{int}}(2\text{--}10\text{ keV})$  (5 objects). Note that 0.3 dex also corresponds to the typical long-term variability found in individual AGN (e.g., McHardy et al. 2004). For the CT objects, we choose 0.6 dex because *a*) individual  $F^{\text{int}}(2\text{--}10\text{ keV})$  estimates easily differ by an order of magnitude in this regime depending on the model used (e.g., Gandhi et al. 2015), and *b*) by this means, the corresponding objects will statistically be weighted only half during the fitting (where included). The values for  $N_{\text{H}}$  and their uncertainties are computed exactly in the same way as the fluxes, and the corresponding median + STDDEV uncertainty is 0.45 dex.

Finally, for all MIR and X-ray bands, we compute the corresponding luminosities under the assumption of isotropic emission.

### 3 METHODS

We measure correlation strengths by using the Spearman rank correlation coefficient,  $\rho_{\text{S}}$ , and the corresponding null-hypothesis probability  $\log p_{\text{S}}$ , applied to the detections of a sample. The correlations are tested in both luminosity and flux space to show how much correlation is artificially introduced by the distance. Furthermore, we compute the partial correlation rank in luminosity space,  $\rho_{\text{p}}$ , which measures the correlation of the residuals of the correlations of the luminosities with the object distance (`p_correlate` in IDL). To measure the functional description of the correlations, we perform linear regression in logarithmic space with the Bayesian based `linmix_err` algorithm and a normal prior distribution (Kelly 2007). We prefer `linmix_err` for this work over the canonical `fitexy` algorithm (Press et al. 1992) because the former can handle upper limits and also takes into account the intrinsic scatter,  $\sigma_{\text{int}}$ , in the sample (see Park et al. 2012 for a thorough comparison of fitting algorithms). In all correlations, we choose the X-ray component as independent variable, which is physically motivated by the fact that the X-ray emission is a more direct proxy of the primary accretion than the MIR emission. Owing to the nature of the sample which originates from a combined indirect MIR and X-ray selection, there is no preference for the choice of independent variable from the statistical point of view. In Sect. 5.1, we further discuss how our results are affected by possible biases and the choice of methods. Furthermore, we use the logarithmic ratio of the MIR over X-ray luminosity,  $R_{\text{X}}^{\text{M}} = \log L_{\text{MIR}} - \log L_{\text{X}}$  and its standard deviation,  $\sigma_{\text{X}}^{\text{M}}$ , to describe the various relations ( $L_{\text{MIR}}$  and  $L_{\text{X}}$  are to be substituted with the corresponding subbands used in that section). Finally, we use the two-sided one-dimensional Kolmogorov-Smirnov (KS) test to quantify the statistical difference in the MIR–X-ray ratio between various subsamples. The test provides a maximum sample difference,  $D_{\text{KS}}$  and a null-hypothesis probability,  $p_{\text{KS}}$ . To better address the robustness of the KS test results, we perform Monte-Carlo resampling with  $10^5$  random draws. Here, we vary the individual MIR–X-ray ratios by a normal distribution with the STDDEV of the individual uncertainties and then perform simple bootstrapping with drawing and replacement (Press et al. 1992). The combination of both allows us to take into account the effects of both measurement uncertainties and sample incompleteness. Apart from the linear regression analysis, non-detections are always excluded from the quantitative analysis. However, the consistency of the corresponding upper limits with the obtained results is discussed where suitable.

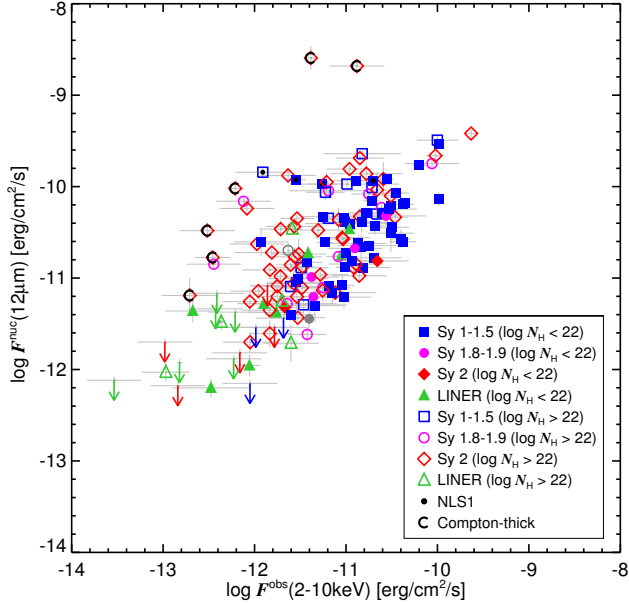


**Figure 1.** Relation of the 12  $\mu\text{m}$  and observed 2-10 keV fluxes for the reliable sample. Blue squares are type I AGN, magenta circles type II, red diamonds type II, green triangles LINERs, and grey filled circles objects without a clear optical type (NGC 4992 and NGC 6251). Filled symbols mark X-ray unabsorbed objects ( $\log N_{\text{H}} \leq 22$ ) while empty symbols are the obscured ones. The arrows mark upper limits of MIR non-detections. Objects marked with a small black filled circle are NLS1 and objects marked with a C are Compton-thick obscured.

## 4 RESULTS

In the following, the relations between the MIR and X-ray emission of the reliable sample are investigated in the four different wavelength ranges, 12  $\mu\text{m}$ , 18  $\mu\text{m}$ , 2-10 keV and 14-195 keV.

### 4.1 12 $\mu\text{m}$ –2-10 keV correlation

Figs. 1 and 2 show the relation of the observed 12  $\mu\text{m}$  and 2-10 keV bands in flux and luminosity space respectively. As expected from previous works, a significant correlation is present between  $F^{\text{nuc}}(12 \mu\text{m})$  and  $F^{\text{obs}}(2-10 \text{ keV})$ . The Spearman rank correlation coefficient for all detected sources is  $\rho_S = 0.59$  and the null-hypothesis probability  $\log p_S = -13.7$  with highly obscured objects introducing large scatter towards high MIR–X-ray ratios (standard deviation  $\sigma_X^M = 0.57$ ). In particular, most of the CT objects exhibit large offsets owing to their strong suppression in X-rays. Interestingly, three of the four NLS1 also exhibit high MIR–X-ray ratios despite low obscuration. We come back to this observation in Section 4.4. If one only regards the 68 X-ray unabsorbed AGN of the reliable sample ( $\log N_{\text{H}} \leq 22$ ), the correlation strength increases to  $\rho_S = 0.77$  and  $\log p_S = -13.5$ . A corresponding linear regression of the unabsorbed sources yields  $\log F^{\text{nuc}}(12 \mu\text{m}) \propto (0.79 \pm 0.08) \log F^{\text{obs}}(2-10 \text{ keV})$  with `linmix_err`. The detailed fitting results are given in Table 1. In luminosity space (Fig. 2), the sample is spread over seven orders of magnitude leading to a formally stronger correlation ( $\rho_S = 0.94$  and  $\log p_S = -27.8$  for the unabsorbed AGN). The partial correlation rank is  $\rho_p = 0.73$  for the unabsorbed AGN, showing that the correlation strength is not dominated by the effect of the distance.

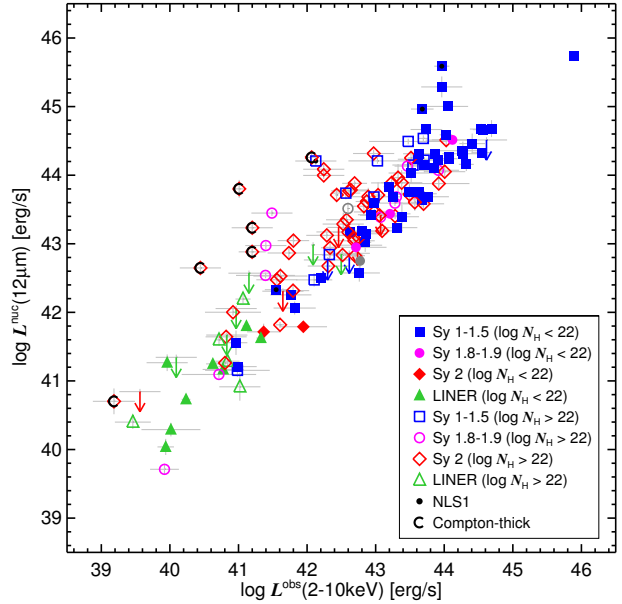


**Figure 2.** Relation of the nuclear 12  $\mu\text{m}$  and observed 2-10 keV luminosities for the reliable sample. Symbols and colours are as in Fig. 1.

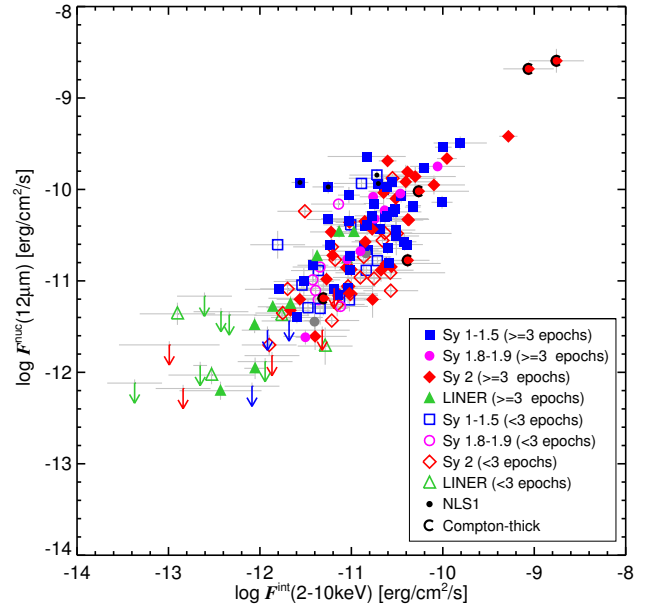


**Figure 3.** Relation of the nuclear 12  $\mu\text{m}$  and intrinsic 2-10 keV fluxes for the reliable sample. Symbols and colours are as in Fig. 1 apart from the filled symbols which here mark objects with at least three epochs of 2-10 keV data.

Owing to the absorption corrections available for the 2-10 keV emission of the reliable objects, we can also investigate the correlation of  $F^{\text{nuc}}(12 \mu\text{m})$  and  $L^{\text{nuc}}(12 \mu\text{m})$  with the intrinsic X-ray fluxes and luminosities,  $F^{\text{int}}(2-10 \text{ keV})$  and  $L^{\text{int}}(2-10 \text{ keV})$ , shown in Figs. 3 and 4. As expected the correlation strength increases in flux space when using an absorption correction for the X-rays ( $\rho_S = 0.73$  and  $\log p_S = -23.2$  for all 152 reliable AGN), and the slope of the linear fit is  $1.02 \pm 0.06$ . Note that two of the

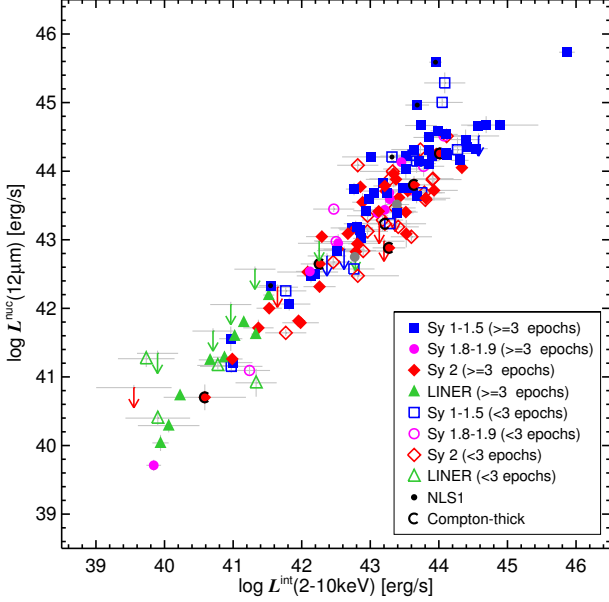


**Figure 4.** Relation of the nuclear 12  $\mu\text{m}$  and intrinsic 2–10 keV luminosities for the reliable sample. Symbols and colours are as in Fig. 3.

NLS1 are still outliers (IZw 1 and IRAS 13349+2438). In luminosity space, the partial correlation rank increases to 0.79 and the slope remains consistent at  $0.98 \pm 0.03$  (Table 1). The observed scatter is  $\sigma_X^M = 0.39$  dex, while the intrinsic scatter is smaller,  $\sigma_{\text{int}} = 0.33$  dex.

Many AGN show significant variability in the 2–10 keV band, while any MIR variability appears to be much weaker and only occurs on much longer time scales (Neugebauer & Matthews 1999; Asmus et al. 2014). Therefore, one would expect a further decrease in the scatter of the correlation when regarding only those 100 AGN for which our  $L^{\text{int}}(2\text{--}10\text{ keV})$  value is based on at least three epochs of X-ray observations in the last decade. For this subsample, the partial correlation rank indeed increases ( $\rho_p = 0.83$ ) and the observed scatter in the  $L^{\text{nuc}}(12\ \mu\text{m})/L^{\text{int}}(2\text{--}10\text{ keV})$  ratio decreases ( $\sigma_X^M = 0.35$  dex). However, the intrinsic scatter estimate stays the same ( $\sigma_{\text{int}} = 0.32$  dex). The similarity of observed and intrinsic scatter indicate that the former is dominated by the latter. The corresponding fit represents the best estimate of the “true” 12  $\mu\text{m}$ –2–10 keV correlation so far:

$$\log\left(\frac{L^{\text{nuc}}(12\ \mu\text{m})}{10^{43}\text{ erg s}^{-1}}\right) = (0.33 \pm 0.04) + (0.97 \pm 0.03) \log\left(\frac{L^{\text{int}}(2\text{--}10\text{ keV})}{10^{43}\text{ erg s}^{-1}}\right). \quad (1)$$

For comparison purposes, in Fig. 5, we also show the 12  $\mu\text{m}$ –2–10 keV relation when using low angular resolution MIR data, here 12  $\mu\text{m}$  luminosities,  $L^{\text{tot}}(12\ \mu\text{m})$ , obtained with the *IRAS* satellite (Neugebauer et al. 1984), which correspond rather to the total emission of the galaxies than the nuclear emission. The corresponding data were collected in Asmus et al. (2014) from the literature, mainly from NED (<http://ned.ipac.caltech.edu>), Sanders et al. (2003), Golombek, Miley & Neugebauer (1988), Rush, Malkan & Spinoglio (1993), Rice et al. (1988) and Sanders & Mirabel (1996). The resulting luminosity correlation has a significantly higher observed scatter ( $\sigma_X^M = 0.65$ ) and the fitted slope is also much flatter ( $b = 0.63$ ). This is obviously caused by host

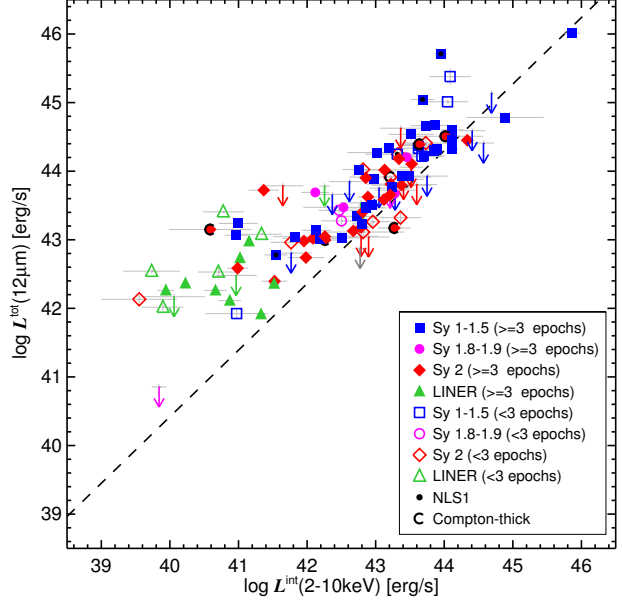


**Figure 5.** Relation of the total 12  $\mu\text{m}$  (*IRAS*) and intrinsic 2–10 keV luminosities for the reliable sample. Symbols and colours are as in Fig. 3. In addition, the dashed line shows the correlation for all reliable objects with multi-epoch X-ray data (Eq. 1).

emission dominating the total MIR emission in many objects up to luminosities of  $\approx 10^{44}$  erg/s (Asmus et al. 2014). But even if one fits only the higher luminosity part of the population ( $> 10^{43}$  erg/s), the slope is still flatter compared to the high angular resolution data ( $b = 0.82$ ). Therefore,  $L^{\text{int}}(2\text{--}10\text{ keV})$  estimates based on MIR luminosities that include the entire galaxy are very unreliable.

## 4.2 MIR–X-ray correlation using 18 $\mu\text{m}$ or 14–195 keV

The AGN MIR atlas also contains nuclear 18  $\mu\text{m}$  flux measurements for 38 of the reliable AGN. This wavelength region has two advantages compared to the 12  $\mu\text{m}$  region, it is even less affected by obscuration and it contains the MIR emission peak of most AGN in  $\nu F_\nu$ , in particular type 1 sources (e.g., Asmus et al. 2014). Note however that at this wavelength, the subarcsecond resolution is even more important to isolate the AGN from the host emission which is stronger at 18  $\mu\text{m}$  than at 12  $\mu\text{m}$ . We plot the corresponding 18  $\mu\text{m}$ –2–10 keV relations in flux and luminosity space in Figs. 6 and 7. Despite the lower object number and coverage in orders of magnitude, the correlation is surprisingly strong already in flux space ( $\rho_S = 0.83$  and  $\log p_S = -9.8$ ). The slope of the correlation is flatter compared to that with the 12  $\mu\text{m}$  band,  $\log F^{\text{nuc}}(18\ \mu\text{m}) \propto (0.88 \pm 0.07) \log F^{\text{int}}(2\text{--}10\text{ keV})$ . In luminosity space, the partial correlation rank is higher than for using 12  $\mu\text{m}$  ( $\rho_p = 0.90$ ) while the observed and intrinsic scatter measures are smaller ( $\sigma_X^M = 0.3$  and  $\sigma_{\text{int}} = 0.25$ ). Thus, the correlation appears to be significantly tighter for 18  $\mu\text{m}$  compared to 12  $\mu\text{m}$ . However, this is just a selection effect because the scatter becomes as small for 12  $\mu\text{m}$  if exactly the same objects are used as for the 18  $\mu\text{m}$  analysis. Note that the slope of the linear fit is higher than in flux space and consistent with the 12  $\mu\text{m}$ -based fitted slopes,  $\log L^{\text{nuc}}(18\ \mu\text{m}) \propto (1.00 \pm 0.05) \log L^{\text{int}}(2\text{--}10\text{ keV})$ .

Instead of using the substantially absorption-affected 2–10 keV energy range, one can now use the 14–195 keV long-term

**Table 1.** Correlation properties.

$X$ (1)	$Y$ (2)	Sample (3)	$N$ (4)	$\rho$ (5)	$a$ (6)	$b$ (7)	$\overline{R_X^M}$ (8)	$\sigma_X^M$ (9)	$\sigma_{\text{int}}$ (10)
$F^{\text{obs}}(2\text{-}10\text{ keV})$	$F^{\text{nuc}}(12\ \mu\text{m})$	$\log N_{\text{H}} \leq 22$	68	0.77	$0.35 \pm 0.05$	$0.79 \pm 0.08$	0.40	0.42	$0.34 \pm 0.16$
$L^{\text{obs}}(2\text{-}10\text{ keV})$	$L^{\text{nuc}}(12\ \mu\text{m})$	$\log N_{\text{H}} \leq 22$	68	0.73	$0.34 \pm 0.05$	$0.96 \pm 0.04$	0.36	0.39	$0.35 \pm 0.18$
$F^{\text{int}}(2\text{-}10\text{ keV})$	$F^{\text{nuc}}(12\ \mu\text{m})$	All (reliable)	152	0.73	$0.29 \pm 0.03$	$1.02 \pm 0.06$	0.32	0.39	$0.33 \pm 0.14$
$L^{\text{int}}(2\text{-}10\text{ keV})$	$L^{\text{nuc}}(12\ \mu\text{m})$	All (reliable)	152	0.79	$0.30 \pm 0.03$	$0.98 \pm 0.03$	0.32	0.39	$0.33 \pm 0.14$
$F^{\text{int}}(2\text{-}10\text{ keV})$	$F^{\text{nuc}}(12\ \mu\text{m})$	$N(\text{X-ray epochs}) \geq 3$	100	0.73	$0.34 \pm 0.04$	$0.94 \pm 0.07$	0.33	0.35	$0.32 \pm 0.14$
$L^{\text{int}}(2\text{-}10\text{ keV})$	$L^{\text{nuc}}(12\ \mu\text{m})$	$N(\text{X-ray epochs}) \geq 3$	100	0.83	$0.33 \pm 0.04$	$0.97 \pm 0.03$	0.33	0.35	$0.32 \pm 0.14$
$L^{\text{int}}(2\text{-}10\text{ keV})$	$L^{\text{tot}}(12\ \mu\text{m})$	<i>IRAS</i>	116	0.57	$0.72 \pm 0.05$	$0.63 \pm 0.04$	0.97	0.65	$0.45 \pm 0.19$
$L^{\text{int}}(2\text{-}10\text{ keV})$	$L^{\text{tot}}(12\ \mu\text{m})$	<i>IRAS</i> & $\log L^{\text{int}}(2\text{-}10\text{ keV}) > 43$	53	0.48	$0.64 \pm 0.12$	$0.82 \pm 0.14$	0.64	0.39	$0.43 \pm 0.24$
$F^{\text{int}}(2\text{-}10\text{ keV})$	$F^{\text{nuc}}(12\ \mu\text{m})$	$18\ \mu\text{m}$	38	0.83	$0.75 \pm 0.05$	$0.88 \pm 0.07$	0.69	0.30	$0.23 \pm 0.14$
$L^{\text{int}}(2\text{-}10\text{ keV})$	$L^{\text{nuc}}(18\ \mu\text{m})$	$18\ \mu\text{m}$	38	0.90	$0.53 \pm 0.06$	$1.00 \pm 0.05$	0.51	0.30	$0.25 \pm 0.16$
$L^{\text{int}}(2\text{-}10\text{ keV})$	$L^{\text{nuc}}(12\ \mu\text{m})$	$18\ \mu\text{m}$	38	0.90	$0.42 \pm 0.06$	$0.99 \pm 0.05$	0.38	0.31	$0.23 \pm 0.15$
$F^{\text{obs}}(14\text{-}195\text{ keV})$	$F^{\text{nuc}}(12\ \mu\text{m})$	$14\text{-}195\text{ keV}$ & $\log N_{\text{H}} < 23.7$	101	0.62	$-0.10 \pm 0.08$	$0.82 \pm 0.10$	-0.19	0.41	$0.40 \pm 0.16$
$L^{\text{obs}}(14\text{-}195\text{ keV})$	$L^{\text{nuc}}(12\ \mu\text{m})$	$14\text{-}195\text{ keV}$ & $\log N_{\text{H}} < 23.7$	101	0.62	$-0.15 \pm 0.05$	$0.91 \pm 0.04$	-0.19	0.41	$0.39 \pm 0.16$
$L^{\text{int}}(2\text{-}10\text{ keV})$	$L^{\text{obs}}(14\text{-}195\text{ keV})$	$14\text{-}195\text{ keV}$ & $\log N_{\text{H}} < 23.7$	101	0.85	$0.47 \pm 0.03$	$1.01 \pm 0.02$	0.47	0.23	$0.17 \pm 0.09$
$L^{\text{int}}(2\text{-}10\text{ keV})$	$L^{\text{nuc}}(12\ \mu\text{m})$	Type I	54	0.70	$0.35 \pm 0.05$	$0.96 \pm 0.05$	0.35	0.34	$0.25 \pm 0.15$
$L^{\text{int}}(2\text{-}10\text{ keV})$	$L^{\text{nuc}}(12\ \mu\text{m})$	Type II	58	0.75	$0.18 \pm 0.06$	$0.97 \pm 0.07$	0.19	0.37	$0.31 \pm 0.18$
$L^{\text{int}}(2\text{-}10\text{ keV})$	$L^{\text{nuc}}(12\ \mu\text{m})$	Type I+II	112	0.74	$0.26 \pm 0.04$	$0.99 \pm 0.04$	0.27	0.36	$0.29 \pm 0.14$
$L^{\text{int}}(2\text{-}10\text{ keV})$	$L^{\text{nuc}}(12\ \mu\text{m})$	<i>LINER</i>	19	0.71	$0.22 \pm 0.44$	$0.92 \pm 0.19$	0.46	0.43	$0.30 \pm 0.31$
$L^{\text{int}}(2\text{-}10\text{ keV})$	$L^{\text{nuc}}(12\ \mu\text{m})$	$\log N_{\text{H}} < 22$	63	0.79	$0.30 \pm 0.04$	$0.95 \pm 0.03$	0.32	0.35	$0.22 \pm 0.14$
$L^{\text{int}}(2\text{-}10\text{ keV})$	$L^{\text{nuc}}(12\ \mu\text{m})$	$22 \leq \log N_{\text{H}} < 23$	32	0.88	$0.43 \pm 0.07$	$1.09 \pm 0.06$	0.36	0.31	$0.23 \pm 0.17$
$L^{\text{int}}(2\text{-}10\text{ keV})$	$L^{\text{nuc}}(12\ \mu\text{m})$	$\log N_{\text{H}} \geq 23$	52	0.77	$0.20 \pm 0.07$	$1.00 \pm 0.09$	0.23	0.41	$0.37 \pm 0.22$
$L^{\text{int}}(2\text{-}10\text{ keV})$	$L^{\text{nuc}}(12\ \mu\text{m})$	Radio-quiet	41	0.88	$0.27 \pm 0.05$	$1.01 \pm 0.05$	0.26	0.28	$0.21 \pm 0.14$
$L^{\text{int}}(2\text{-}10\text{ keV})$	$L^{\text{nuc}}(12\ \mu\text{m})$	Radio-loud	48	0.83	$0.20 \pm 0.06$	$0.90 \pm 0.04$	0.28	0.41	$0.28 \pm 0.17$
$L^{\text{int}}(2\text{-}10\text{ keV})$	$L^{\text{nuc}}(12\ \mu\text{m})$	<i>BAT9</i>	80	0.74	$0.23 \pm 0.04$	$1.02 \pm 0.05$	0.21	0.32	$0.24 \pm 0.13$

– Notes: (1) and (2) the quantities, of which the correlation is measured; (3) sample used for the `linmix_err` fitting; (4)  $N$ : number of objects used for the analysis; (5)  $\rho$ : linear correlation coefficient (Spearman rank  $\rho_S$  for fluxes and partial correlation rank  $\rho_P$  for luminosities); (6) and (7)  $a, b$ : fitting parameters of  $\log(Y) - c = a + b(\log(X) - c)$  with  $c$  being -11 for fluxes and 43 for luminosities; (8)  $\langle R_X^M \rangle$ : average of the ratio  $R_X^M$  with (9)  $\sigma_X^M$  its standard deviation; (10)  $\sigma_{\text{int}}$ : intrinsic scatter (from `linmix_err`).

data obtained with *Swift*/BAT over the last years, which is available for 118 of the 152 reliable AGN. This energy range is less affected by absorption, and the data are also less prone to variability because they are long-term averages. The relation of the observed 14-195 keV to 12  $\mu\text{m}$  fluxes and luminosities is shown in Figs. 8 and 9 respectively. Similar to the 2-10 keV band, a correlation is present ( $\rho_S = 0.60$  and  $\log p_S = -11.9$  in flux space and  $\rho_P = 0.81$  in luminosity space). The correlation strength further increases in luminosity space if we regard only those 101 objects that are unaffected by absorption in the 14-195 keV band, i.e.  $\log N_{\text{H}} < 23.7$  ( $\rho_P = 0.62$ ). The correlation strength still remains lower than that of the 12  $\mu\text{m}$ –2-10 keV correlation however. In addition, the observed and intrinsic scatter are higher as well ( $\sigma_X^M = 0.41$  and  $\sigma_{\text{int}} = 0.39$ ) while the fitted slope is slightly lower:  $\log L^{\text{nuc}}(12\ \mu\text{m}) \propto (0.91 \pm 0.04) \log L^{\text{obs}}(14\text{-}195\text{ keV})$ . As a consistency check, we also compute the 14-195 keV–2-10 keV correlation, which yields  $\log L^{\text{obs}}(14\text{-}195\text{ keV}) \propto (1.01 \pm 0.02) \log L^{\text{int}}(2\text{-}10\text{ keV})$ , also listed in Table 1. Thus, taking this slight non-linearity into account, the different luminosity correlations are consistent to each other within  $1\sigma$ .

In the following, we concentrate on the 12  $\mu\text{m}$  versus intrinsic 2-10 keV luminosity correlation because the corresponding data are available for all objects of the reliable sample.

### 4.3 Dependence on luminosity

The increased number of objects and improved accuracy of the MIR and X-ray data motivates the search for fine structure in the MIR–X-ray correlation based on other AGN properties. First, we

investigate whether there is a luminosity dependence in the logarithmic MIR–X-ray ratio,  $R_X^M$ , and whether the slope of the correlation changes with luminosity. For this purpose, we compute the error-weighted mean MIR–X-ray ratio of the detected objects from the reliable sample for different binnings in  $L^{\text{int}}(2\text{-}10\text{ keV})$  and  $L^{\text{nuc}}(12\ \mu\text{m})$ , shown in Fig. 10. We exclude the NLS1 sources from this analysis for the reasons given in Sect. 4.4, as well as 3C 273. The latter object is presumably beamed (e.g., Soldi et al. 2008) and would have an disproportionately large effect on the fitting because of its isolated position at very high luminosities ( $\approx 10^{46}$  erg/s), separated from the main population by more than an order of magnitude. Note that 3C 273 however follows the general behaviour found below. There is a weak global trend of decreasing  $R_X^M$  with increasing luminosity for binning along the  $L^{\text{int}}(2\text{-}10\text{ keV})$  axis. For the X-ray binning, the ratio changes from approximately 0.4 dex to 0 dex over approximately five orders of magnitude in luminosity, which is consistent with the fitted slopes  $< 1$  that we found in Sect. 4.1. Out of the 14 upper limits, only LEDA 013946 is not consistent with the general behaviour by more than  $1\sigma$  ( $\log L^{\text{int}}(2\text{-}10\text{ keV}) = 43.2$ ;  $R_X^M \leq 0.08$ ). In particular, at the highest probed luminosities,  $\log L^{\text{int}}(2\text{-}10\text{ keV}) \geq 44$ , a significant decrease seems to be present. The two-sided KS test provides maximum difference for separating the population at a threshold of  $\sim 44.1$  ( $D_{\text{KS}} = 0.66$ ;  $\log p_{\text{KS}} = -4.2$ ). We perform also the Monte-Carlo sampling with the above found threshold as described in Sect. 3 and get a 68 per cent confidence interval for  $p_{\text{KS}}$  of 0.004 to 3 per cent. However, such a decrease is not visible when the binning is done along the  $L^{\text{nuc}}(12\ \mu\text{m})$  axis (brown data points in Fig. 10) and thus the corresponding KS test shows no significant difference.

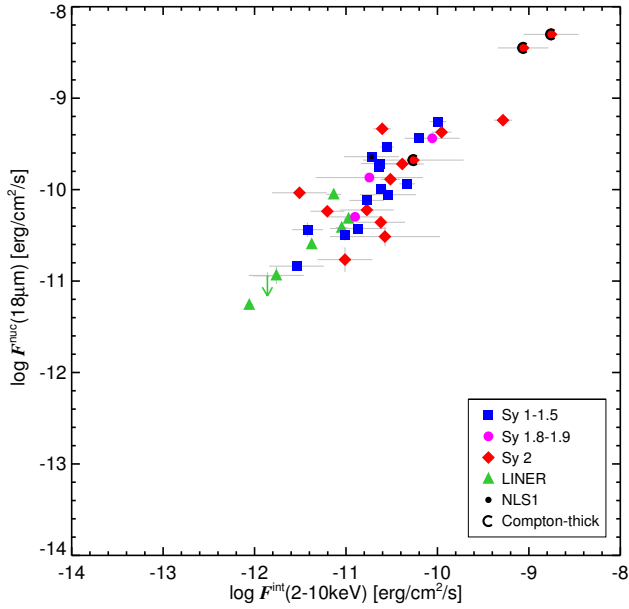


**Figure 6.** Relation of the nuclear 18  $\mu\text{m}$  and intrinsic 2-10 keV fluxes for the reliable sample. Symbols and colours are as in Fig. 1 apart from all objects having filled symbols.

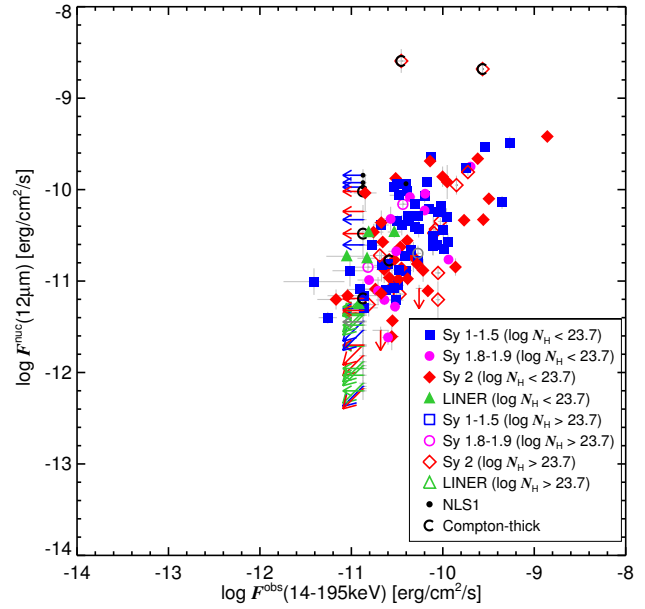


**Figure 8.** Relation of the nuclear 12  $\mu\text{m}$  and observed 14-195 keV fluxes for the reliable sample. Symbols and colours are as in Fig. 1 apart from filled symbols here marking objects with  $\log N_{\text{H}} \leq 23.7$ .

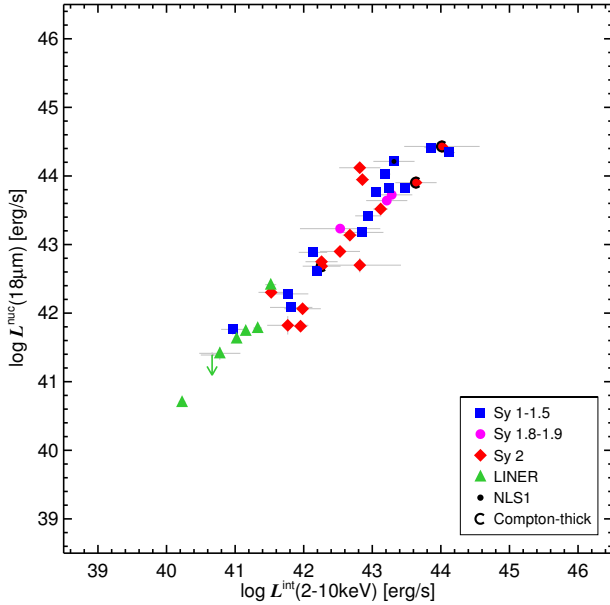


**Figure 7.** Relation of the nuclear 18  $\mu\text{m}$  and intrinsic 2-10 keV luminosities for the reliable sample. Symbols and colours are as in Fig. 6.

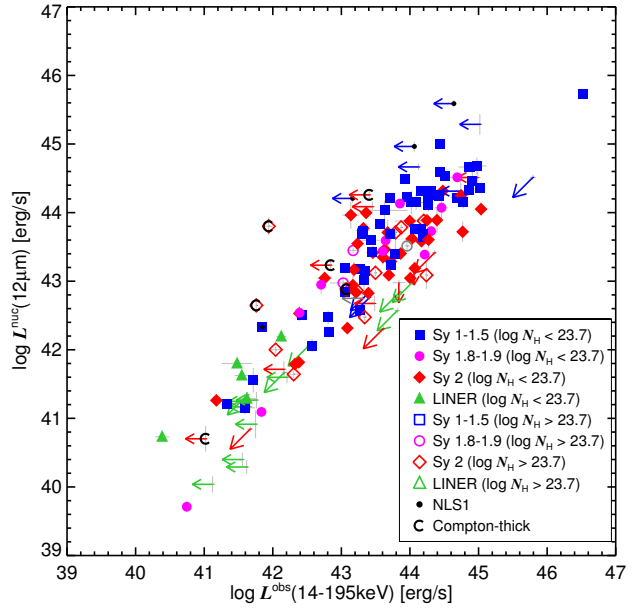


**Figure 9.** Relation of the nuclear 12  $\mu\text{m}$  and observed 14-195 keV luminosities for the reliable sample. Symbols and colours are as in Fig. 8.

Therefore, we employ another diagnostic, namely to compare the slopes of linear fits for different luminosity cuts in 12  $\mu\text{m}$  and 2-10 keV space in Fig. 12. The individual fitted slopes,  $b$ , for using thresholds in either  $L^{\text{int}}(2-10\text{keV})$  or  $L^{\text{nuc}}(12\mu\text{m})$  space are between 0.95 and 1.15 and are in general consistent with the unity. Only the highest luminosity bin for  $L^{\text{nuc}}(12\mu\text{m})$  has a steep slope of  $\sim 1.14$  that differs from unity by more than one  $\sigma$ . On the other hand, the corresponding  $L^{\text{int}}(2-10\text{keV})$  bin has the lowest slope of

$\sim 0.96$ . Again, this is caused by the insufficient object numbers above  $10^{44}$  erg/s. However, the two highest bins of both threshold directions are consistent with the slopes at lower luminosities and do not indicate any trend. Therefore, we conclude that there is no conclusive evidence for any local changes in the MIR–X-ray ratio or correlation slope with luminosity (see Sect. 5.3 for further discussion and also Mateos et al. 2015; but see Stern 2015).

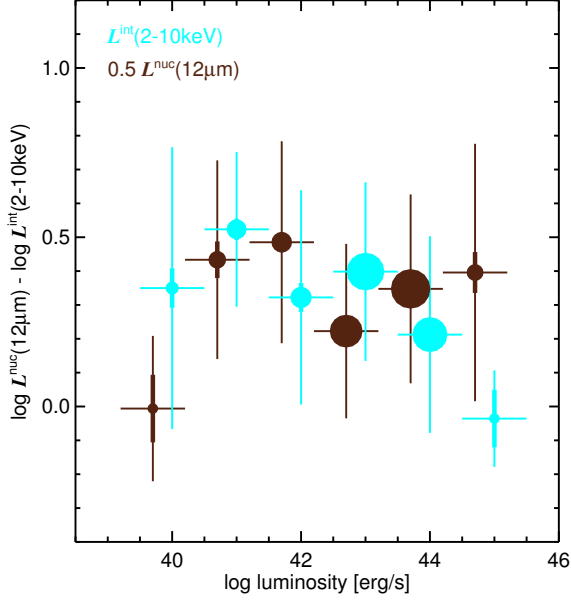


**Figure 10.** MIR–X-ray ratio over luminosity for the reliable sample. The data are binned with 1 dex bin width. Cyan symbols mark the error-weighted mean for a binning with  $L^{\text{int}}(2\text{--}10\text{keV})$  as  $x$ -axis while brown symbols mark a binning along  $L^{\text{nuc}}(12\mu\text{m})$ . The latter is shifted by  $-0.3$  dex to compensate for the constant  $a$  in the correlation. The area of the filled circles is proportional to the number of objects in that bin with the smallest circle corresponding to six and the largest to 61 objects. The error bars mark the bin width and error-weighted standard deviation of the MIR–X-ray ratio in that bin. In addition, the uncertainty of the weighted means are marked with thick vertical error bars which in most cases are smaller than the filled circles.

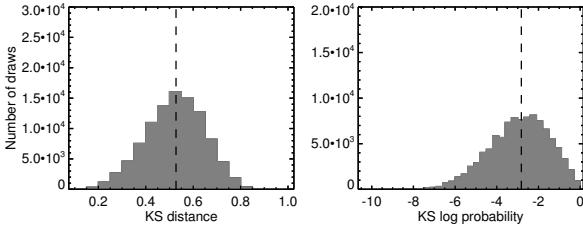


**Figure 11.** Results of the KS test for an MIR–X-ray ratio change above the luminosity  $\log L^{\text{int}}(2\text{--}10\text{keV}) = 44.1$ . The dashed vertical lines mark the median.

#### 4.4 Dependence on optical type

Next, we investigate differences with the optical type by fitting the  $12\mu\text{m}$ – $2\text{--}10\text{keV}$  luminosity distributions separately for type I, type II and LINER AGN (Fig. 13). Note that we treat NLS1 not as type I AGN and that we also exclude 3C 273 from this analysis. This leaves 54 type I AGN of the reliable sample, while there are 58 type II and 19 LINER objects. The corresponding linear fits are listed in Table 1 and shown in Fig. 13 as well. The slopes of the type I and II correlations are similar to each other and the total population fit. However, type I objects display a systematically higher constant  $a$  and MIR–X-ray ratio than type II objects (0.15 dex difference at  $2\sigma$  significance). Note that this offset is consistent to the finding for more powerful AGN (Hönig et al. 2011). In addition,

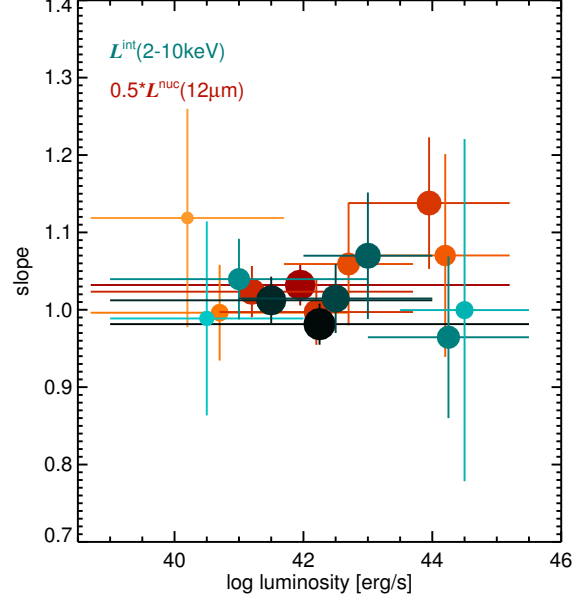


**Figure 12.** Fitted linear slopes,  $b$  of  $\log(L^{\text{nuc}}(12\mu\text{m})) - 43 = a + b(\log(L^{\text{int}}(2\text{--}10\text{keV})) - 43)$  for the reliable sample. Each data point represents the slope of the `linmix_err` fit for a sub-sample with luminosities in between the thresholds given by the width of the horizontal error bars. The vertical error bar gives the  $1\text{-}\sigma$  uncertainty of the fitted slope. The area of the filled circles and darkness in color are proportional to the number of objects in that sub-sample with the smallest circle corresponding to 23 and the largest to 147 objects. Cyan to black coloured symbols mark sub-samples with thresholds in  $L^{\text{int}}(2\text{--}10\text{keV})$  while orange to red symbols mark sub-samples with thresholds in  $L^{\text{nuc}}(12\mu\text{m})$ . For the latter,  $\log(L^{\text{int}}(2\text{--}10\text{keV})) - 43 = a' + b'(\log(L^{\text{nuc}}(12\mu\text{m})) - 43)$  was fitted and  $b'$  then inverted for direct comparison. In addition, the  $L^{\text{nuc}}(12\mu\text{m})$ -based data points are shifted by  $-0.3$  dex to compensate for the constant  $a$  in the correlation.

the observed and intrinsic scatter is lower in the type I population ( $\sigma_{\text{int}} = 0.25$ ) compared not only to the type II ( $\sigma_{\text{int}} = 0.31$ ) but also to the whole reliable sample ( $\sigma_{\text{int}} = 0.32$ ). Although the uncertainties of these values are larger than the differences, it indicates that the scatter in the total population is dominated by the type II objects. LINERs exhibit the highest average MIR–X-ray ratio (0.46) and a flatter but consistent fitted slope compared to the Seyferts. We note that all 14 upper limits except again LEDA 013946 are consistent with the obtained fits within the  $1\sigma$  X-ray uncertainty. Finally, there are too few NLS1 for a reasonable fit but their average MIR–X-ray ratio is very high compared to the other AGN classes (1.16).

To further investigate if the differences between the different optical classes are statistically significant we employ the two-sided KS test on the distribution of MIR–X-ray ratios of the MIR-detected reliable AGN shown in Fig. 14. Note that here the upper limits of all MIR non-detected AGN are within the central 68 per cent interval of the  $R_X^{\text{M}}$  distributions for their corresponding optical classes. The difference between type I and type II AGN is not significant at  $3\text{-}\sigma$  level according to this test, the resulting distribution shown in Fig. 15. The 68 per cent confidence interval for the null-hypothesis probability is from 0.25 to 30 per cent.

Similarly, the difference between LINERs to the combined type I+II sample remains insignificant at  $3\text{-}\sigma$  level, the 68 per cent interval for  $p_{\text{KS}}$  is 0.5 to 36 per cent. Still, we state a correlation fit excluding LINERs (type I+II) in Table 1 for completeness.



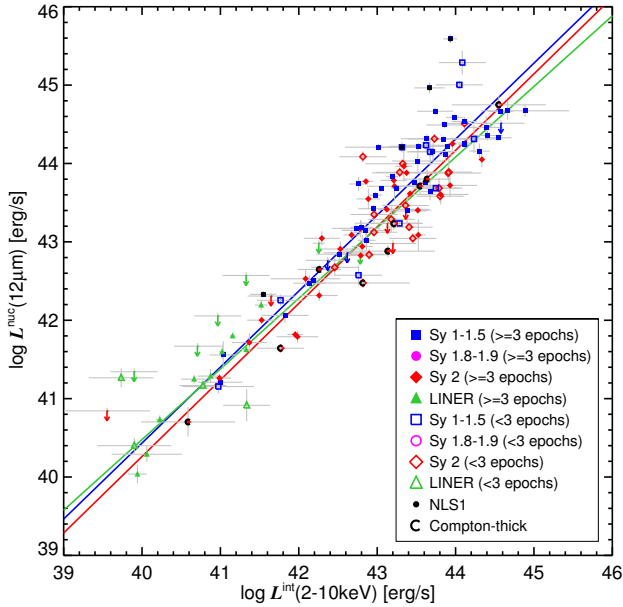


**Figure 13.** Relation of the nuclear 12  $\mu\text{m}$  and intrinsic 2–10 keV luminosities for the different optical AGN types. Symbols and colours are as in Fig. 3. In addition, the blue, red and green lines mark the `linmix_err` fits to the type 1, type 2 and LINER objects in the reliable sample.

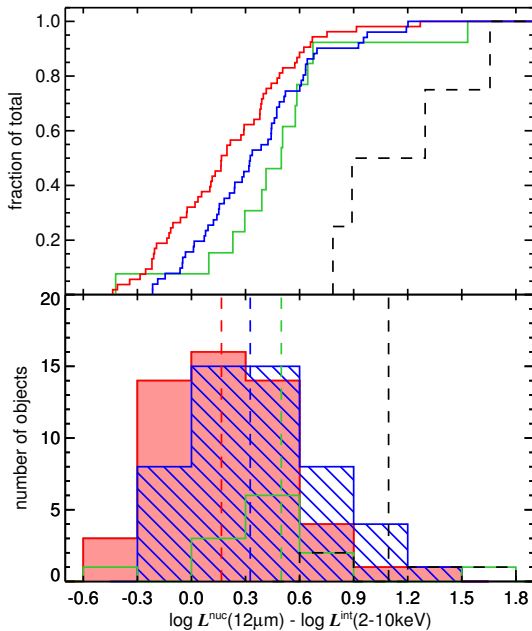


**Figure 14.** Distribution of the 12  $\mu\text{m}$ –2–10 keV ratio for the different optical AGN types. *Top:* Normalised cumulative distribution with the blue solid line being type 1, the red type 2, the green LINER, and the black dashed line NLS1. *Bottom:* Histogram distribution with blue hatched being type 1, red solid type 2, green empty LINER, and black empty dashed NLS1. The dashed vertical lines indicate the corresponding median 12  $\mu\text{m}$ –2–10 keV ratios.

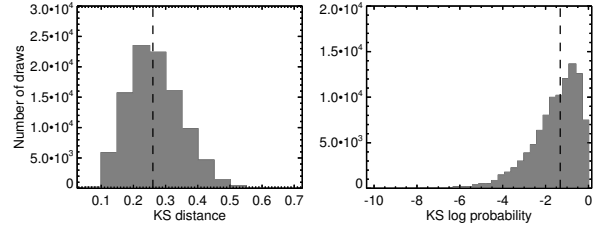


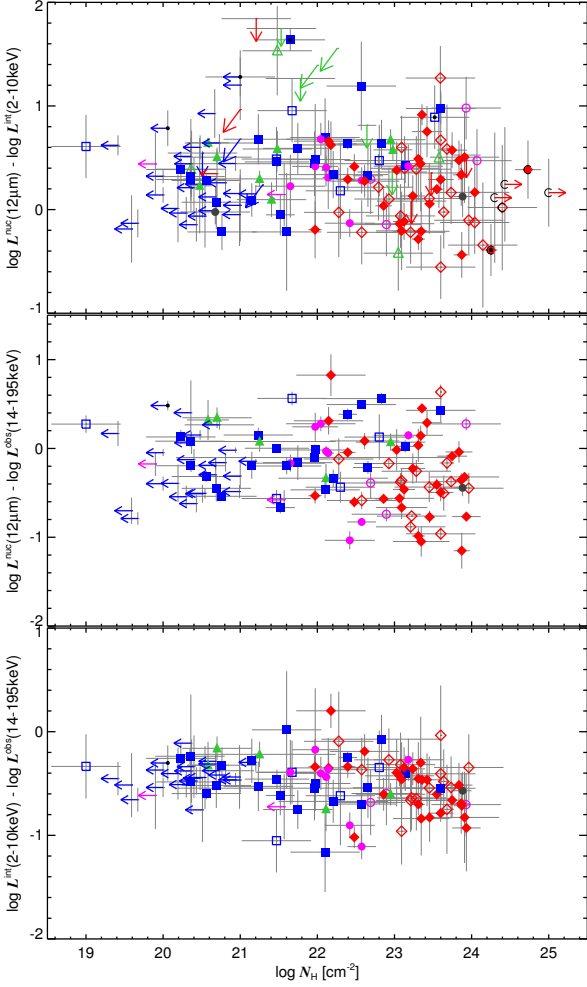
**Figure 15.** Results of the KS test for an MIR–X-ray ratio difference between type I and II AGN. The dashed vertical lines mark the median.

The largest statistically significant difference is found for the NLS1 versus type I according to the KS-test with a 68 per cent interval for  $p_{\text{KS}}$  of 0.06 to 2 per cent and a median  $D_{\text{KS}} = 0.86$ . A possible explanation for their high MIR–X-ray ratios is that owing to their steep X-ray spectral energy distributions, the 2–10 keV emission is not representative of the bolometric luminosity in NLS1. On the other hand, NLS1 generally have complex X-ray spectra which make intrinsic luminosity estimates difficult. Thus, a larger sample of NLS1 is required to verify our finding.

#### 4.5 Dependence on X-ray column density

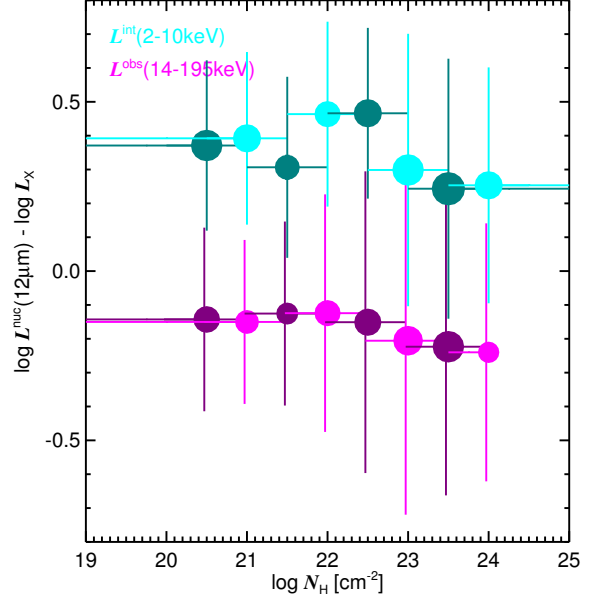
To investigate possible differences between obscured and unobscured AGN, it is presumably superior to use the X-ray column density,  $N_{\text{H}}$ , rather than the optical type because  $N_{\text{H}}$  probes the nuclear obscuration more directly and in a quantitative way and neutralises possible selection effects against obscured AGN. According to results of the previous sections, we exclude the NLS1 sources here. Fig. 16 displays the relation of the MIR–X-ray ratio with the column density. As expected, type I AGN have in general  $\log N_{\text{H}} \lesssim 22$  and type II AGN  $\log N_{\text{H}} \gtrsim 22$ . However, there are a few exceptions, namely two type I AGN with  $\log N_{\text{H}} > 23$  (3C 445 and ESO 323-77). In both cases, the absorption is highly variable and/or partly caused by broad-line region clouds (Reeves et al. 2010; Miniutti et al. 2014). In addition, there are three type II AGN with  $\log N_{\text{H}} < 22$ , namely the true Sy 2 candidate NGC 3147 (Pappa et al. 2001) the borderline Sy 2/LINER objects 3C 317 and NGC 4374. LINERs, intermediate type AGN (and NLS1) are distributed over most of the whole  $N_{\text{H}}$  range. No global trend of the MIR–X-ray ratio with  $N_{\text{H}}$  is obvious in Fig. 16 when using either the intrinsic 2–10 keV or the observed 14–195 keV band, and none of the objects with limits on either  $R_{\text{X}}^{\text{M}}$  or  $N_{\text{H}}$  sticks out. On the other hand, there seems to be a decline of the MIR–X-ray ratio for column densities  $\gtrsim 10^{23} \text{ cm}^{-2}$ . For example, the median  $N_{\text{H}}$  is  $> 10^{23} \text{ cm}^{-2}$  for all 32 objects with a 12  $\mu\text{m}$ –2–10 keV ratio  $< 0$ . In particular, all four objects with 12  $\mu\text{m}$ –2–10 keV ratio  $< -0.3$  have  $N_{\text{H}} > 10^{23} \text{ cm}^{-2}$  (NGC 1144, NGC 3169, ESO 297-18, and NGC 5728). However, the result of the KS test splitting the whole sample at  $10^{23} \text{ cm}^{-2}$  does not indicate significant differences (68 per cent confidence interval on  $p_{\text{KS}}$  is from 0.2 to 27 per cent).

In order to quantify a decrease of  $R_{\text{X}}^{\text{M}}$  at high  $N_{\text{H}}$  better, we first look at the weighted mean MIR–X-ray ratio for both 2–10 keV and 14–195 keV using different binnings of the column density in Fig. 17. Here, objects with only limits on  $R_{\text{X}}^{\text{M}}$  are excluded, which includes 14–195 keV upper limits for the binning in  $L^{\text{obs}}$  (14–195 keV). Limits in  $N_{\text{H}}$  are treated as belonging to the bin of their limit value for the sake of simplicity. This does not affect the results obtained below. The binnings using both  $L_{\text{X}}$  and  $L^{\text{obs}}$  (14–195 keV) for the MIR–X-ray ratio show qualitatively a



**Figure 16.** MIR–X-ray ratio versus the X-ray column density for the reliable sample. *Top:* 12  $\mu\text{m}$ –2–10 keV ratio. Symbols and descriptions are as in Fig. 3. *Middle:* 12  $\mu\text{m}$ –14–195 keV ratio for all 14–195 keV detected non-CT objects in the reliable sample. *Bottom:* 2–10–14–195 ratio for all objects as in the middle plot.

similar behaviour, namely a  $\sim 0.1$  dex increase of  $R_X^M$  for  $22 \leq \log N_H \leq 23$ , followed by a decrease of  $\sim 0.15$  dex for  $\log N_H \geq 23$ . Note that this trends occurs independently of the exact bin locations chosen as demonstrated in Fig. 17 and also when removing the outliers with the most extreme MIR–X-ray ratios at intermediate column densities visible in Fig. 16. Thus, there is indeed a weak global decreasing trend present with, however, a maximum MIR–X-ray ratio at intermediate column densities, instead of at the lowest column densities as naively expected. The KS test, yields a median  $p_{KS} = 6$  per cent (68 per cent confidence interval: 0.2 to 30 per cent) between the intermediate and highly obscured objects using the thresholds above. Furthermore, the ten objects with highest obscuration ( $\log N_H > 24$ ), exhibit the lowest average MIR–X-ray ratio of 0.07 ( $\sigma_X^M = 0.27$ ) compared to 0.36 ( $\sigma_X^M = 0.41$ ) for objects with  $\log N_H < 24$ . The median  $p_{KS}$  is 6 per cent (68 per cent confidence interval: 0.3 to 35 per cent) from a corresponding KS test. Therefore, the observed trend might be real since consistent for both  $L_X$  and  $L^{\text{obs}}(14\text{--}195\text{ keV})$  but is not significant at a  $3\text{-}\sigma$  level. The upper limits are consistent with the result except for two of the 19 objects with non-detections in  $L^{\text{obs}}(14\text{--}195\text{ keV})$  but detections in  $L^{\text{nuc}}(12\text{ }\mu\text{m})$ , PG 2130+099 and MCG 2-8-39, which



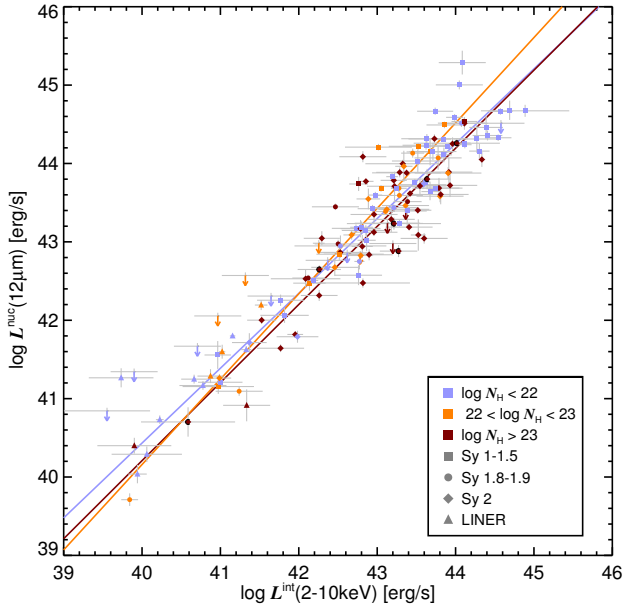
**Figure 17.** MIR–X-ray ratio over X-ray column density for the reliable sample. The data are binned with 1 dex bin width and two different choices of bin centres, shifted by 0.5 dex. Cyan symbols mark the error-weighted mean for a binning using  $L^{\text{int}}(2\text{--}10\text{ keV})$  whereas lighter and darker color distinguish the two binnings. Magenta symbols mark a binning using  $L^{\text{obs}}(14\text{--}195\text{ keV})$  for the MIR–X-ray ratio again with lighter and darker color distinguishing the two binnings. The area of the filled circles is proportional to the number of objects in that bin with the smallest circle corresponding to 18 and the largest to 40 objects. The error bars mark the bin width and weighted standard deviation of the MIR–X-ray ratio in that bin. In addition, the uncertainty of the weighted means are smaller than the filled circles in all cases.

exhibit exceptionally high lower limits on the logarithmic 12  $\mu\text{m}$  to 14–195 keV ratios of  $\sim 0.5$ .

Second, we perform linear regression to the obscured and unobscured subsamples as displayed in Fig. 18. Here, we exclude 3C 273 from the analysis again. The correlation and fitting parameters listed in Table 1 show that the unobscured subsample shows a much stronger correlation and lower intrinsic scatter than the obscured subsample ( $\log N_H \geq 23$ ), similar to the optical type division. The linear fits of the unobscured and obscured AGN are consistent within the  $1\text{-}\sigma$  uncertainties with a minimal offset of the unobscured to a higher MIR–X-ray ratio by  $\sim 1$  dex. The intermediately obscured subsample ( $22 \leq \log N_H \leq 23$ ) has a steeper slope ( $1.09 \pm 0.06$ ) and higher intercept ( $0.43 \pm 0.07$ ). This result is insensitive against the exact selection of the  $N_H$  threshold values, and removing the lowest luminosity objects would make the deviation from the fits of the other subsamples even larger. Moreover, the partial correlation coefficient and scatter are tightest for the intermediately obscured subsample, making it stand out the most. This is similar to the result of the previous test. We discuss the implications of these results in Sec. 5.4.

#### 4.6 Dependence on radio-loudness

This section investigates whether there is any connection between MIR–X-ray correlation and the radio power of the AGN. This is interesting because non-thermal emission processes from a jet, if present, might significantly contribute or even dominate



**Figure 18.** Relation of the nuclear  $12\ \mu\text{m}$  and intrinsic 2–10 keV luminosities for the different X-ray obscuration levels. Symbols are as in Fig. 3 while light blue marks objects with  $\log N_{\text{H}} < 22$ , orange for  $22 \leq \log N_{\text{H}} \leq 23$  and dark red for  $\log N_{\text{H}} \geq 23$ . The corresponding `linmix_err` fits are marked by solid lines in the same colors.

the MIR and/or the X-ray emission of the AGN. For this purpose, we collect radio fluxes for all reliable objects from NED, of which 137 have detections reported in at least one frequency band. There is no single frequency band with observations of all targets. The most common is  $\sim 1.4$  GHz with 121 objects (mainly from White & Becker 1992; Condon et al. 1998; Condon, Cotton & Broderick 2002), followed by  $\sim 4.9$  GHz with 91 objects (mainly from Edelson 1987; Gregory & Condon 1991; Gregory et al. 1994; Barvainis, Lonsdale & Antonucci 1996; Wright et al. 1996; Nagar, Wilson & Falcke 2001; Tingay et al. 2003; Gallimore & Beswick 2004; Nagar, Falcke & Wilson 2005). Moreover, the data are highly heterogeneous with respect to the telescope used, angular-resolution, extraction apertures, and observing time. Therefore, rather than a direct comparison using the radio emission, we classify the objects into radio-quiet and radio-loud, following the definition by Terashima & Wilson (2003),  $R_{\text{X}}^{\text{R}} = \log L(4.9\ \text{GHz}) - \log L^{\text{int}}(2-10\ \text{keV})$  and  $R_{\text{X}}^{\text{R}} > -4.5$  being radio-loud. In order to classify objects with no available  $L(4.9\ \text{GHz})$ , we use the low-angular resolution measurements for  $L(1.4\ \text{GHz})$  and  $L(0.8\ \text{GHz})$ , the latter available for 33 objects (Mauch et al. 2003). These three bands cover all 137 objects with radio detections. The average conversion factors from  $L(4.9\ \text{GHz})$  to  $L(1.4\ \text{GHz})$  and  $L(0.8\ \text{GHz})$  are  $\log L(1.4\ \text{GHz}) = (0.35 \pm 0.85) + \log L(4.9\ \text{GHz})$  and  $\log L(0.8\ \text{GHz}) = \log L(1.4\ \text{GHz}) - (0.14 \pm 0.12)$ . They are computed from the 85 and 19 objects with data in both bands respectively. Because the goal is to obtain robust radio-loudness determinations, firstly, the standard deviations of the conversions are taken into account (e.g., only  $\log L(1.4\ \text{GHz}) - \log L^{\text{int}}(2-10\ \text{keV}) > -3.3$  is radio-loud). Secondly, high angular resolution  $L(4.9\ \text{GHz})$  data are preferred, and  $R_{\text{X}}^{\text{R}} > -3$  as criterion is used when only low-angular resolution  $L(4.9\ \text{GHz})$  is available. Using these definitions, 48 objects can robustly be classified as radio-loud, and 41 as radio-

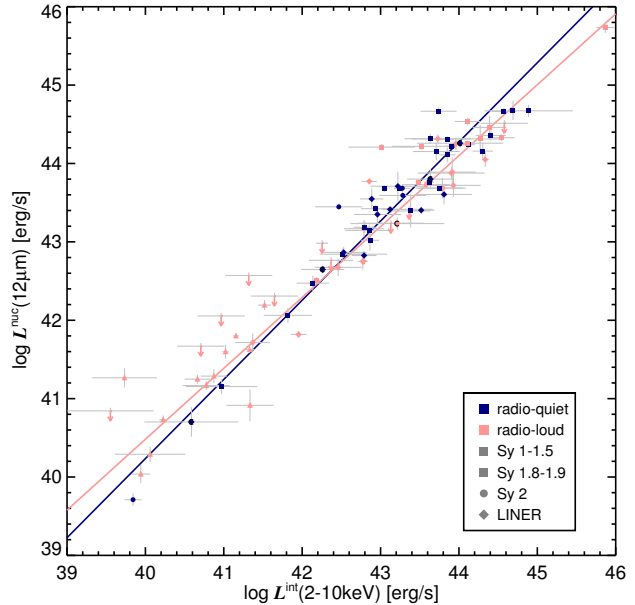


**Figure 19.** Relation of the nuclear  $12\ \mu\text{m}$  and intrinsic 2–10 keV luminosities for radio-quiet (dark-blue) and radio-loud (light-red) AGN. Symbols are as in Fig. 3. The corresponding `linmix_err` fits are marked by solid lines in the same colors.

quiet. These classifications are listed in Table 2 for the individual objects.

Fig. 19 shows the MIR–X-ray correlation for radio-loud and radio-quiet objects. Radio-loud objects tend to exhibit on average higher MIR–X-ray ratios at low luminosities compared to the radio-quiet ones, while this trend inverts at high luminosities. The transition happens between  $42 \leq \log L^{\text{int}}(2-10\ \text{keV}) \leq 43$ . Therefore, the corresponding radio-loud fit has a significantly flatter slope ( $0.90 \pm 0.04$ ) than the radio-quiet fit ( $1.01 \pm 0.05$ ; see Table 1). Note that this result does not depend on the low-luminosity objects ( $\log L^{\text{int}}(2-10\ \text{keV}) \leq 42$ ). If these are removed from the fitting for the radio-loud subsample, the slope becomes even a little bit flatter ( $0.88 \pm 0.09$ ). The radio-quiet sample shows a remarkable high partial correlation ( $0.88$ ) and small scatter ( $\sigma_{\text{X}}^{\text{M}} = 0.28$ ;  $\sigma_{\text{int}} = 0.21$ ). Both are worse for the radio-loud subsample.

This result can be explained by the presence of a jet in the radio-loud objects which dominates the MIR emission at low-luminosities (e.g., Mason et al. 2012). Most of these objects are optically classified as LINERs, which showed a higher MIR–X-ray ratio already in Section 4.4. More puzzling is the situation at high luminosities where the jet apparently contributes much more to the X-rays (e.g., Hardcastle, Evans & Croston 2009; see next section).

## 5 DISCUSSION

### 5.1 Dependence of results on the fitting method

In order to investigate how the exact form of the correlation depends on the fitting method chosen, we concentrate on the  $L^{\text{nuc}}(12\ \mu\text{m})$ – $L^{\text{int}}(2-10\ \text{keV})$  correlation for the whole reliable sample. First, we verify that the choice of input parameters for `linmix_err` does not influence our results. If instead of three Gaussians (the default) we choose a uniform prior distribution, the

intercept,  $a$ , becomes  $\sim 2$  per cent smaller while the slope,  $b$ , increases by  $\sim 0.1$  per cent. Both are much smaller than the uncertainties on  $a$  and  $b$ . Using two Gaussians leads to even smaller deviations. The same applies to changing the algorithm to create the Markov Chains or the number of random draws as long as the latter is sufficiently large (here  $10^4$ ).

For the following comparisons, upper limits can not be taken into account. Using only the 138 detected objects in the reliable sample,  $a$  and  $b$  become  $0.33 \pm 0.03$  and  $0.98 \pm 0.03$  respectively. The correlation parameters using `fitexy` instead are  $a = 0.37 \pm 0.01$  and  $0.99 \pm 0.01$  and thus consistent to within  $1\text{-}\sigma$ . In other words, the difference in predicted  $L^{\text{nuc}}(12\mu\text{m})$  depending on the algorithm is smaller than  $0.07$  dex over the whole luminosity range ( $39 \leq \log L^{\text{int}}(2\text{-}10\text{ keV}) \leq 46$ ). Therefore, we conclude that the choice of fitting algorithm or inclusion of non-detections does not have a significant effect on the results obtained here.

However, we note that at least for using `linmix_err`, the choice of independent variable makes a difference by more than  $1\sigma$ . Specifically, for using  $L^{\text{nuc}}(12\mu\text{m})$  as independent variable,  $a$  and  $b$  become  $0.33 \pm 0.03$  and  $1.06 \pm 0.03$  when inverting back to the  $\log L^{\text{nuc}}(12\mu\text{m}) = a + b \log L^{\text{int}}(2\text{-}10\text{ keV})$  form. Therefore, for predicting  $L^{\text{int}}(2\text{-}10\text{ keV})$  based on a  $L^{\text{nuc}}(12\mu\text{m})$  measurement, the following equation should be used:

$$\log\left(\frac{L^{\text{int}}(2\text{-}10\text{ keV})}{10^{43}\text{ erg s}^{-1}}\right) = (-0.32 \pm 0.03) + (0.95 \pm 0.03) \log\left(\frac{L^{\text{nuc}}(12\mu\text{m})}{10^{43}\text{ erg s}^{-1}}\right). \quad (2)$$

## 5.2 Sample biases

The sample of the 152 reliable AGN from the MIR atlas is neither uniform nor complete. In order to test whether the MIR–X-ray correlations are representative for the local AGN population, we perform the following two tests.

### 5.2.1 Uniform sample test

First, the MIR–X-ray properties for the uniform flux-limited BAT 9 month AGN sample as defined by Winter et al. (2009a) are measured. The 14–195 keV energy band is possibly best-suited for selecting AGN because emission in this band is dominated by AGN, and it is only weakly dependent on nuclear obscuration up to CT columns. Out of the 102 objects in this sample, 80 have high angular resolution MIR photometry available. Note that four of these sources are not in the reliable AGN sample because they are AGN/starburst composites (Mrk 520, NGC 6240S and NGC 7582) or are Compton-thick without reliable intrinsic 2–10 keV emission estimates (NGC 3281). In the  $12\mu\text{m}$ –2–10 keV luminosity plane (Fig. 20), the partial correlation rank for the 80 objects from the BAT 9 month sample is 0.74 and the intrinsic scatter is 0.24, so slightly lower values than for the reliable sample. The correlation according to `linmix_err` is:

$$\log\left(\frac{L^{\text{nuc}}(12\mu\text{m})}{10^{43}\text{ erg s}^{-1}}\right) = (0.23 \pm 0.04) + (1.02 \pm 0.05) \log\left(\frac{L^{\text{int}}(2\text{-}10\text{ keV})}{10^{43}\text{ erg s}^{-1}}\right), \quad (3)$$

which is consistent with the fit for all reliable AGN. As visible in Fig. 20, the rather high 14–195 keV flux limit of the nine-month BAT AGN sample leads to a large under-density of low-luminosity

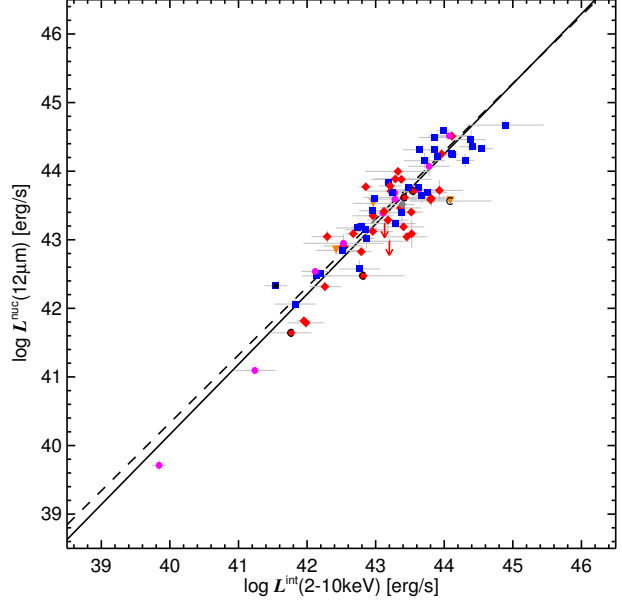


**Figure 20.** Relation of the nuclear  $12\mu\text{m}$  and intrinsic 2–10 keV luminosities for the nine-month BAT AGN sample. Symbols and colours are as in Fig. 3. In addition, the solid black line marks the `linmix_err` fit for the BAT sample while the dashed line marks the one for all reliable AGN.

AGN in that sample. Only the X-ray brightest low-luminosity objects are detected, which biases the correlation towards a steeper slope and lower intercept. For this reason, the correlation derived from reliable AGN sample is more representative of the whole local AGN population. Note that the more recent BAT AGN sample contains more low-luminosity objects but for these the high angular resolution MIR coverage becomes too small for investigating the MIR–X-ray correlation. Finally, Compton-thick obscured objects are presumably under-represented in both the BAT and the reliable sample because of absorption in the 14–195 keV band and the difficulty to estimate reliable intrinsic 2–10 keV fluxes.

### 5.2.2 Volume-limited sample test

The second test is addressing biases caused by the incompleteness of the sample. Unfortunately, the fraction of local AGN with high angular resolution MIR photometry is too low to obtain significant coverage in representative volume-limited samples that contain low and high luminosity AGN. However, one can use distance and luminosity cuts of the reliable sample to form cubes in logarithmic distance–luminosity space with rather uniform sampling. We select a cube with  $1.1 < \log D < 1.7$ ,  $39 < \log L^{\text{int}}(2\text{-}10\text{ keV}) < 43$ , representative of the low luminosity range (Fig. 21). It contains 39 objects, and its corresponding  $12\mu\text{m}$ –2–10 keV luminosity correlation has an intercept of  $a = 0.38 \pm 0.12$  and a slope of  $b = 1.00 \pm 0.07$ , so similar to the values for the whole reliable sample. Another cube is  $(2.1 < \log D < 2.7, 43 < L^{\text{int}}(2\text{-}10\text{ keV}) < 44.7)$  with 45 objects and  $a = 0.01 \pm 0.22$  and a slope of  $b = 1.21 \pm 0.25$ . This fit is steeper than that for the reliable sample although consistent within the uncertainties. Although the chosen cuts are optimizing the sampling as well as possible, the resulting luminosity coverage of this cube is not large enough to provide valuable constraints. This is indicated by the large uncertainties on  $a$  and  $b$ .

In conclusion, the sample bias tests does not indicate that the

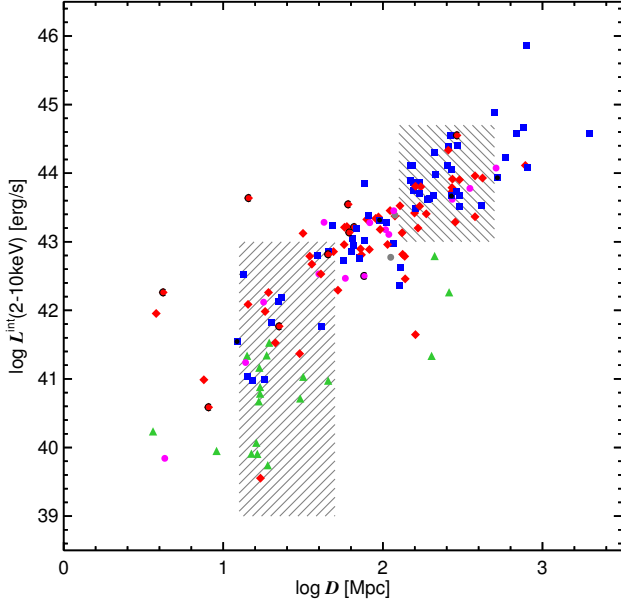


**Figure 21.** Intrinsic 2-10 keV luminosity over distance for the reliable sample. Symbols and colours are as in Fig. 3. In addition, the hatched areas mark the two cubes used for the volume test in Sect. 5.2.2. See text for explanation.

results derived from the reliable sample of AGN in the MIR atlas are affected by significant biases. However, we encourage further tests with larger volume-limited samples.

### 5.3 Comparison to the literature

#### 5.3.1 Previous studies based on high resolution MIR data – Gandhi et al. (2009) and Levenson et al. (2009)

While a strong MIR–X-ray correlation was reported in Elvis et al. (1978), Glass, Moorwood & Eichendorf (1982), Krabbe, Böker & Maiolino (2001) and Lutz et al. (2004), a fitting-based functional description of the correlation was only attempted in Horst et al. (2006, 2008) and Ramos Almeida et al. (2007). While the latter work used low angular resolution *ISO* data, the former were based on high angular resolution ground-based MIR photometry. Horst et al. (2008) was then extended by Gandhi et al. (2009), Hönig et al. (2010) Asmus et al. (2011) and finally this work. Out of these studies, the correlation parameters from Gandhi et al. (2009) are the most widely used because they apply to all classes of AGN including CT objects. The parameters are based on the observed 12  $\mu\text{m}$  and intrinsic 2-10 keV luminosities for a heterogeneous sample of 42 local AGN observed with VISIR. For the fitting, the `fitexy` routine was used (Press et al. 1992) and provides as slope of  $1.11 \pm 0.04$ . The corresponding correlation is shown in Fig. 22 in comparison to the results obtained here. The slope for the Gandhi et al. sample depends on the choice of algorithm and becomes  $1.00 \pm 0.08$  when using `linmix_err` on the same data. The intercept is less sensitive to the fitting algorithm ( $0.35 \pm 0.06$  for `linmix_err`). Therefore, our new results are fully consistent with Gandhi et al. (2009).

A study similar to Gandhi et al. (2009) was presented in Levenson et al. (2009) although based on a smaller sample of 17 objects spanning only two orders of magnitude in  $L^{\text{int}}(2-10\text{keV})$ .

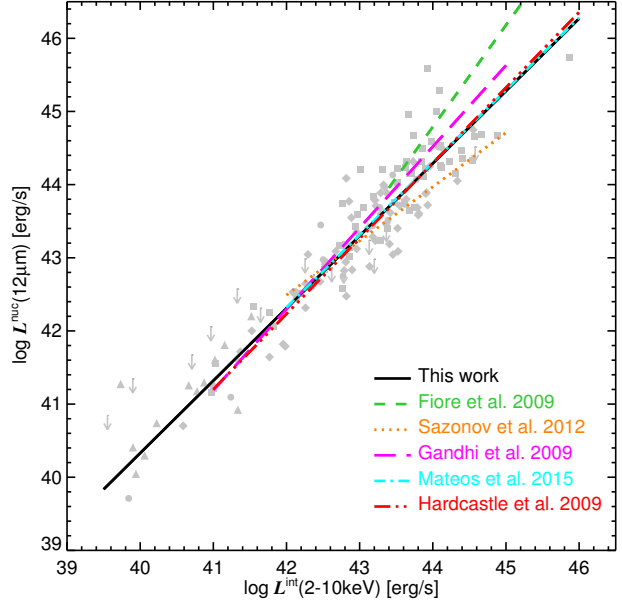


**Figure 22.** Comparison of different MIR–X-ray correlation fits in the literature. Note that no correction is applied for the different subbands used. The grey symbols mark the reliable AGN sample from this work.

They found a much steeper correlation  $\log L^{\text{nucl}}(12\mu\text{m}) \propto (1.32 \pm 0.11) \log L^{\text{int}}(2-10\text{keV})$  using bisector fitting. This fit is dominated by the type II sources in their sample because the fit to the type I objects only yields a slope of  $1.0 \pm 0.2$  consistent with Gandhi et al. (2009) and this work. They attribute the difference to star formation contamination even on small scales to the objects in their sample. In addition, half of their type II sources are Compton-thick obscured and thus have uncertain  $L^{\text{int}}(2-10\text{keV})$  values. We attribute differences between our study and Levenson et al. (2009) to this and the small sample size in the latter work, in particular because our sample incorporates all objects from Levenson et al. (2009).

#### 5.3.2 High luminosities – Fiore et al. (2009), Lanzuisi et al. (2009), Mateos et al. (2015) and Stern (2015)

Another often used version of the MIR–X-ray correlation is by Fiore et al. (2009) which focuses on the higher luminosity end. It used the observed restframe 5.8  $\mu\text{m}$  and 2-10 keV luminosities of  $\sim 80$  X-ray-selected type I AGN in the COSMOS and CDF-S fields with *Chandra* and *Spitzer* observations. Converted to our form of notation, their correlation is

$$\log \left( \frac{L^{\text{tot}}(5.8\mu\text{m})}{10^{43}\text{erg s}^{-1}} \right) = 0.40 + 1.39 \log \left( \frac{L^{\text{obs}}(2-10\text{keV})}{10^{43}\text{erg s}^{-1}} \right), \quad (4)$$

for  $\log L^{\text{tot}}(5.8\mu\text{m}) > 43.04$ . At the same time, Lanzuisi et al. (2009) performed a similar study but for luminous type II AGN. They obtain a slope of 1.24 in the same notation. Thus, both slopes are much steeper than our findings as visible in Fig. 22. Unfortunately, no uncertainties nor the algorithm used are stated in Fiore et al. (2009) and Lanzuisi et al. (2009). However, the distribution of sources in the MIR–X-ray plane (e.g., Fig. 5 in Fiore et al. 2009) shows that there is a clear trend of increasing MIR–X-ray ratio for high luminosities ( $\log L^{\text{tot}}(5.8\mu\text{m}) > 44$ ). Therefore, we can exclude error treatment and fitting technique as cause for the inconsistency. Furthermore, at these high luminosities, host related MIR

contamination should not be an issue, in particular for the type I AGN of Fiore et al. (2009) since these sources are presumably unobscured. On the other hand, they excluded seven objects because of their outlying position in the MIR–X-ray plane, indicating heavy obscuration. Therefore, it is possible that also some of the objects showing less extreme MIR–X-ray ratios are affected by obscuration in X-rays. Furthermore, the correlation using  $5.8\ \mu\text{m}$  could be intrinsically different from the  $12\ \mu\text{m}$  based correlation, in particular since the hot dust component dominates the MIR emission at  $5.8\ \mu\text{m}$  in many type I AGN rather than the warm component (dominating at  $12\ \mu\text{m}$ , if present; e.g., Edelson & Malkan 1986; Mor & Netzer 2012). Alternatively, it is possible that the MIR–X-ray correlation becomes steeper at high luminosities, although our sources overlapping with the Fiore et al. fitting region are not consistent with such a steep slope (see also discussion about Sazonov et al. 2012 below).

Very recently, Mateos et al. (2015) and Stern (2015) re-examined the  $6\ \mu\text{m}$ – $2\text{--}10\ \text{keV}$  correlation. The former uses a complete, flux limited sample of 232 AGN from the Bright Ultra hard XMM-Newton Survey. The X-ray luminosities were corrected for absorption through spectral modelling while no Compton-thick sources were found in their sample. The MIR luminosities were extracted from WISE through spectral decomposition of AGN and host contributions. Using also `linmix_err` with the X-ray luminosity as independent variable, Mateos et al. find a correlation slope of  $0.99 \pm 0.03$  applicable for the whole range up to luminosities of  $10^{46}\ \text{erg/s}$  in X-rays. This agrees very well with our result (Fig. 22) and contradicts as well the finding of Fiore et al. (2009).

Stern (2015), on the other hand, finds a steepening of the MIR–X-ray fit slope at luminosities above  $\log L^{\text{int}}(2\text{--}10\ \text{keV}) \sim 44.5$  using a combination of several samples, with multiwavelength data obtained with various recent instruments. Different, to all the other works, a second order polynomial is fitted to the data with the resulting fit bending at higher luminosities to higher MIR–X-ray ratios. This result agrees with our at lower luminosities ( $\lesssim 10^{44}\ \text{erg/s}$ ) where our sampling is still high. At higher luminosities it agrees rather with Fiore et al. (2009) but not with Mateos et al. (2015). This disagreement is not discussed in Stern (2015). We do not attempt to solve this controversy at high luminosities here but we would like to point out that there is a mismatch between the two high luminosity samples used, "SDSS DR5" versus "high-luminosity" sample in Stern (2015). Namely, the median MIR luminosity of the former sample is 0.8 dex lower than that of the latter sample in the overlapping X-ray luminosity range of both samples ( $10^{45} \lesssim L^{\text{int}}(2\text{--}10\ \text{keV}) \lesssim 10^{45.9}\ \text{erg/s}$ ). The fit is dominated by the "high-luminosity sample, owing to the much denser sampling in this region, and the difference between the bended fit of Stern (2015) and the straight fit of, e.g., Mateos et al. (2015) is  $\sim 0.8$  dex in MIR luminosity at  $L^{\text{int}}(2\text{--}10\ \text{keV}) \sim 10^{45.5}\ \text{erg/s}$ . Clearly, a better sampling at these luminosities is required to resolve this mismatch.

### 5.3.3 Radio-loud sources – Hardcastle et al. (2009) and Mason et al. (2012)

Hardcastle, Evans & Croston (2009) investigate multiwavelength correlations for radio-loud AGN, namely the low-redshift 3CCR sources. In this analysis, they use the restframe  $15\ \mu\text{m}$  global luminosity measured by *Spitzer*. The absorption corrected restframe  $2\text{--}10\ \text{keV}$  luminosities are split into an unabsorbed, jet-related and an absorbed, accretion-related component. They find that the MIR luminosity is only weakly correlated with the jet-related X-ray luminosity, while the former correlates much stronger with the

accretion-related component. The correlation is fitted to 36 objects with an unspecified Bayesian code that takes into account errors and upper limits, similar to `linmix_err`. The resulting slope is  $1.03 \pm 0.18$  and thus fully consistent with our results (Fig. 22). Unfortunately, the data of Hardcastle, Evans & Croston (2009) do not provide a good coverage at low luminosities and show a large scatter. Thus, it is not possible to use them to directly compare to our finding of radio-loud AGN differing from the correlation of radio-quiet sources. However, the results of Hardcastle, Evans & Croston (2009) are consistent with the jet increasingly contributing to the X-ray emission at high luminosities, which would explain the on average lower MIR–X-ray ratios of high luminosity radio-loud sources.

Mason et al. (2012) used the correlation found from combining the samples of Gandhi et al. (2009) and Levenson et al. (2009) to probe the position of the local low-luminosity AGN in the MIR–X-ray plane. Different to Asmus et al. (2011), they find a significant MIR-excess for those sources, in particular the radio-loud ones. Our work includes all the sources of these works and verifies this MIR-excess (Sect. 4.6), although with a smaller strength. This difference is mainly caused by differences in the  $2\text{--}10\ \text{keV}$  luminosities used, which can be very uncertain owing to the intrinsic faintness of low-luminosity AGN. For example, Mason et al. (2012) uses  $\log L^{\text{int}}(2\text{--}10\ \text{keV}) = 40.0$  for M 87 (NGC 4486) and a distance of 16 Mpc based on the Perlman & Wilson (2005) of *Chandra* observations from 2000. However, Donato, Sambruna & Gliozzi (2004) calculate  $\log L^{\text{int}}(2\text{--}10\ \text{keV}) = 40.6$  from the same observation for the same distance. Furthermore, the *Chandra* observation of 2002 analysed by González-Martín et al. (2009b) show an even higher value of  $\log L^{\text{int}}(2\text{--}10\ \text{keV}) = 40.9$ . Therefore, the long-term average X-ray luminosity is a factor of a few higher than the value used by Mason et al. (2012). M 87 is one of the objects with the strongest MIR-excess in that work.

### 5.3.4 Correlations with hardest X-rays – Mullaney et al. 2011, Matsuta et al. (2012), Ichikawa et al. (2012) and Sazonov et al. (2012)

Mullaney et al. (2011) was the the first to make use of the *Swift*/BAT data to probe the MIR–X-ray correlation in the hardest X-ray regime. They cross-matched the nine-month BAT AGN catalogue with the *IRAS* source catalogue and used those 44 objects with detections in all four *IRAS* bands for fitting the correlation. Before, they applied an SED fitting routine to isolate the AGN contribution in the large aperture *IRAS* data. They obtain a flatter but still marginally consistent correlation slope of  $0.74 \pm 0.13$  and a significantly higher intercept of  $0.37 \pm 0.08$  compared to our result. Unfortunately, no detailed information is given about the fitting algorithm or sources used for the fitting. Therefore, it is difficult to address the cause for the different correlation parameters. However, as Mullaney et al. (2011) note, their SED fitting procedure tends to over-estimate the AGN contribution at low luminosities. We thus suspect that their lower MIR luminosities are still affected by host emission. In addition, the next two works find higher slopes and lower intercepts for the BAT AGN based on higher resolution MIR data.

Matsuta et al. (2012) and Ichikawa et al. (2012) also use the *Swift*/BAT AGN catalogues to investigate the MIR–X-ray correlation at hardest X-rays but using MIR data from the most recent infrared satellites. Matsuta et al. (2012) utilizes the *AKARI* all-sky survey while Ichikawa et al. (2012) also uses *IRAS* and *WISE* data. On the other hand, Matsuta et al. (2012) cross-correlates with the

22-month BAT sample arriving at 158 AGN, while Ichikawa et al. (2012) starts with the nine-month BAT sample arriving at 128 objects. Compared to Mullaney et al. (2011) and this work, these studies have the advantage of a higher coverage of the flux-limited BAT samples but suffer again by a biases towards non-CT and higher-luminosity sources, as already discussed in Sect. 5.2.1. Both works find strong correlations of the observed 14–195 keV luminosities with the 9 and 18  $\mu\text{m}$  luminosities, and a weaker but significant one with the 90  $\mu\text{m}$  luminosities. Matsuta et al. (2012) uses the bisector method for fitting of the correlation. If we apply the same method to our reliable sample with  $\log N_{\text{H}} < 24$ , we get a slope of  $0.97 \pm 0.04$  and an intercept of  $-0.18 \pm 0.05$ . Therefore, the found correlation slopes of Matsuta et al. (2012) are slightly flatter but fully consistent with our results, while the intercept is  $\sim 0.3$  dex higher. These differences are presumably caused by host contamination affecting their low-resolution MIR data. Unfortunately, Ichikawa et al. (2012) does not state the exact fitting algorithm used so an accurate comparison is not possible. However, their fit is consistent with all our fits, bisector or `linmix_err`. The similarity of the correlations between 9, 18 and 22  $\mu\text{m}$  as found in Matsuta et al. (2012) and Ichikawa et al. (2012) and 12 and 18  $\mu\text{m}$  in this work indicate that the difference in wavelengths contributes at most 0.1 dex in this wavelength region (at least between  $\sim 8$  to 24  $\mu\text{m}$ ). Furthermore, Matsuta et al. (2012) also fits the radio-loud sources in their sample only, also finding the trend of a flatter slope similar to our work.

Finally, Sazonov et al. (2012) used a cleaned AGN sample from the *INTEGRAL* all-sky survey also observed with *Spitzer* to determine the MIR–X-ray correlation between the 15  $\mu\text{m}$  and observed 17–60 keV wavebands. They find

$$\log\left(\frac{L^{\text{Spi}}(15\mu\text{m})}{10^{43}\text{erg s}^{-1}}\right) = (0.23 \pm 0.04) + (0.74 \pm 0.06) \log\left(\frac{L^{\text{obs}}(17\text{--}60\text{ keV})}{10^{43}\text{erg s}^{-1}}\right), \quad (5)$$

which is significantly flatter than our correlation (Fig. 22) and also the correlations found by Matsuta et al. (2012) and Ichikawa et al. (2012) but in good agreement with Mullaney et al. (2011). Unfortunately, Sazonov et al. (2012) does not state which algorithm was used exactly but likely it was ordinary least square fitting with  $L^{\text{obs}}(17\text{--}60\text{ keV})$  as independent variable. The overlap with our reliable sample is only 33 objects (54 per cent of their clean sample). Thus, we can not robustly calculate the  $L^{\text{nuc}}(12\mu\text{m})$ – $L^{\text{obs}}(14\text{--}195\text{ keV})$  correlation for their sample.

Similar to the BAT samples, the *INTEGRAL* sample also under-represents lower luminosities and is dominated by sources with  $\log L^{\text{obs}}(17\text{--}60\text{ keV}) \gtrsim 43$ . In fact, the only low-luminosity source ( $\log L^{\text{obs}}(17\text{--}60\text{ keV}) < 42$ ) in their sample that is not star formation dominated is NGC 4395. They exclude this object from most analysis because as a high Eddington system with a small black hole mass in a dwarf galaxy it might belong to a physically different class of AGN. However our continuous coverage down to the low-luminosity level of NGC 4395 does not indicate any significant difference between this object and other more massive low-luminosity AGN. Including NGC 4395 into the fitting to their sample results in a formally stronger correlation with a steeper slope that would be consistent with our  $L^{\text{nuc}}(12\mu\text{m})$ – $L^{\text{obs}}(14\text{--}195\text{ keV})$  correlation. The intercept is still  $\sim 0.3$  dex higher in that case, which is at least partly caused by host contamination of their *Spitzer* data as indicated by the median ratio of  $F^{\text{nuc}}(12\mu\text{m})$  over  $F^{\text{Spi}}(15\mu\text{m})$  of 0.65. This contamination likely also affects the slope of the correlation or decrease of MIR–X-ray ratio with increasing luminosity as Sazonov et al. found (their Fig. 3). Specifically, all but

one (Cygnus A) of the eight sources overlapping with our reliable sample with  $F^{\text{nuc}}(12\mu\text{m})/F^{\text{Spi}}(15\mu\text{m}) < 0.46$  (median - standard deviation) are between  $\sim 42 < \log L^{\text{obs}}(17\text{--}60\text{ keV}) < 43.5$ , which is the region where  $L^{\text{Spi}}(15\mu\text{m})/L^{\text{obs}}(17\text{--}60\text{ keV})$  is largest in their sample.

Sazonov et al. (2012) pointed out that the correlation slopes might flatten at high luminosities ( $\log L^{\text{obs}}(17\text{--}60\text{ keV}) \gtrsim 44$ ), which is the reason they find flatter slopes compared to Gandhi et al. (2009). Our coverage at high luminosities is better compared to both works but still we did not find compelling evidence for a decrease in the MIR–X-ray ratio (Sect. 4.3). Furthermore, a flattening appears to be inconsistent with Fiore et al. (2009), unless the 2–10 keV and 14–195 keV or 5.8 and 12  $\mu\text{m}$  wavebands decouple at high luminosities.

Finally, we note that the four NLS1 sources in Sazonov et al. (2012; none in common with our sample) do not show significantly higher MIR–X-ray ratios than the rest of their sample, contrary to what we find for our sample.

In summary, our results are in general consistent with all previous works focusing on low to moderate luminosity AGN while there appears to be significant differences to studies focusing on high luminosity sources, whereas both flatter and steeper slopes are found (mainly for type I AGN). However, the most recent comprehensive study focusing on high luminosities does not find any change in slope, validating our result (Mateos et al. 2015).

#### 5.4 Implications for the torus scenario

Current clumpy and smooth torus models (e.g., Nenkova et al. 2008; Hönig & Kishimoto 2010; Stalevski et al. 2012) predict differences of  $\sim 0.3$  dex in the MIR–X-ray ratio with changing inclination angles assuming isotropic X-ray/UV emission. This is however not found in our results neither in Section 4.4 nor in Section 4.5 which show that differences between unobscured and highly obscured objects are at best small ( $< 0.1$  dex). Only when entering the Compton-thick obscuration regime, the MIR–X-ray ratio seems to further decrease by  $\sim 0.15$  dex owing to strong absorption also in the MIR (intrinsic or foreground). This small difference could be explained in three ways. First, the X-ray emission could be anisotropic as indicated by comparison to [O IV] emission coming presumably from the narrow line region (Liu et al. 2014). Then, the anisotropy of the MIR and X-ray emission would have roughly a similar dependence on the orientation angle as recently found by Yang, Wang & Liu (2015). Second, as the most recent interferometric results indicate, the majority of MIR emission is actually produced in the polar outflow region rather than in a canonical torus (Hönig et al. 2012, 2013; Tristram et al. 2014). In that case, the MIR anisotropy between face-on and edge-on systems is possibly much lower. Third, higher obscured objects could have on average higher covering factors (Ramos Almeida et al. 2011; Elitzur 2012), which could mitigate differences. However, this effect is expected to be strongest in the high obscuration regime where we do find larger differences in the MIR–X-ray ratio. Another interesting claim is that the X-ray reflection component is possibly larger in many objects with  $\log N_{\text{H}} > 23$  (Ricci et al. 2011), which would lead to a lower MIR–X-ray ratio for affected sources, at least in the 14–195 keV band.

The largest MIR–X-ray ratios and differences to the other subsamples are exhibited by objects with intermediate columns,  $22 \lesssim \log N_{\text{H}} \lesssim 23$  (Sect. 4.5; Fig. 17). The surprising increase from low to intermediate  $N_{\text{H}}$  can possibly be explained by a deficit of warm dust in the least obscured AGN. Indeed unobscured ob-

jects with a blue MIR spectral energy distribution in Asmus et al. (2014) display on average lower MIR–X-ray ratios than those with an emission peak at  $\sim 18 \mu\text{m}$ . Many of the latter have intermediate X-ray column densities. Such a behaviour is in fact predicted by Hönlig & Kishimoto (2010) where the contribution of the MIR emission to the bolometric luminosity depends on the distribution of the dust and blue MIR spectral slopes would come from a compact distribution with most of the emitting dust mass confined close to the sublimation radius (see also Hönlig et al. 2010). Note that this explanation is independent of the obscuring fraction or opening angle and does not depend on the accretion luminosity.

It is curious that the decrease in the MIR–X-ray ratio from intermediate to high  $N_{\text{H}}$  occurs around  $10^{23} \text{cm}^{-2}$ , which is the value for which the obscuration in the MIR becomes optically thick assuming a standard gas to dust ratio of 100. Therefore, self-obscuration in the torus or foreground absorption in the host might play a role here. In fact, we caution the reader concerning the direct application of these results to torus models because this MIR–X-ray analysis does not separate between AGN-intrinsic and foreground, host obscuration. The latter can be a large contributor to the measured column densities (e.g., Hönlig et al. 2014).

The uncertainties in both the host contribution to the obscuration and the isotropy of the MIR and X-ray emission does prevent us from making any statements about the obscuring fraction or opening angle and their dependencies on luminosity or object type.

At the same time, systematics dominate the uncertainties on the correlation slope and only allow constraining it to between 0.9 and 1 (Sections. 4.1, 4.2, and 4.3). Thus, the uncertainties are still too large to draw strong conclusions on bolometric corrections and underlying physics. We note however that the MIR–X-ray correlation slope  $\leq 1$  together with the previous findings that  $L^{\text{int}}(2\text{-}10 \text{ keV}) \propto L(\text{UV})^\beta$  with  $\beta \approx 0.85$  (Marchese et al. 2012b) imply that  $L^{\text{nuc}}(12 \mu\text{m}) \propto L(\text{UV})^{\beta'}$  with  $\beta' < 0.85$ , assuming a similar geometry for the MIR, X-ray and UV emitters.

### 5.5 The MIR–X-ray correlation as a tool to predict $N_{\text{H}}$ and $L^{\text{int}}(2\text{-}10 \text{ keV})$

The tightness of the MIR–X-ray correlation for all AGN types suggests that high angular resolution MIR data can be used to predict or constrain the column densities and luminosities in X-rays irrespective of the object nature. In particular for highly obscured (Compton-thick) objects or those with low S/N X-ray data, it is often difficult to reliably estimate these properties.

In Fig. 23,  $N_{\text{H}}$  is plotted versus the ratio of observed MIR to X-ray fluxes for the reliable sample. The MIR–X-ray ratio stays constant with increasing column density up to  $\log N_{\text{H}} = 22.8$  and then increases with growing  $N_{\text{H}}$ . The threshold is here determined from the intrinsic to observed 2-10 keV flux ratio, which increases for higher values, which is visible in the median ratio and through a double-sided KS test. For the latter, the sub-samples above and below  $\log N_{\text{H}} = 22.8$  show maximal difference ( $D_{\text{KS}} = 0.91$ ;  $\log p_{\text{KS}} = -21.38$ ). This fact motivates us to only regard those objects with  $\log N_{\text{H}} > 22.8$  for the  $N_{\text{H}}$ -diagnostic, which conversely is blind to lower column densities than that, i.e. the 2-10 keV emission is only affected by obscuration above this threshold. For the corresponding sub-sample of 53 reliable AGN with higher column densities,  $N_{\text{H}}$  and  $\log F^{\text{nuc}}(12 \mu\text{m}) - \log F^{\text{obs}}(2\text{-}10 \text{ keV})$  show a significant correlation ( $\rho_{\text{S}} = 0.60$ ;  $\log p_{\text{S}} = -5.6$ ). A corresponding `linmix_err` fit

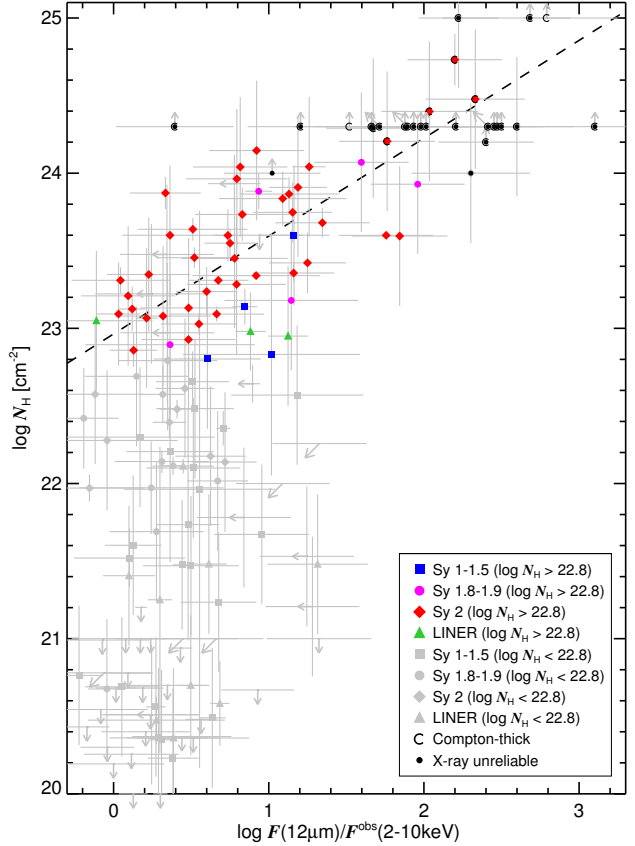


**Figure 23.** X-ray column density diagnostic:  $N_{\text{H}}$  versus the observed  $12 \mu\text{m}$  to 2-10 keV flux ratio. Symbols are as in Fig. 3. All coloured symbols are reliable AGN with  $\log N_{\text{H}} > 22.8$  and have been used for the `linmix_err` fit displayed as dashed line. All remaining sources from the reliable sample are plotted in grey. In addition, 22 unreliable AGN from the AGN MIR atlas that are Compton-thick or CT candidates are marked with small filled black circles. See text for further explanation.

yields:

$$\log\left(\frac{N_{\text{H}}}{10^{22.8} \text{cm}^{-2}}\right) = (0.14 \pm 0.11) + (0.67 \pm 0.12) \log\left(\frac{F^{\text{nuc}}(12 \mu\text{m})}{F^{\text{obs}}(2\text{-}10 \text{ keV})}\right), \quad (6)$$

or for convenient use in directly measured quantities:

$$\log\left(\frac{N_{\text{H}}}{\text{cm}^{-2}}\right) = (14.37 \pm 0.11) + (0.67 \pm 0.11) \log\left(\frac{F^{\text{nuc}}(12 \mu\text{m}) \text{ erg/s/cm}^2}{F^{\text{obs}}(2\text{-}10 \text{ keV}) \text{ mJy}}\right) \quad (7)$$

This equation allows in principle predicting  $N_{\text{H}}$  to within 0.32 dex (the observed  $1\text{-}\sigma$  scatter from this correlation) for significantly obscured objects. The caveat is that owing to the constancy of  $\log F^{\text{nuc}}(12 \mu\text{m}) - \log F^{\text{obs}}(2\text{-}10 \text{ keV})$  for  $\log N_{\text{H}} < 22.8$ , this diagnostic has in practise only predictive power for  $\log F^{\text{nuc}}(12 \mu\text{m}) - \log F^{\text{obs}}(2\text{-}10 \text{ keV}) \gtrsim 0.64$  (median + STDDEV), corresponding to  $\log N_{\text{H}} \gtrsim 23.36$ . A similar plot but using low-resolution MIR photometry is also discussed in Brightman & Nandra (2011; their Sect. 5, Fig. 12). The low angular resolution leads to a shift in the observed  $12 \mu\text{m}$ –2-10 keV distribution by 0.5 to 1 dex and an increased scatter owing to significant host contamination with re-



spect to our results. According to the findings of Asmus et al. (2014), low angular resolution MIR data can only be reliably used for this  $N_H$  diagnostic for objects with  $\log L^{\text{mic}}(12\mu\text{m}) \gtrsim 44$ , i.e., where the AGN mostly dominates the total MIR emission. Another comparable diagnostic is introduced by Severgnini, Caccianiga & Della Ceca (2012), using the X-ray hardness ratio to better isolate CT objects.

The intrinsic 2–10 keV luminosity can directly be estimated from Eq. 2. The uncertainty of this  $L^{\text{int}}(2\text{--}10\text{ keV})$  prediction is 0.32 dex (the observed 1- $\sigma$  scatter from the correlation). In Appendix B1, we use these derived tools to predict the intrinsic 2–10 keV luminosities and column densities of objects with uncertain X-ray properties.

Using the MIR–X-ray correlation itself as a diagnostic, we find that in most of AGN/starburst composite objects from the atlas the AGN MIR emission is well isolated at subarcsecond scales with the caveat that this diagnostic by itself can not distinguish between Compton-thick obscured AGN and star formation dominated nuclei. More details are given in Appendix B2 including a discussion of the largest outlier, the complex object NGC 4945 with a very low MIR–X-ray ratio, which can at least be partly explained by particularly high foreground extinction affecting the MIR. However, our results indicate that it is unlikely that many objects are significantly affected by this. Finally, we test the AGN nature of the uncertain objects from the AGN MIR atlas in Appendix B3.

### 5.6 True type II AGN and the MIR–X-ray correlation

The idea of so-called true type II AGN is based observationally on the absence of broad emission lines in polarized light (but see Antonucci 2012) and the absence of significant X-ray absorption in many type II AGN (Ptak et al. 1996; Pappa et al. 2001; Panessa & Bassani 2002). Theoretically, the disappearance of the broad line region has been predicted to occur at low accretion rates (Nicastrò 2000; Nicastrò, Martocchia & Matt 2003). Many candidates for true type II AGN were claimed over the years. However, most of them could later be shown to be either Compton-thick obscured, star formation dominated, or to show in fact broad emission line components (Shi et al. 2010). The best remaining candidates among the local galaxies are NGC 3147 and possibly NGC 3660. However, the optical classifications for NGC 3660 are very contradicting ranging from anything between non-AGN to type I AGN (Kollatschny et al. 1983; Contini, Considero & Davoust 1998; Moran, Halpern & Helfand 1996; Véron-Cetty & Véron 2010). Note that Shi et al. (2010) also suggests NGC 4594 but this low-luminosity object is usually classified as LINER or as Sy 1.9 (Véron-Cetty & Véron 2010). While not strictly demanded by definition, many works suggest that not only the broad line region but also the obscuring dusty structure is absent in true type II AGN. Therefore, it is interesting to test whether the candidates found so far exhibit particularly low MIR–X-ray ratios. NGC 3147, NGC 3660 and NGC 4594 are all in the AGN MIR atlas. Their nuclear MIR–X-ray ratios are  $R_X^M = 0.35$ ; 0.38; and 0.1 respectively. Therefore, there is no evidence from the MIR point of view for the absence of a dusty obscurer or any other deviation from the other AGN for these objects.

For completeness we also regard two more distant candidates that are not included into the AGN MIR atlas. These are GSN 069 (Miniutti et al. 2013) and Q2131-427 (Panessa et al. 2009; Bianchi et al. 2012). For both we use the band 3 fluxes of the Wide-field Infrared Survey Explorer (*WISE*; Wright et al. 2010) as a proxy for the nuclear 12  $\mu\text{m}$  emission. The MIR–X-ray ratio of GSN 069 is

$R_X^M \leq 1$  (it was not detected in the 2–10 keV range; Miniutti et al. 2013). This is well consistent with the presence of warm dust as in normal type II AGN with the caveat that the *WISE* data might be host contaminated. Note that GSN 069 has an extremely soft X-ray spectrum and thus 2–10 keV might not be a good intrinsic indicator in this case.

The closest *WISE* source to Q2131-427 has a W3 magnitude of 12.645 (distance 2.6 arcseconds). There is no other source within the confusion limit of *WISE*. Using the 2–10 keV flux stated by Panessa et al. (2009), the corresponding MIR–X-ray ratio is  $R_X^M = 0.46$ . Since the luminosity is  $\approx 10^{44}$  erg/s, significant star formation contamination is unlikely (Asmus et al. 2011).

We conclude that all true type II AGN candidates exhibit MIR–X-ray ratios typical of normal type II AGN and thus do not show any evidence for the absence of a dusty obscurer.

### 5.7 Double AGN and the MIR–X-ray correlation

During major mergers it is expected that the nuclei of both galaxies become active at some point during the process and temporarily form a binary AGN before finally the super massive black holes merge (Begelman, Blandford & Rees 1980). This is one proposed way for black hole growth during the cosmic evolution. Here, we address the question whether these double and binary AGN also follow the same MIR–X-ray correlation as single AGN. One would expect deviations to occur latest as soon as the influence of the other AGN component starts to change the AGN structure. But also the infall process during the merger could lead significant changes in the structure already, which should be indicated by deviating MIR–X-ray ratios.

However, only very few double or binary AGN have been found so far (e.g., Wang & Gao 2010), with Mrk 463 (Hutchings & Neff 1989) and NGC 6240 (Komossa et al. 2003) still being the best cases.

The MIR AGN atlas contains three double AGN candidates, Mrk 266, NGC 3690 and NGC 6240. Their X-ray properties are described in detail in Appendix B4. All are major merger systems, show intense star formation and are heavily obscured along the line of sight. These complicate extracting the X-ray and MIR properties of the AGN. For Mrk 266, only for one nucleus an intrinsic X-ray luminosity is available (Mrk 266NE), placing it at a relatively high MIR–X-ray ratio ( $R_X^M = 1.22$ ). However, the nucleus is presumably CT obscured, which would move it to a much lower ratio. This is in fact the case for both NGC 3690 and NGC 6240 where the more powerful and X-ray brighter nucleus is CT obscured with average to low MIR–X-ray ratios (NGC 3690W:  $R_X^M = 0.49$  and NGC 6240S:  $R_X^M = -0.52$ ). The low ratio of NGC 6240S might indicate significant absorption also in the MIR, similar to NGC 4945 (Appendix B2). For both systems, the fainter nuclei might also be CT obscured. But while NGC 6240N still has a nominal MIR–X-ray ratio ( $R_X^M = 0.77$ ), the one of NGC 3690E is as high as for pure star formation ( $R_X^M = 3.57$ ). Therefore, the latter object might be star formation dominated also on nuclear scales (see also Alonso-Herrero et al. 2013), unless it is highly CT obscured.

Note that for another object in the AGN MIR atlas, NGC 3393, a double AGN was claimed based on *Chandra* observations (Fabiano et al. 2011). However, the existence of a double AGN in this regular face-on spiral is disfavoured in a recent multiwavelength analysis also using new *NuSTAR* data (Koss et al. 2015). Only a single nucleus was also detected in the MIR (Asmus et al. 2014).

In summary, the individual AGN in the double AGN have MIR–X-ray ratios consistent with single AGN but intense star for-

mation and high obscuration makes accurate measurements difficult. Additional high angular resolution data, in particular MIR spectra (e.g., Alonso-Herrero et al. 2013, 2014) can help to better isolate the intrinsic AGN power in these systems.

## 6 CONCLUSIONS

We presented an updated determination of the MIR–X-ray correlation for AGN using the subarcsecond scale 12 and 18  $\mu\text{m}$  photometry from Asmus et al. (2014) and averaged X-ray properties from the most recent observations collected from the literature. Starting from the atlas sample of 253 AGN, we selected 152 objects with reliable AGN classification, no AGN/starburst composites, and trustworthy X-ray properties. This sample is not obviously biased against highly obscured objects, and although we exclude many CT object from the analysis because of unreliable  $L^{\text{int}}$  (2–10 keV) estimates, their MIR–X-ray ratios agree well with the results summarized below (see App. B1). In particular, we obtained the following main results:

(i) An MIR–X-ray correlation is present in flux and luminosity space, extending over the whole probed range from  $\sim 10^{40}$  to  $\sim 10^{45}$  erg/s. The correlation is strong for any combinations of 12 and 18  $\mu\text{m}$  and 2–10 and 14–195 keV and likely even extends to shorter (and longer) MIR wavelengths as indicated in the literature already. Its slope is between 0.9 and 1.0 depending on the exact wavelengths and samples used while the observed scatter is always  $< 0.4$  dex. Therefore, the MIR–X-ray correlation is a useful tool to convert between X-ray and MIR luminosities irrespective of the object nature and underlying physics.

(ii) *The observed MIR–X-ray ratio can be used to constrain the X-ray column density within 0.32 dex.*

(iii) There is indication for a decrease of the MIR–X-ray ratio at the highest probed X-ray luminosities ( $\sim 10^{45}$  erg/s) but remains statistically insignificant. Such a turn over would agree with the decrease of the dust covering factor and the results of Sazonov et al. (2012) but in contradiction to Fiore et al. (2009) and Stern (2015). A well defined sufficiently large high luminosity sample needs to be studied in order to solve this conflict.

(iv) Differences with optical type are small. The correlation for type I AGN is tightest and type II objects dominate the scatter in the correlation of all AGN. *Optical type I AGN display on average an only 0.15 dex higher MIR–X-ray ratio compared to optical type II AGN*, while their correlation slopes are parallel. LINERs exhibit on average the highest MIR–X-ray ratio and have a flatter correlation slope, which is explained by their radio-loudness (see below). These differences remain statistically insignificant however.

(v) *True type II AGN candidates show the same MIR–X-ray ratios as normal type II AGN* and, thus, do not indicate any deficit of dust (and obscurer) in those objects.

(vi) The MIR–X-ray ratios of the individual AGN in double AGN systems are consistent with the MIR–X-ray correlation but intense star formation and heavy obscuration make measurements very uncertain.

(vii) *Only the NLS1 objects are significantly different with very high MIR–X-ray ratios.* However, the MIR–X-ray properties of a larger sample of NLS1 have to be studied for more conclusive results.

(viii) The differences between X-ray obscured and unobscured AGN are smaller ( $< 0.1$  dex) than expected from torus models but can be explained by either an anisotropy in the X-ray emission or the MIR emission being dominated by dust in the outflow region.

*Only CT sources have significantly lower MIR–X-ray ratios than unobscured AGN.* AGN with intermediate obscuration show the highest MIR–X-ray ratio which is possibly related to a deficit of warm dust in many unobscured AGN as indicated by their MIR spectral energy distributions.

(ix) *Radio-loud AGN differ from radio-quiet AGN also in the MIR–X-ray plane in having a significantly flatter correlation slope* leading to higher MIR–X-ray ratios at low luminosities and lower ratios at high luminosities. This can be explained by an additional MIR contribution or dominance of the jet at low luminosities while the jet contributes much more to the X-rays at higher luminosities.

## ACKNOWLEDGEMENTS

We thank the referee for valuable comments that improved the manuscript. D.A. acknowledges the JAXA ITYF scheme for visitor support to ISAS in Aug 2012. P.G. acknowledges support from STFC (grant reference ST/J003697/1). This research made use of the NASA/IPAC Extragalactic Database (NED), which is operated by the Jet Propulsion Laboratory, California Institute of Technology, under contract with the National Aeronautics and Space Administration. This work made use of data supplied by the UK Swift Science Data Centre at the University of Leicester. This publication makes use of data products from the Wide-field Infrared Survey Explorer, which is a joint project of the University of California, Los Angeles, and the Jet Propulsion Laboratory/California Institute of Technology, funded by the National Aeronautics and Space Administration.

## REFERENCES

- Akylas A., Georgantopoulos I., 2009, *A&A*, 500, 999  
 Alonso-Herrero A. et al., 2014, *MNRAS*, 443, 2766  
 Alonso-Herrero A. et al., 2013, *The ApJL*, 779, L14  
 Andrade-Velázquez M., Krongold Y., Elvis M., Nicastro F., Brickhouse N., Binette L., Mathur S., Jiménez-Bailón E., 2010, *ApJ*, 711, 888  
 Antonucci R., 2012, arXiv:1210.2716  
 Arévalo P. et al., 2014, *ApJ*, 791, 81  
 Arnaud K. A., 1996, in , p. 17  
 Ashton C. E., Page M. J., Branduardi-Raymont G., Blustein A. J., 2006, *MNRAS*, 366, 521  
 Asmus D., Gandhi P., Smette A., Hönig S. F., Duschl W. J., 2011, *A&A*, 536, 36  
 Asmus D., Hönig S. F., Gandhi P., Smette A., Duschl W. J., 2014, *MNRAS*, 439, 1648  
 Awaki H. et al., 2008, *PASJ*, 60, 293  
 Awaki H., Murakami H., Ogawa Y., Leighly K. M., 2006, *ApJ*, 645, 928  
 Awaki H., Ueno S., Koyama K., Tsuru T., Iwasawa K., 1996, *PASJ*, 48, 409  
 Awaki H., Ueno S., Taniguchi Y., Weaver K. A., 2000, *ApJ*, 542, 175  
 Baldi A., Forman W., Jones C., Kraft R., Nulsen P., Churazov E., David L., Giacintucci S., 2009, *ApJ*, 707, 1034  
 Balestra I., Bianchi S., Matt G., 2004, *A&A*, 415, 437  
 Ballo L., Braitto V., Della Ceca R., Maraschi L., Tavecchio F., Dadina M., 2004, *ApJ*, 600, 634  
 Balmaverde B., Capetti A., Grandi P., 2006, *A&A*, 451, 35  
 Baloković M. et al., 2014, *ApJ*, 794, 111

- Barvainis R., Lonsdale C., Antonucci R., 1996, *AJ*, 111, 1431
- Bassani L., Dadina M., Maiolino R., Salvati M., Risaliti G., della Ceca R., Matt G., Zamorani G., 1999, *ApJSS*, 121, 473
- Bauer F. E. et al., 2014, arXiv:1411.0670 [astro-ph], arXiv: 1411.0670
- Baumgartner W. H., Tueller J., Markwardt C. B., Skinner G. K., Barthelmy S., Mushotzky R. F., Evans P. A., Gehrels N., 2013, *ApJSS*, 207, 19
- Beckmann V., Gehrels N., Shrader C. R., Soldi S., 2006, *ApJ*, 638, 642
- Beckmann V. et al., 2009, *A&A*, 505, 417
- Begelman M. C., Blandford R. D., Rees M. J., 1980, *Nature*, 287, 307
- Bianchi S., Bonilla N. F., Guainazzi M., Matt G., Ponti G., 2009a, *A&A*, 501, 915
- Bianchi S., Corral A., Panessa F., Barcons X., Matt G., Bassani L., Carrera F. J., Jiménez-Bailón E., 2008a, *MNRAS*, 385, 195
- Bianchi S., Guainazzi M., Chiaberge M., 2006, *A&A*, 448, 499
- Bianchi S., La Franca F., Matt G., Guainazzi M., Jimenez Bailón E., Longinotti A. L., Nicastro F., Pentericci L., 2008b, *MNRAS*, 389, L52
- Bianchi S., Matt G., Balestra I., Guainazzi M., Perola G. C., 2004, *A&A*, 422, 65
- Bianchi S., Matt G., Balestra I., Perola G. C., 2003, *A&A*, 407, L21
- Bianchi S., Miniutti G., Fabian A. C., Iwasawa K., 2005, *MNRAS*, 360, 380
- Bianchi S. et al., 2012, *MNRAS*, 426, 3225
- Bianchi S., Piconcelli E., Chiaberge M., Bailón E. J., Matt G., Fiore F., 2009b, *ApJ*, 695, 781
- Blanton E. L., Sarazin C. L., Irwin J. A., 2001, *ApJ*, 552, 106
- Boller T., Gallo L. C., Lutz D., Sturm E., 2002, *MNRAS*, 336, 1143
- Braitto V., Ballo L., Reeves J. N., Risaliti G., Ptak A., Turner T. J., 2013, *MNRAS*, 428, 2516
- Braitto V. et al., 2003, *A&A*, 398, 107
- Braitto V., Reeves J. N., Della Ceca R., Ptak A., Risaliti G., Yaqoob T., 2009, *A&A*, 504, 53
- Braitto V., Reeves J. N., Sambruna R. M., Gofford J., 2011, *MNRAS*, 414, 2739
- Brenneman L. W. et al., 2014, *ApJ*, 788, 61
- Brenneman L. W. et al., 2011, *ApJ*, 736, 103
- Brenneman L. W., Risaliti G., Elvis M., Nardini E., 2013, *MNRAS*, 429, 2662
- Brightman M., Nandra K., 2008, *MNRAS*, 390, 1241
- Brightman M., Nandra K., 2011a, *MNRAS*, 413, 1206
- Brightman M., Nandra K., 2011b, *MNRAS*, 414, 3084
- Brinkmann W., Grupe D., Branduardi-Raymont G., Ferrero E., 2003, *A&A*, 398, 81
- Burrows D. N. et al., 2005, *Space Science Reviews*, 120, 165
- Capetti A., Balmaverde B., 2005, *A&A*, 440, 73
- Cappi M. et al., 2006, *A&A*, 446, 459
- Cardaci M. V., Santos-Lleó M., Krongold Y., Hägele G. F., Díaz A. I., Rodríguez-Pascual P., 2009, *A&A*, 505, 541
- Castangia P., Panessa F., Henkel C., Kadler M., Tarchi A., 2013, *MNRAS*, 436, 3388
- Chernyakova M. et al., 2007, *A&A*, 465, 147
- Coffey D. et al., 2014, *MNRAS*, 443, 1788
- Comastri A., Iwasawa K., Gilli R., Vignali C., Ranalli P., Matt G., Fiore F., 2010, *ApJ*, 717, 787
- Condon J. J., Cotton W. D., Broderick J. J., 2002, *AJ*, 124, 675
- Condon J. J., Cotton W. D., Greisen E. W., Yin Q. F., Perley R. A., Taylor G. B., Broderick J. J., 1998, *AJ*, 115, 1693
- Contini T., Considere S., Davoust E., 1998, *A&A Supplement Series*, 130, 285
- Cowperthwaite P. S., Reynolds C. S., 2012, *The ApJL*, 752, L21
- Cusumano G. et al., 2010, *A&A*, 524, 64
- Dadina M., 2007, *A&A*, 461, 1209
- Dadina M., Guainazzi M., Cappi M., Bianchi S., Vignali C., Malaguti G., Comastri A., 2010, *A&A*, 516, 9
- D’Ammando F., Bianchi S., Jiménez-Bailón E., Matt G., 2008, *A&A*, 482, 499
- de Rosa A., Bassani L., Ubertini P., Panessa F., Malizia A., Dean A. J., Walter R., 2008, *A&A*, 483, 749
- Della Ceca R. et al., 2002, *The ApJL*, 581, L9
- Della Ceca R., Pellegrini S., Bassani L., Beckmann V., Cappi M., Palumbo G. G. C., Trinchieri G., Wolter A., 2001, *A&A*, 375, 781
- Diamond-Stanic A. M., Rieke G. H., Rigby J. R., 2009, *ApJ*, 698, 623
- Donato D., Sambruna R. M., Gliozzi M., 2004, *ApJ*, 617, 915
- Dong H., Xue S.-J., Li C., Cheng F.-Z., 2004, *Chinese Journal of A&A*, 4, 427
- Ebrero J., Costantini E., Kaastra J. S., de Marco B., Dadina M., 2011, *A&A*, 535, 62
- Edelson R. A., 1987, *ApJ*, 313, 651
- Edelson R. A., Malkan M. A., 1986, *ApJ*, 308, 59
- Eguchi S., Ueda Y., Awaki H., Aird J., Terashima Y., Mushotzky R., 2011, *ApJ*, 729, 31
- Eguchi S., Ueda Y., Terashima Y., Mushotzky R., Tueller J., 2009, *ApJ*, 696, 1657
- Elitzur M., 2012, *The ApJL*, 747, L33
- Elvis M., Maccacaro T., Wilson A. S., Ward M. J., Penston M. V., Fosbury R. A. E., Perola G. C., 1978, *MNRAS*, 183, 129
- Emmanoulopoulos D., Papadakis I. E., McHardy I. M., Nicastro F., Bianchi S., Arévalo P., 2011, *MNRAS*, 415, 1895
- Eracleous M., Shields J. C., Chartas G., Moran E. C., 2002, *ApJ*, 565, 108
- Esquej P. et al., 2012, *MNRAS*, 423, 185
- Evans A. S. et al., 2008a, *The ApJL*, 675, L69
- Evans D. A. et al., 2008b, *ApJ*, 675, 1057
- Evans D. A., Hardcastle M. J., Croston J. H., Worrall D. M., Birkinshaw M., 2005, *MNRAS*, 359, 363
- Evans D. A., Hardcastle M. J., Lee J. C., Kraft R. P., Worrall D. M., Birkinshaw M., Croston J. H., 2008c, *ApJ*, 688, 844
- Evans D. A., Kraft R. P., Worrall D. M., Hardcastle M. J., Jones C., Forman W. R., Murray S. S., 2004, *ApJ*, 612, 786
- Evans D. A., Lee J. C., Kamenetska M., Gallagher S. C., Kraft R. P., Hardcastle M. J., Weaver K. A., 2006, *ApJ*, 653, 1121
- Evans D. A., Lee J. C., Turner T. J., Weaver K. A., Marshall H. L., 2007, *ApJ*, 671, 1345
- Evans P. A. et al., 2009, *MNRAS*, 397, 1177
- Fabbiano G. et al., 2003, *ApJ*, 588, 175
- Fabbiano G., Wang J., Elvis M., Risaliti G., 2011, *Nature*, 477, 431
- Fabian A. C., Miniutti G., Iwasawa K., Ross R. R., 2005, *MNRAS*, 361, 795
- Falcke H., Körding E., Markoff S., 2004, *A&A*, 414, 895
- Fiore F. et al., 2009, *ApJ*, 693, 447
- Fioretti V., Angelini L., Mushotzky R. F., Koss M., Malaguti G., 2013, *A&A*, 555, 44
- Flohic H. M. L. G., Eracleous M., Chartas G., Shields J. C., Moran E. C., 2006, *ApJ*, 647, 140
- Franceschini A. et al., 2003, *MNRAS*, 343, 1181

- Fruscione A., Greenhill L. J., Filippenko A. V., Moran J. M., Her-  
rnstein J. R., Galle E., 2005, *ApJ*, 624, 103
- Fukazawa Y. et al., 2011, *ApJ*, 727, 19
- Gallimore J. F., Beswick R., 2004, *AJ*, 127, 239
- Gallo L. C., 2006, *MNRAS*, 368, 479
- Gallo L. C., Grupe D., Schartel N., Komossa S., Miniutti G.,  
Fabian A. C., Santos-Lleo M., 2011, *MNRAS*, 412, 161
- Gallo L. C., Lehmann I., Pietsch W., Boller T., Brinkmann W.,  
Friedrich P., Grupe D., 2006, *MNRAS*, 365, 688
- Gandhi P., Fabian A. C., 2003, *MNRAS*, 339, 1095
- Gandhi P., Horst H., Smette A., Hönig S., Comastri A., Gilli R.,  
Vignali C., Duschl W., 2009, *A&A*, 502, 457
- Gandhi P. et al., 2014, *ApJ*, 792, 117
- Gandhi P., Yamada S., Ricci C., Asmus D., Mushotzky R. F., Ueda  
Y., Terashima Y., La Parola V., 2015, *MNRAS*, 449, 1845
- Ghosh H., Pogue R. W., Mathur S., Martini P., Shields J. C., 2007,  
*ApJ*, 656, 105
- Glass I. S., Moorwood A. F. M., Eichendorf W., 1982, *A&A*, 107,  
276
- Glasse A. C., Atad-Ettdgui E. I., Harris J. W., 1997, in *SPIE*, Vol.  
2871, *Optical Telescopes of Today and Tomorrow*, pp. 1197–  
1203
- Gliozzi M., Papadakis I. E., Sambruna R. M., 2008, *ApJ*, 678, 78
- Gliozzi M., Sambruna R. M., Brandt W. N., Mushotzky R., Era-  
cleous M., 2004, *A&A*, 413, 139
- Gliozzi M., Sambruna R. M., Eracleous M., Yaqoob T., 2007, *ApJ*,  
664, 88
- Gofford J. et al., 2011, *MNRAS*, 414, 3307
- Golombek D., Miley G. K., Neugebauer G., 1988, *AJ*, 95, 26
- Gondoin P., Orr A., Lumb D., 2003, *A&A*, 398, 967
- González-Martín O., Masegosa J., Márquez I., Guainazzi M.,  
2009a, *ApJ*, 704, 1570
- González-Martín O., Masegosa J., Márquez I., Guainazzi M.,  
Jiménez-Bailón E., 2009b, *A&A*, 506, 1107
- González-Martín O., Masegosa J., Márquez I., Guerrero M. A.,  
Dultzin-Hacyan D., 2006, *A&A*, 460, 45
- González-Martín O. et al., 2013, *A&A*, 553, 35
- Goodger J. L., Hardcastle M. J., Croston J. H., Kassim N. E., Per-  
ley R. A., 2008, *MNRAS*, 386, 337
- Greenhill L. J., Tilak A., Madejski G., 2008, *The ApJL*, 686, L13
- Gregory P. C., Condon J. J., 1991, *ApJSS*, 75, 1011
- Gregory P. C., Vavasour J. D., Scott W. K., Condon J. J., 1994,  
*ApJSS*, 90, 173
- Grier C. J., Mathur S., Ghosh H., Ferrarese L., 2011, *ApJ*, 731, 60
- Grupe D., Mathur S., Komossa S., 2004, *AJ*, 127, 3161
- Guainazzi M., 2002, *MNRAS*, 329, L13
- Guainazzi M., Matt G., Perola G. C., 2005, *A&A*, 444, 119
- Guainazzi M., Rodriguez-Pascual P., Fabian A. C., Iwasawa K.,  
Matt G., 2004, *MNRAS*, 355, 297
- Haardt F., Maraschi L., 1993, *ApJ*, 413, 507
- Hardcastle M. J., Croston J. H., Kraft R. P., 2007, *ApJ*, 669, 893
- Hardcastle M. J., Evans D. A., Croston J. H., 2006, *MNRAS*, 370,  
1893
- Hardcastle M. J., Evans D. A., Croston J. H., 2009, *MNRAS*, 396,  
1929
- Hardcastle M. J. et al., 2012, *MNRAS*, 424, 1774
- Hernández-García L., González-Martín O., Márquez I., Masegosa  
J., 2013, *A&A*, 556, 47
- Hernández-García L., González-Martín O., Masegosa J., Márquez  
I., 2014, *A&A*, 569, A26
- Herrero-Illana R. et al., 2014, *ApJ*, 786, 156
- Ho L. C., 2009, *ApJ*, 699, 626
- Ho L. C. et al., 2001, *ApJ*, 549, L51
- Hodges-Kluck E. J., Reynolds C. S., Cheung C. C., Miller M. C.,  
2010, *ApJ*, 710, 1205
- Holczer T., Behar E., Kaspi S., 2007, *ApJ*, 663, 799
- Hönig S. F., Gandhi P., Asmus D., Mushotzky R. F., Antonucci  
R., Ueda Y., Ichikawa K., 2014, *MNRAS*, 438, 647
- Hönig S. F., Kishimoto M., 2010, *A&A*, 523, 27
- Hönig S. F., Kishimoto M., Antonucci R., Marconi A., Prieto  
M. A., Tristram K., Weigelt G., 2012, *ApJ*, 755, 149
- Hönig S. F., Kishimoto M., Gandhi P., Smette A., Asmus D.,  
Duschl W., Polletta M., Weigelt G., 2010, *A&A*, 515, 23
- Hönig S. F. et al., 2013, *ApJ*, 771, 87
- Hönig S. F., Leipski C., Antonucci R., Haas M., 2011, *ApJ*, 736,  
26
- Horst H., Gandhi P., Smette A., Duschl W. J., 2008, *A&A*, 479,  
389
- Horst H., Smette A., Gandhi P., Duschl W. J., 2006, *A&A*, 457,  
L17
- Hudaverdi M., Kunieda H., Tanaka T., Haba Y., Furuzawa A.,  
Tawara Y., Ercan E. N., 2006, *PASJ*, 58, 931
- Hutchings J. B., Neff S. G., 1989, *AJ*, 97, 1306
- Ichikawa K., Ueda Y., Terashima Y., Oyabu S., Gandhi P., Matsuta  
K., Nakagawa T., 2012, *ApJ*, 754, 45
- Imanishi M., 2003, *ApJ*, 599, 918
- Isobe N., Makishima K., Tashiro M., Hong S., 2005, *ApJ*, 632,  
781
- Iwasawa K. et al., 2011, *A&A*, 529, A106
- Jiménez-Bailón E., Santos-Lleo M., Dahlem M., Ehle M., Mas-  
Hesse J. M., Guainazzi M., Heckman T. M., Weaver K. A., 2005,  
*A&A*, 442, 861
- Jiménez-Bailón E., Santos-Lleo M., Mas-Hesse J. M., Guainazzi  
M., Colina L., Cervio M., González Delgado R. M., 2003, *ApJ*,  
593, 127
- Kaspi S., Netzer H., Chelouche D., George I. M., Nandra K.,  
Turner T. J., 2004, *ApJ*, 611, 68
- Kataoka J. et al., 2008, *ApJ*, 685, 839
- Kataza H., Okamoto Y., Takubo S., Onaka T., Sako S., Nakamura  
K., Miyata T., Yamashita T., 2000, in *SPIE*, Vol. 4008, *Optical  
and IR Telescope Instrumentation and Detectors*, pp. 1144–1152
- Kawamuro T., Ueda Y., Tazaki F., Terashima Y., 2013, *ApJ*, 770,  
157
- Kelly B. C., 2007, *ApJ*, 665, 1489
- Kharb P. et al., 2012, *AJ*, 143, 78
- Kim D.-W., Fabbiano G., 2003, *ApJ*, 586, 826
- King A. L. et al., 2011, *ApJ*, 729, 19
- Kollatschny W., Biermann P., Fricke K. J., Huchtmeier W., Witzel  
A., 1983, *A&A*, 119, 80
- Komossa S., Burwitz V., Hasinger G., Predehl P., Kaastra J. S.,  
Ikebe Y., 2003, *ApJ*, 582, L15
- Koss M. J. et al., 2015, *ArXiv e-prints*, 1505, 3524
- Krabbe A., Böker T., Maiolino R., 2001, *ApJ*, 557, 626
- Kraft R. P., Birkinshaw M., Hardcastle M. J., Evans D. A., Croston  
J. H., Worrall D. M., Murray S. S., 2007, *ApJ*, 659, 1008
- Kraft R. P., Hardcastle M. J., Worrall D. M., Murray S. S., 2005,  
*ApJ*, 622, 149
- Krongold Y. et al., 2010, *ApJ*, 710, 360
- Krongold Y. et al., 2009, *ApJ*, 690, 773
- Krongold Y., Nicastro F., Elvis M., Brickhouse N. S., Mathur S.,  
Zezas A., 2005, *ApJ*, 620, 165
- Lagage P. O. et al., 2004, *The Messenger*, 117, 12
- Laha S., Dewangan G. C., Kembhavi A. K., 2014, *MNRAS*, 437,  
2664

- LaMassa S. M., Heckman T. M., Ptak A., Martins L., Wild V., Sonnentrucker P., Hornschemeier A., 2011, *ApJ*, 729, 52
- Landi R. et al., 2007, *ApJ*, 669, 109
- Lanzuisi G., Piconcelli E., Fiore F., Feruglio C., Vignali C., Salvato M., Gruppioni C., 2009, *A&A*, 498, 67
- Lawson A. J., Turner M. J. L., 1997, *MNRAS*, 288, 920
- Lehmer B. D. et al., 2013, *ApJ*, 771, 134
- Levenson N. A., Heckman T. M., Krolik J. H., Weaver K. A., Życki P. T., 2006, *ApJ*, 648, 111
- Levenson N. A., Radomski J. T., Packham C., Mason R. E., Schaefer J. J., Telesco C. M., 2009, *ApJ*, 703, 390
- Levenson N. A., Weaver K. A., Heckman T. M., Awaki H., Terashima Y., 2004, *ApJ*, 602, 135
- Levenson N. A., Weaver K. A., Heckman T. M., Awaki H., Terashima Y., 2005, *ApJ*, 618, 167
- Li Z. et al., 2011, *ApJ*, 730, 84
- Liu J., 2011, *ApJSS*, 192, 10
- Liu T., Wang J.-X., Yang H., Zhu F.-F., Zhou Y.-Y., 2014, *ApJ*, 783, 106
- Lobban A. P., Reeves J. N., Porquet D., Braito V., Markowitz A., Miller L., Turner T. J., 2010, *MNRAS*, 408, 551
- Lobban A. P., Vaughan S., 2014, *MNRAS*, 439, 1575
- Longinotti A. L., Bianchi S., Ballo L., de La Calle I., Guainazzi M., 2009, *MNRAS*, 394, L1
- Longinotti A. L., Bianchi S., Santos-Lleo M., Rodríguez-Pascual P., Guainazzi M., Cardaci M., Pollock A. M. T., 2007, *A&A*, 470, 73
- Lubiński P., Zdziarski A. A., Walter R., Paltani S., Beckmann V., Soldi S., Ferrigno C., Courvoisier T. J.-L., 2010, *MNRAS*, 408, 1851
- Lutz D., Maiolino R., Spoon H. W. W., Moorwood A. F. M., 2004, *A&A*, 418, 465
- Maccarone T. J., Kundu A., Zepf S. E., 2003, *ApJ*, 586, 814
- Machacek M. E., Jones C., Forman W. R., 2004, *ApJ*, 610, 183
- Maiolino R. et al., 2003, *MNRAS*, 344, L59
- Maiolino R., Salvati M., Bassani L., Dadina M., della Ceca R., Matt G., Risaliti G., Zamorani G., 1998, *A&A*, 338, 781
- Malaguti G. et al., 1998, *A&A*, 331, 519
- Malizia A. et al., 2007, *ApJ*, 668, 81
- Malizia A., Malaguti G., Bassani L., Cappi M., Comastri A., Di Cocco G., Palazzi E., Vignali C., 2002, *A&A*, 394, 801
- Marchese E., Braito V., Della Ceca R., Caccianiga A., Severgnini P., 2012a, *MNRAS*, 421, 1803
- Marchese E., Della Ceca R., Caccianiga A., Severgnini P., Corral A., Fanali R., 2012b, *A&A*, 539, A48
- Marinucci A., Bianchi S., Matt G., Fabian A. C., Iwasawa K., Miniutti G., Piconcelli E., 2011, *A&A*, 526, 36
- Marinucci A., Bianchi S., Nicastro F., Matt G., Goulding A. D., 2012a, *ApJ*, 748, 130
- Marinucci A., Risaliti G., Wang J., Bianchi S., Elvis M., Matt G., Nardini E., Braito V., 2013, *MNRAS*, 429, 2581
- Marinucci A., Risaliti G., Wang J., Nardini E., Elvis M., Fabbiano G., Bianchi S., Matt G., 2012b, *MNRAS*, 423, L6
- Markoff S. et al., 2008, *ApJ*, 681, 905
- Markowitz A., Reeves J. N., George I. M., Braito V., Smith R., Vaughan S., Arévalo P., Tombesi F., 2009, *ApJ*, 691, 922
- Markowitz A. et al., 2007, *ApJ*, 665, 209
- Markowitz A. G., Reeves J. N., 2009, *ApJ*, 705, 496
- Masegosa J., Márquez I., Ramirez A., González-Martín O., 2011, *A&A*, 527, 23
- Mason R. E. et al., 2012, *AJ*, 144, 11
- Massaro F. et al., 2010, *ApJ*, 714, 589
- Massaro F. et al., 2012, *ApJSS*, 203, 31
- Mateos S. et al., 2015, *MNRAS*, 449, 1422
- Matsumoto C., Nava A., Maddox L. A., Leighly K. M., Grupe D., Awaki H., Ueno S., 2004, *ApJ*, 617, 930
- Matsuta K. et al., 2012, *ApJ*, 753, 104
- Matt G., Bianchi S., Guainazzi M., Barcons X., Panessa F., 2012, *A&A*, 540, 111
- Matt G., Bianchi S., Guainazzi M., Brandt W. N., Fabian A. C., Iwasawa K., Perola G. C., 2003, *A&A*, 399, 519
- Matt G., Bianchi S., Marinucci A., Guainazzi M., Iwawasa K., Jimenez Bailon E., 2013, *A&A*, 556, 91
- Mauch T., Murphy T., Buttery H. J., Curran J., Hunstead R. W., Piestrzynski B., Robertson J. G., Sadler E. M., 2003, *MNRAS*, 342, 1117
- Mazzarella J. M. et al., 2012, *AJ*, 144, 125
- McHardy I. M., Papadakis I. E., Uttley P., Page M. J., Mason K. O., 2004, *MNRAS*, 348, 783
- Mingo B., Hardcastle M. J., Croston J. H., Dicken D., Evans D. A., Morganti R., Tadhunter C., 2014, *MNRAS*, 440, 269
- Miniutti G. et al., 2007a, *PASJ*, 59, 315
- Miniutti G., Ponti G., Dadina M., Cappi M., Malaguti G., 2007b, *MNRAS*, 375, 227
- Miniutti G. et al., 2014, *MNRAS*, 437, 1776
- Miniutti G., Saxton R. D., Rodríguez-Pascual P. M., Read A. M., Esquej P., Colless M., Dobbie P., Spolaor M., 2013, *MNRAS*, 433, 1764
- Misaki K., Iwasawa K., Taniguchi Y., Terashima Y., Kunieda H., Watarai H., 1999, *Advances in Space Research*, 23, 1051
- Miyazawa T., Haba Y., Kunieda H., 2009, *PASJ*, 61, 1331
- Modica F. et al., 2012, *AJ*, 143, 16
- Moorwood A. F. M., van der Werf P. P., Kotilainen J. K., Marconi A., Oliva E., 1996, *A&A*, 308, L1
- Mor R., Netzer H., 2012, *MNRAS*, 420, 526
- Moran E. C., Eracleous M., Leighly K. M., Chartas G., Filippenko A. V., Ho L. C., Blanco P. R., 2005, *AJ*, 129, 2108
- Moran E. C., Halpern J. P., Helfand D. J., 1996, *ApJSS*, 106, 341
- Mullaney J. R., Alexander D. M., Goulding A. D., Hickox R. C., 2011, *MNRAS*, 474
- Müller-Sánchez F., González-Martín O., Fernández-Ontiveros J. A., Acosta-Pulido J. A., Prieto M. A., 2010, *ApJ*, 716, 1166
- Nagar N. M., Falcke H., Wilson A. S., 2005, *A&A*, 435, 521
- Nagar N. M., Wilson A. S., Falcke H., 2001, *The ApJL*, 559, L87
- Nandra K., O'Neill P. M., George I. M., Reeves J. N., 2007, *MNRAS*, 382, 194
- Nardini E., Risaliti G., 2011, *MNRAS*, 415, 619
- Nemmen R. S., Storchi-Bergmann T., Yuan F., Eracleous M., Terashima Y., Wilson A. S., 2006, *ApJ*, 643, 652
- Nenkova M., Sirocky M. M., Ivezić v., Elitzur M., 2008, *ApJ*, 685, 147
- Neugebauer G. et al., 1984, *The ApJL*, 278, L1
- Neugebauer G., Matthews K., 1999, *AJ*, 118, 35
- Nicastro F., 2000, *ApJ*, 530, L65
- Nicastro F., Martocchia A., Matt G., 2003, *ApJ*, 589, L13
- Noguchi K., Terashima Y., Awaki H., 2009, *ApJ*, 705, 454
- Noguchi K., Terashima Y., Ishino Y., Hashimoto Y., Koss M., Ueda Y., Awaki H., 2010, *ApJ*, 711, 144
- Ogle P. M., Davis S. W., Antonucci R. R. J., Colbert J. W., Malkan M. A., Page M. J., Sasseen T. P., Tornikoski M., 2005, *ApJ*, 618, 139
- Paggi A., Wang J., Fabbiano G., Elvis M., Karovska M., 2012, *ApJ*, 756, 39
- Panessa F., Bassani L., 2002, *A&A*, 394, 435

- Panessa F., Bassani L., Cappi M., Dadina M., Barcons X., Carrera F. J., Ho L. C., Iwasawa K., 2006, *A&A*, 455, 173
- Panessa F. et al., 2008, *A&A*, 483, 151
- Panessa F. et al., 2009, *MNRAS*, 398, 1951
- Papadakis I. E., Ioannou Z., Brinkmann W., Xilouris E. M., 2008, *A&A*, 490, 995
- Pappa A., Georgantopoulos I., Stewart G. C., Zezas A. L., 2001, *MNRAS*, 326, 995
- Parisi P. et al., 2009, *A&A*, 507, 1345
- Park D., Kelly B. C., Woo J.-H., Treu T., 2012, arXiv:1209.3773
- Pereira-Santaella M. et al., 2011, *A&A*, 535, 93
- Pérez-Beaupuits J. P., Spoon H. W. W., Spaans M., Smith J. D., 2011, *A&A*, 533, 56
- Perlman E. S. et al., 2007, *ApJ*, 663, 808
- Perlman E. S., Wilson A. S., 2005, *ApJ*, 627, 140
- Petrucchi P. O. et al., 2007, *A&A*, 470, 889
- Piconcelli E., Bianchi S., Vignali C., Jiménez-Bailón E., Fiore F., 2011, *A&A*, 534, 126
- Piconcelli E., Jimenez-Bailón E., Guainazzi M., Schartel N., Rodríguez-Pascual P. M., Santos-Lleó M., 2004, *MNRAS*, 351, 161
- Piconcelli E., Jimenez-Bailón E., Guainazzi M., Schartel N., Rodríguez-Pascual P. M., Santos-Lleó M., 2005, *A&A*, 432, 15
- Pier E. A., Krolik J. H., 1992, *ApJ*, 401, 99
- Ponti G., Cappi M., Dadina M., Malaguti G., 2004, *A&A*, 417, 451
- Ponti G. et al., 2009, *MNRAS*, 394, 1487
- Porquet D., Kaastra J. S., Page K. L., O'Brien P. T., Ward M. J., Dubau J., 2004, *A&A*, 413, 913
- Press W. H., Teukolsky S. A., Vetterling W. T., Flannery B. P., 1992, *Numerical recipes in FORTRAN. The art of scientific computing*
- Prieto M. A., Reunanen J., Tristram K. R. W., Neumayer N., Fernandez-Ontiveros J. A., Orienti M., Meisenheimer K., 2010, *MNRAS*, 402, 724
- Ptak A., Heckman T., Levenson N. A., Weaver K., Strickland D., 2003, *ApJ*, 592, 782
- Ptak A. et al., 2015, *ApJ*, 800, 104
- Ptak A., Yaqoob T., Serlemitsos P. J., Kunieda H., Terashima Y., 1996, *ApJ*, 459, 542
- Puccetti S. et al., 2014, *ApJ*, 793, 26
- Ramírez J. M., Komossa S., Burwitz V., Mathur S., 2008, *ApJ*, 681, 965
- Ramos Almeida C. et al., 2011, *ApJ*, 731, 92
- Ramos Almeida C., Pérez García A. M., Acosta-Pulido J. A., Rodríguez Espinosa J. M., 2007, *AJ*, 134, 2006
- Ranalli P., Comastri A., Setti G., 2003, *A&A*, 399, 39
- Reeves J. N. et al., 2007, *PASJ*, 59, 301
- Reeves J. N., Gofford J., Braitto V., Sambruna R., 2010, *ApJ*, 725, 803
- Reynolds C. S., Nowak M. A., Markoff S., Tueller J., Wilms J., Young A. J., 2009, *ApJ*, 691, 1159
- Ricci C., Beckmann V., Audard M., Courvoisier T. J.-L., 2010, *A&A*, 518, 47
- Ricci C., Walter R., Courvoisier T. J.-L., Paltani S., 2011, *A&A*, 532, 102
- Rice W., Lonsdale C. J., Soifer B. T., Neugebauer G., Kopan E. L., Lloyd L. A., de Jong T., Habing H. J., 1988, *ApJSS*, 68, 91
- Rinn A. S., Sambruna R. M., Gliozzi M., 2005, *ApJ*, 621, 167
- Risaliti G. et al., 2009, *The ApJL*, 705, L1
- Risaliti G., Elvis M., Nicastro F., 2002, *ApJ*, 571, 234
- Risaliti G., Gilli R., Maiolino R., Salvati M., 2000, *A&A*, 357, 13
- Risaliti G. et al., 2006, *ApJ*, 637, L17
- Rivers E., Markowitz A., Duro R., Rothschild R., 2012, *ApJ*, 759, 63
- Rivers E., Markowitz A., Rothschild R., 2011a, *ApJSS*, 193, 3
- Rivers E., Markowitz A., Rothschild R., 2011b, *ApJ*, 732, 36
- Rodríguez J., Tomsick J. A., Bodaghee A., 2010, *A&A*, 517, 14
- Rodríguez J., Tomsick J. A., Chaty S., 2008, *A&A*, 482, 731
- Rush B., Malkan M. A., Spinoglio L., 1993, *ApJSS*, 89, 1
- Russell H. R., McNamara B. R., Edge A. C., Hogan M. T., Main R. A., Vantyghem A. N., 2013, *MNRAS*, 432, 530
- Sambruna R. M., Eracleous M., Mushotzky R. F., 1999, *ApJ*, 526, 60
- Sambruna R. M. et al., 2009, *ApJ*, 700, 1473
- Sambruna R. M., Tombesi F., Reeves J. N., Braitto V., Ballo L., Gliozzi M., Reynolds C. S., 2011, *ApJ*, 734, 105
- Sanders D. B., Mazzarella J. M., Kim D.-C., Surace J. A., Soifer B. T., 2003, *AJ*, 126, 1607
- Sanders D. B., Mirabel I. F., 1996, *ARA&A*, 34, 749
- Satyapal S., Dudik R. P., O'Halloran B., Gliozzi M., 2005, *ApJ*, 633, 86
- Satyapal S., Sambruna R. M., Dudik R. P., 2004, *A&A*, 414, 825
- Saxton R. D., Read A. M., Esquej P., Freyberg M. J., Altieri B., Bermejo D., 2008, *A&A*, 480, 611
- Sazonov S., Churazov E., Revnivtsev M., Vikhlinin A., Sunyaev R., 2005, *A&A*, 444, L37
- Sazonov S. et al., 2012, *ApJ*, 757, 181
- Severgnini P., Caccianiga A., Della Ceca R., 2012, *A&A*, 542, 46
- Shelton D. L., Hardcastle M. J., Croston J. H., 2011, *MNRAS*, 418, 811
- Shi Y. et al., 2005, *ApJ*, 629, 88
- Shi Y., Rieke G. H., Smith P., Rigby J., Hines D., Donley J., Schmidt G., Diamond-Stanic A. M., 2010, *ApJ*, 714, 115
- Shinozaki K., Miyaji T., Ishisaki Y., Ueda Y., Ogasaka Y., 2006, *AJ*, 131, 2843
- Shirai H. et al., 2008, *PASJ*, 60, 263
- Shu X. W., Liu T., Wang J. X., 2010, *ApJ*, 722, 96
- Shu X. W., Wang J. X., Jiang P., Fan L. L., Wang T. G., 2007, *ApJ*, 657, 167
- Shu X.-W., Wang J.-X., Liu T., Zheng W., 2012, *Research in A&A*, 12, 1247
- Shu X. W., Yaqoob T., Murphy K. D., Braitto V., Wang J. X., Zheng W., 2010, *ApJ*, 713, 1256
- Shu X. W., Yaqoob T., Wang J. X., 2010, *ApJSS*, 187, 581
- Singh V., Risaliti G., Braitto V., Shastri P., 2012, *MNRAS*, 419, 2089
- Smith D. A., Wilson A. S., 2001, *ApJ*, 557, 180
- Soldi S. et al., 2008, *A&A*, 486, 411
- Spoon H. W. W., Koornneef J., Moorwood A. F. M., Lutz D., Tielens A. G. G. M., 2000, *A&A*, 357, 898
- Stalevski M., Fritz J., Baes M., Nakos T., Popović L., 2012, *MNRAS*, 420, 2756
- Stern D., 2015, arXiv:1506.00162 [astro-ph], arXiv: 1506.00162
- Strickland D. K., 2007, *MNRAS*, 376, 523
- Tazaki F., Ueda Y., Terashima Y., Mushotzky R. F., 2011, *ApJ*, 738, 70
- Telesco C. M., Pina R. K., Hanna K. T., Julian J. A., Hon D. B., Kisko T. M., 1998, in *SPIE, Vol. 3354, Infrared Astronomical Instrumentation*, pp. 534–544
- Teng S. H., Veilleux S., 2010, *ApJ*, 725, 1848
- Teng S. H. et al., 2009, *ApJ*, 691, 261
- Teng S. H., Veilleux S., Wilson A. S., Young A. J., Sanders D. B., Nagar N. M., 2008, *ApJ*, 674, 133

- Teng S. H., Wilson A. S., Veilleux S., Young A. J., Sanders D. B., Nagar N. M., 2005, *ApJ*, 633, 664
- Terashima Y., Iyomoto N., Ho L. C., Ptak A. F., 2002, *ApJSS*, 139, 1
- Terashima Y., Wilson A. S., 2003, *ApJ*, 583, 145
- Tingay S. J., Jauncey D. L., King E. A., Tzioumis A. K., Lovell J. E. J., Edwards P. G., 2003, *PASJ*, 55, 351
- Tombesi F., Cappi M., Reeves J. N., Palumbo G. G. C., Yaqoob T., Braito V., Dadina M., 2010, *A&A*, 521, 57
- Torresi E., Grandi P., Guainazzi M., Palumbo G. G. C., Ponti G., Bianchi S., 2009, *A&A*, 498, 61
- Trippe M. L., Reynolds C. S., Koss M., Mushotzky R. F., Winter L. M., 2011, *ApJ*, 736, 81
- Tristram K. R. W., Burtscher L., Jaffe W., Meisenheimer K., Hönig S. F., Kishimoto M., Schartmann M., Weigelt G., 2014, *A&A*, 563, 82
- Turner T. J., George I. M., Nandra K., Mushotzky R. F., 1997, *ApJSS*, 113, 23
- Turner T. J., Miller L., Kraemer S. B., Reeves J. N., Pounds K. A., 2009, *ApJ*, 698, 99
- Tzanavaris P., Georgantopoulos I., 2007, *A&A*, 468, 129
- Ueda Y. et al., 2007, *ApJ*, 664, L79
- Ueda Y., Ishisaki Y., Takahashi T., Makishima K., Ohashi T., 2001, *ApJSS*, 133, 1
- Ueda Y., Ishisaki Y., Takahashi T., Makishima K., Ohashi T., 2005, *ApJSS*, 161, 185
- Vasudevan R. V., Brandt W. N., Mushotzky R. F., Winter L. M., Baumgartner W. H., Shimizu T. T., Schneider D. P., Nousek J., 2013a, *ApJ*, 763, 111
- Vasudevan R. V., Fabian A. C., 2009, *MNRAS*, 392, 1124
- Vasudevan R. V., Fabian A. C., Mushotzky R. F., Meléndez M., Winter L. M., Trippe M. L., 2013b, *MNRAS*, 431, 3127
- Vasudevan R. V., Mushotzky R. F., Winter L. M., Fabian A. C., 2009, *MNRAS*, 399, 1553
- Vaughan S., Uttley P., Pounds K. A., Nandra K., Strohmayer T. E., 2011, *MNRAS*, 413, 2489
- Véron-Cetty M.-P., Véron P., 2010, *A&A*, 518, 10
- Vignali C., Comastri A., Stirpe G. M., Cappi M., Palumbo G. G. C., Matsuoka M., Malaguti G., Bassani L., 1998, *A&A*, 333, 411
- Wang J., Risaliti G., Fabbiano G., Elvis M., Zezas A., Karovska M., 2010, *ApJ*, 714, 1497
- Wang J.-B., Gao Y., 2010, *Research in A&A*, 10, 309
- Warwick R. S., Saxton R. D., Read A. M., 2012, *A&A*, 548, 99
- Weaver K. A., Heckman T. M., Strickland D. K., Dahlem M., 2002, *ApJ*, 576, L19
- White R. L., Becker R. H., 1992, *ApJSS*, 79, 331
- Winter L. M., Mushotzky R., 2010, *ApJ*, 719, 737
- Winter L. M., Mushotzky R. F., Reynolds C. S., Tueller J., 2009a, *ApJ*, 690, 1322
- Winter L. M., Mushotzky R. F., Terashima Y., Ueda Y., 2009b, *ApJ*, 701, 1644
- Winter L. M., Mushotzky R. F., Tueller J., Markwardt C., 2008, *ApJ*, 674, 686
- Winter L. M., Veilleux S., McKernan B., Kallman T. R., 2012, *ApJ*, 745, 107
- Wright A. E., Griffith M. R., Hunt A. J., Troup E., Burke B. F., Ekers R. D., 1996, *ApJSS*, 103, 145
- Wright E. L. et al., 2010, *AJ*, 140, 1868
- Yamaoka H., Kato T., Filippenko A. V., van Dyk S. D., Yamamoto M., Balam D., Hornoch K., Plsek M., 1998, *International Astronomical Union Circular*, 6859, 1
- Yang H., Wang J., Liu T., 2015, *ApJ*, 799, 91
- Yang Y., Wilson A. S., Matt G., Terashima Y., Greenhill L. J., 2009, *ApJ*, 691, 131
- Yankulova I. M., Golev V. K., Jockers K., 2007, *A&A*, 469, 891
- Yaqoob T., 2012, *MNRAS*, 423, 3360
- Yaqoob T., George I. M., Kallman T. R., Padmanabhan U., Weaver K. A., Turner T. J., 2003, *ApJ*, 596, 85
- Yaqoob T. et al., 2007, *PASJ*, 59, 283
- Younes G., Porquet D., Sabra B., Grosso N., Reeves J. N., Allen M. G., 2010, *A&A*, 517, 33
- Younes G., Porquet D., Sabra B., Reeves J. N., 2011, *A&A*, 530, 149
- Young A. J., Wilson A. S., Terashima Y., Arnaud K. A., Smith D. A., 2002, *ApJ*, 564, 176
- Yuan F., Cui W., 2005, *ApJ*, 629, 408
- Yuan T.-T., Kewley L. J., Sanders D. B., 2010, *ApJ*, 709, 884
- Zezas A., Ward M. J., Murray S. S., 2003, *The ApJL*, 594, L31
- Zhang J. S., Henkel C., Kadler M., Greenhill L. J., Nagar N., Wilson A. S., Braatz J. A., 2006, *A&A*, 450, 933
- Zhang W. M., Soria R., Zhang S. N., Swartz D. A., Liu J. F., 2009, *ApJ*, 699, 281

Table 2: Reliable sample.

Object	$D$ [Mpc]	Opt. class	$\log L^{\text{nuc}}$ (12 $\mu\text{m}$ ) [erg/s]	$\log L^{\text{nuc}}$ (18 $\mu\text{m}$ ) [erg/s]	X-ray epochs	$\log L^{\text{obs}}$ (2-10 keV) [erg/s]	$\log N_{\text{H}}$ [ $\text{cm}^{-2}$ ]	$\log L^{\text{int}}$ (2-10 keV) [erg/s]	$\log L^{\text{obs}}$ (14-195 keV) [erg/s]	radio- loud?	2-10 keV Ref.
(1)	(2)	(3)	(4)	(5)	(6)	(7)	(8)	(9)	(10)	(11)	(12)
IH 0419-577	499.0	1.5	44.67 $\pm$ 0.08		5+	44.54 $\pm$ 0.16	21.6 $\pm$ 0.45	44.89 $\pm$ 0.56	44.87 $\pm$ 0.05	0	1, 2, 3
1RXS J112716.6+	512.0	1.8	44.52 $\pm$ 0.05		2	44.12 $\pm$ 0.30	$\leq$ 19.9	44.07 $\pm$ 0.30	44.69 $\pm$ 0.13	?	4, 3
2MASX J03565655	351.0	1.9	44.07 $\pm$ 0.15		2	43.92 $\pm$ 0.30	22.7 $\pm$ 0.45	43.78 $\pm$ 0.30	44.46 $\pm$ 0.10	?	5, 3
2MASX J09180027	781.0	2	44.51 $\pm$ 0.08		1	44.03 $\pm$ 0.30	23.1 $\pm$ 0.45	44.11 $\pm$ 0.30	$\leq$ 44.99	?	6, 3
3C 29	202.0	L	$\leq$ 42.57		1	41.15 $\pm$ 0.30	$\leq$ 22.3	41.32 $\pm$ 0.30	$\leq$ 43.82	1	7
3C 33	273.0	2	43.89 $\pm$ 0.18		2	43.38 $\pm$ 0.30	23.6 $\pm$ 0.07	43.91 $\pm$ 0.30	44.39 $\pm$ 0.07	1	8, 9, 10
3C 78	127.0	1	$\leq$ 42.76		3	42.30 $\pm$ 0.35	$\leq$ 21.0	42.37 $\pm$ 0.28	$\leq$ 43.41	1	11, 12, 13
3C 93	1967.0	1	$\leq$ 44.51		1	44.62 $\pm$ 0.30	$\leq$ 21.3	44.58 $\pm$ 0.30	$\leq$ 45.79	1	14
3C 98	137.0	2	43.17 $\pm$ 0.11		3	42.60 $\pm$ 0.22	23.0 $\pm$ 0.07	42.79 $\pm$ 0.25	43.18 $\pm$ 0.20	1	15, 16, 17
3C 105	421.0	2	43.72 $\pm$ 0.15		3	43.49 $\pm$ 0.22	23.3 $\pm$ 0.37	43.93 $\pm$ 0.35	44.77 $\pm$ 0.08	1	18, 3, 6
3C 120	150.0	1.5	44.26 $\pm$ 0.01		5+	44.08 $\pm$ 0.04	$\leq$ 21.2	44.11 $\pm$ 0.08	44.40 $\pm$ 0.02	1	19, 20, 21, 3
3C 227	414.0	1.5	44.22 $\pm$ 0.04		3	43.71 $\pm$ 0.30	22.1 $\pm$ 0.45	43.52 $\pm$ 0.38	44.69 $\pm$ 0.09	1	22, 23, 24
3C 273	792.0	1	45.73 $\pm$ 0.07		5+	45.89 $\pm$ 0.06	$\leq$ 19.7	45.87 $\pm$ 0.12	46.52 $\pm$ 0.00	1	25, 19, 26
3C 285	378.0	2	$\leq$ 43.42		1	43.07 $\pm$ 0.30	23.5 $\pm$ 0.45	43.36 $\pm$ 0.30	$\leq$ 44.36	1	27, 17
3C 293	211.0	L	$\leq$ 42.84		1	42.50 $\pm$ 0.30	23.0 $\pm$ 0.45	42.78 $\pm$ 0.30	$\leq$ 43.85	1	18, 28
3C 317	160.0	2/L	$\leq$ 42.31		2	41.65 $\pm$ 0.30	$\leq$ 21.0	41.65 $\pm$ 0.30	$\leq$ 43.61	1	29, 13
3C 353	138.0	2/L	42.68 $\pm$ 0.11		2	42.31 $\pm$ 0.30	22.8 $\pm$ 0.45	42.46 $\pm$ 0.30	$\leq$ 43.48	1	30, 31
3C 382	267.0	1	44.33 $\pm$ 0.04		5+	44.55 $\pm$ 0.15	20.8 $\pm$ 0.45	44.54 $\pm$ 0.17	44.87 $\pm$ 0.02	1	32, 33, 3
3C 390.3	259.0	1.5	44.46 $\pm$ 0.15		4	44.41 $\pm$ 0.19	20.7 $\pm$ 0.45	44.39 $\pm$ 0.21	44.91 $\pm$ 0.02	1	10, 34, 3
3C 403	271.0	2	44.32 $\pm$ 0.06		2	42.97 $\pm$ 0.30	23.7 $\pm$ 0.09	43.73 $\pm$ 0.42	44.48 $\pm$ 0.08	1	3, 35, 36
3C 445	254.0	1.5	44.54 $\pm$ 0.04		3	43.69 $\pm$ 0.07	23.1 $\pm$ 0.12	44.11 $\pm$ 0.16	44.51 $\pm$ 0.05	1	37, 38, 39
3C 452	378.0	2	44.25 $\pm$ 0.08		3	43.52 $\pm$ 0.05	23.6 $\pm$ 0.17	43.96 $\pm$ 0.06	44.75 $\pm$ 0.06	1	10, 40, 6, 3
4C +73.08	271.0	2	43.69 $\pm$ 0.13		1	42.89 $\pm$ 0.30	24.0 $\pm$ 0.45	43.79 $\pm$ 0.30	44.13 $\pm$ 0.11	1	41
Ark 120	149.0	1	44.22 $\pm$ 0.02		3	43.91 $\pm$ 0.04	$\leq$ 20.0	43.90 $\pm$ 0.06	44.27 $\pm$ 0.03	0	42, 43, 3
Cen A	3.8	2	41.82 $\pm$ 0.04	41.81 $\pm$ 0.05	4	41.61 $\pm$ 0.06	23.1 $\pm$ 0.45	41.95 $\pm$ 0.10	42.38 $\pm$ 0.00	1	44, 45
Circinus	4.2	2	42.65 $\pm$ 0.05	42.68 $\pm$ 0.04	3	40.44 $\pm$ 0.30	24.7 $\pm$ 0.17	42.26 $\pm$ 0.28	41.76 $\pm$ 0.01	0	46, 47, 48
Cygnus A	257.0	2	44.05 $\pm$ 0.09		3	44.01 $\pm$ 0.30	23.3 $\pm$ 0.08	44.34 $\pm$ 0.04	45.04 $\pm$ 0.01	1	10, 49, 17
ESO 5-4	22.4	2	41.64 $\pm$ 0.05	41.82 $\pm$ 0.13	1	40.82 $\pm$ 0.30	24.0 $\pm$ 0.45	41.77 $\pm$ 0.30	42.30 $\pm$ 0.06	?	50
ESO 33-2	82.3	2	43.55 $\pm$ 0.13		3	42.83 $\pm$ 0.16	22.1 $\pm$ 0.45	42.89 $\pm$ 0.15	43.24 $\pm$ 0.08	0	51, 52, 14
ESO 103-35	59.5	2	43.71 $\pm$ 0.19		3	43.04 $\pm$ 0.06	23.3 $\pm$ 0.03	43.22 $\pm$ 0.35	43.68 $\pm$ 0.02	0	53, 16, 3
ESO 121-28	187.0	2	43.19 $\pm$ 0.04		1	43.09 $\pm$ 0.30	23.2 $\pm$ 0.45	43.41 $\pm$ 0.30	44.07 $\pm$ 0.06	?	3
ESO 141-55	169.0	1.2	44.11 $\pm$ 0.09		3	43.85 $\pm$ 0.10	$\leq$ 20.8	43.85 $\pm$ 0.10	44.27 $\pm$ 0.04	0	54, 55, 14
ESO 198-24	208.0	1	43.64 $\pm$ 0.11		3	43.67 $\pm$ 0.13	$\leq$ 20.3	43.67 $\pm$ 0.11	44.18 $\pm$ 0.06	?	56, 57, 58
ESO 209-12	189.0	1.5	44.23 $\pm$ 0.06		2	43.62 $\pm$ 0.30	19.0 $\pm$ 0.45	43.62 $\pm$ 0.30	43.96 $\pm$ 0.08	?	53, 59
ESO 263-13	158.0	2	43.62 $\pm$ 0.03		3	42.87 $\pm$ 0.16	23.5 $\pm$ 0.09	43.42 $\pm$ 0.03	44.02 $\pm$ 0.06	?	53, 60, 61
ESO 297-18	111.0	2	43.04 $\pm$ 0.07		1	42.69 $\pm$ 0.30	23.6 $\pm$ 0.45	43.60 $\pm$ 0.30	44.01 $\pm$ 0.03	?	50
ESO 323-32	76.4	1.9	42.97 $\pm$ 0.05		2	41.40 $\pm$ 0.30	24.1 $\pm$ 0.45	42.50 $\pm$ 0.30	43.03 $\pm$ 0.19	?	53, 60, 25
ESO 323-77	71.8	1.2	43.74 $\pm$ 0.09		5+	42.57 $\pm$ 0.21	23.6 $\pm$ 0.45	42.76 $\pm$ 0.12	43.31 $\pm$ 0.10	?	62
ESO 362-18	56.5	1.5	43.17 $\pm$ 0.05		3	42.62 $\pm$ 0.49	22.0 $\pm$ 1.80	42.73 $\pm$ 0.31	43.27 $\pm$ 0.04	?	19, 43, 63
ESO 416-2	272.0	1.9	43.73 $\pm$ 0.06		2	43.59 $\pm$ 0.30	$\leq$ 21.6	43.58 $\pm$ 0.30	44.31 $\pm$ 0.09	1	64, 14
ESO 506-27	119.0	2	43.88 $\pm$ 0.04		3	42.69 $\pm$ 0.18	23.9 $\pm$ 0.45	43.37 $\pm$ 0.44	44.20 $\pm$ 0.03	?	65, 16, 61
ESO 511-30	105.0	1	43.24 $\pm$ 0.04		2	43.31 $\pm$ 0.30	$\leq$ 21.0	43.28 $\pm$ 0.30	43.72 $\pm$ 0.06	?	66, 43, 3
ESO 548-81	63.5	1	43.02 $\pm$ 0.14		3	42.85 $\pm$ 0.09	$\leq$ 21.0	42.87 $\pm$ 0.12	43.33 $\pm$ 0.04	0	63, 43, 63
Fairall 9	215.0	1.2	44.59 $\pm$ 0.04		5	44.03 $\pm$ 0.09	$\leq$ 20.5	43.99 $\pm$ 0.11	44.44 $\pm$ 0.03	?	37, 67, 43, 3
Fairall 49	90.1	2	43.96 $\pm$ 0.20		4	43.33 $\pm$ 0.11	22.2 $\pm$ 0.45	43.34 $\pm$ 0.11	43.14 $\pm$ 0.12	?	68, 57
Fairall 51	64.1	1.5	43.68 $\pm$ 0.04	43.76 $\pm$ 0.01	3	42.98 $\pm$ 0.01	22.4 $\pm$ 0.12	43.05 $\pm$ 0.03	43.30 $\pm$ 0.05	0	69, 70, 14
Fornax A	19.0	L	41.27 $\pm$ 0.12		2	39.96 $\pm$ 0.30	21.5 $\pm$ 0.45	39.73 $\pm$ 0.41	$\leq$ 41.76	1	19, 11, 71
H 0557-385	156.0	1.2	44.49 $\pm$ 0.04		5+	43.47 $\pm$ 0.57	22.8 $\pm$ 0.78	43.86 $\pm$ 0.23	43.93 $\pm$ 0.05	?	72, 73, 74, 3
H1143-182	156.0	1.5	43.69 $\pm$ 0.04		2	43.77 $\pm$ 0.30	$\leq$ 20.5	43.75 $\pm$ 0.30	44.19 $\pm$ 0.04	0	75, 3
Hydra A	260.0	L	$\leq$ 42.98		3	42.09 $\pm$ 0.03	22.6 $\pm$ 0.12	42.25 $\pm$ 0.08	$\leq$ 44.03	1	76, 11, 77
IC 1459	30.3	L	$\leq$ 41.67		1	40.83 $\pm$ 0.30	21.8 $\pm$ 0.45	40.71 $\pm$ 0.30	$\leq$ 42.17	1	76, 78, 79
IC 4329A	76.5	1.2	44.31 $\pm$ 0.04	44.41 $\pm$ 0.03	5+	43.87 $\pm$ 0.05	21.5 $\pm$ 0.42	43.85 $\pm$ 0.09	44.31 $\pm$ 0.01	0	80, 19, 81, 3
IC 5063	49.1	2	43.77 $\pm$ 0.03	43.95 $\pm$ 0.01	4	42.61 $\pm$ 0.26	23.4 $\pm$ 0.06	42.86 $\pm$ 0.10	43.32 $\pm$ 0.03	1	82, 83, 36
IRAS 09149-6206	269.0	1	45.00 $\pm$ 0.06		2	44.05 $\pm$ 0.30	21.7 $\pm$ 0.45	44.05 $\pm$ 0.30	44.44 $\pm$ 0.05	?	84, 85
IRAS 13349+2438	522.0	1n	45.59 $\pm$ 0.05		3	43.96 $\pm$ 0.11	21.6 $\pm$ 0.45	43.95 $\pm$ 0.09	$\leq$ 44.64	?	86, 14, 19
I Zw 1	269.0	1n	44.96 $\pm$ 0.07		3	43.68 $\pm$ 0.16	$\leq$ 21.0	43.68 $\pm$ 0.17	$\leq$ 44.06	0	14, 19, 87
LEDA 13946	166.0	2	$\leq$ 42.98		2	42.74 $\pm$ 0.36	23.2 $\pm$ 0.45	43.20 $\pm$ 0.30	43.84 $\pm$ 0.09	?	88, 3
LEDA 170194	173.0	2	43.58 $\pm$ 0.08		2	43.70 $\pm$ 0.30	22.6 $\pm$ 0.45	43.80 $\pm$ 0.30	44.17 $\pm$ 0.06	?	89, 3
LEDA 178130	160.0	2	43.60 $\pm$ 0.13		3	43.57 $\pm$ 0.06	23.1 $\pm$ 0.33	43.81 $\pm$ 0.36	44.27 $\pm$ 0.03	0	88, 5, 3
LEDA 549777	284.1	2	43.89 $\pm$ 0.06		2	43.23 $\pm$ 0.30	23.1 $\pm$ 0.05	43.29 $\pm$ 0.30	44.25 $\pm$ 0.12	?	90, 91, 3
M51a	8.1	2	40.70 $\pm$ 0.19		5+	39.18 $\pm$ 0.31	$\geq$ 24.3	40.59 $\pm$ 0.60	$\leq$ 41.02	0	92, 83, 19
M81	3.6	L	40.73 $\pm$ 0.05	40.70 $\pm$ 0.05	5+	40.23 $\pm$ 0.06	20.7 $\pm$ 0.45	40.23 $\pm$ 0.05	40.39 $\pm$ 0.10	1	92, 93, 94, 3
M87	16.7	L	41.25 $\pm$ 0.06	$\leq$ 41.39	3	40.63 $\pm$ 0.10	21.5 $\pm$ 0.45	40.66 $\pm$ 0.16	$\leq$ 41.65	1	76, 78, 29
MCG-1-5-47	73.4	2	42.94 $\pm$ 0.15		3	42.33 $\pm$ 0.13	23.2 $\pm$ 0.16	42.81 $\pm$ 0.13	43.17 $\pm$ 0.09	?	95, 61, 96
MCG-1-13-25	71.2	1.2	42.57 $\pm$ 0.13		2	42.76 $\pm$ 0.30	$\leq$ 19.6	42.76 $\pm$ 0.30	43.28 $\pm$ 0.08	?	64, 64
MCG-1-24-12	93.8	2	43.46 $\pm$ 0.04		1	42.98 $\pm$ 0.30	22.9 $\pm$ 0.45	43.36 $\pm$ 0.30	43.63 $\pm$ 0.05	?	97, 3
MCG-2-8-14	72.5	2	42.84 $\pm$ 0.07		2	42.52 $\pm$ 0.30	23.1 $\pm$ 0.45	42.90 $\pm$ 0.30	43.21 $\pm$ 0.07	?	95, 98
MCG-2-8-39	133.0	2	44.09 $\pm$ 0.07	44.12 $\pm$ 0.05	1	42.24 $\pm$ 0.30	23.6 $\pm$ 0.45	42.82 $\pm$ 0.30	$\leq$ 43.45	?	19, 99
MCG-3-34-64	79.3	1.8/2	44.00 $\pm$ 0.05		1	42.24 $\pm$ 0.30	23.6 $\pm$ 0.01	43.33 $\pm$ 0.48	43.36 $\pm$ 0.07	?	100, 19
MCG-5-23-16	42.8	1.9	43.59 $\pm$ 0.04	43.73 $\pm$ 0.02	3	43.28 $\pm$ 0.30	22.1 $\pm$ 0.07				



Table 2: continued.

Object	$D$ [Mpc]	Opt. class	$\log L^{\text{nuc}}$ (12 $\mu\text{m}$ ) [erg/s]	$\log L^{\text{nuc}}$ (18 $\mu\text{m}$ ) [erg/s]	X-ray epochs	$\log L^{\text{obs}}$ (2–10 keV) [erg/s]	$\log N_{\text{H}}$ [ $\text{cm}^{-2}$ ]	$\log L^{\text{int}}$ (2–10 keV) [erg/s]	$\log L^{\text{obs}}$ (14–195 keV) [erg/s]	radio- loud?	2–10 keV Ref.
(1)	(2)	(3)	(4)	(5)	(6)	(7)	(8)	(9)	(10)	(11)	(12)
Mrk 926	210.0	1.5	44.16 ± 0.10		4	44.32 ± 0.11	≤ 20.4	44.30 ± 0.13	44.78 ± 0.02	0	119, 120, 14, 3
Mrk 937	129.0	1	≤ 42.86		1	42.62 ± 0.30	20.5 ± 0.45	42.62 ± 0.30	≤ 43.43	?	55, 121
Mrk 1014	807.0	1.5	45.29 ± 0.15		2	43.96 ± 0.30	≤ 21.0	44.09 ± 0.30	≤ 45.02	?	87, 122, 123
Mrk 1018	191.0	1	43.76 ± 0.04		3	43.63 ± 0.08	≤ 20.0	43.62 ± 0.06	44.16 ± 0.07	0	124, 43, 3
Mrk 1239	95.4	1n	44.21 ± 0.07	44.21 ± 0.02	1	42.13 ± 0.30	23.5 ± 0.45	43.32 ± 0.30	≤ 43.16	?	125, 126
NGC 235A	96.2	2	43.29 ± 0.16		1	42.53 ± 0.30	23.5 ± 0.45	43.18 ± 0.30	43.72 ± 0.04	?	3
NGC 454E	52.3	2	43.05 ± 0.09		3	41.80 ± 0.23	23.4 ± 0.20	42.29 ± 0.23	42.76 ± 0.11	?	127, 5, 3
NGC 526A	82.8	1.9	43.68 ± 0.05		4	43.30 ± 0.06	22.1 ± 0.06	43.28 ± 0.10	43.72 ± 0.03	0	37, 19, 57
NGC 612	132.0	2	≤ 43.24		4	42.46 ± 0.16	23.9 ± 0.18	43.13 ± 0.42	44.06 ± 0.04	1	128, 129, 90, 3
NGC 788	57.2	2	43.12 ± 0.05		2	42.29 ± 0.30	23.7 ± 0.17	42.96 ± 0.30	43.50 ± 0.02	?	130, 89, 3
NGC 985	195.0	1.5	44.31 ± 0.06		3	43.63 ± 0.23	21.2 ± 0.45	43.63 ± 0.23	44.16 ± 0.05	0	131, 132, 43
NGC 1052	19.4	L	42.19 ± 0.06	42.41 ± 0.04	5+	41.07 ± 0.11	23.0 ± 0.45	41.52 ± 0.08	42.12 ± 0.07	1	76, 133
NGC 1068	14.4	1.8/2	43.80 ± 0.13	43.90 ± 0.01	5+	41.01 ± 0.08	≥ 25.0	43.64 ± 0.30	41.94 ± 0.06	0	53, 134, 110
NGC 1097	17.0	L	41.17 ± 0.06	41.41 ± 0.09	1	40.78 ± 0.30	20.4 ± 0.45	40.78 ± 0.30	≤ 41.67	1	135
NGC 1144	128.0	2	43.09 ± 0.20		3	42.76 ± 0.11	23.9 ± 0.10	43.52 ± 0.10	44.24 ± 0.02	?	65, 16, 65
NGC 1194	58.2	1.9	43.45 ± 0.04		1	41.49 ± 0.30	23.9 ± 0.45	42.47 ± 0.30	43.17 ± 0.06	0	19, 136
NGC 1275	76.8	1.5/L	44.21 ± 0.04		3	43.03 ± 0.42	22.6 ± 0.45	43.02 ± 0.43	43.71 ± 0.02	1	92, 13, 137
NGC 1365	17.9	1.8	42.54 ± 0.04		5+	41.39 ± 0.43	23.2 ± 0.45	42.12 ± 0.20	42.39 ± 0.02	?	138, 19, 139, 3
NGC 1553	16.4	L	≤ 41.34		1	40.09 ± 0.30	21.5 ± 0.45	39.90 ± 0.30	≤ 41.63	?	140, 141
NGC 1566	14.3	1.5	41.56 ± 0.18	41.76 ± 0.08	3	40.96 ± 0.17	21.7 ± 0.45	40.97 ± 0.17	41.72 ± 0.08	?	142, 143, 14
NGC 2110	35.9	2	43.09 ± 0.06	43.14 ± 0.02	4	42.68 ± 0.10	22.5 ± 0.06	42.67 ± 0.10	43.69 ± 0.01	?	80, 144, 144, 3
NGC 2992	39.7	1.5/2	42.95 ± 0.13	43.23 ± 0.02	5	42.71 ± 0.45	22.0 ± 0.30	42.53 ± 0.59	42.71 ± 0.08	?	19, 145, 146, 3
NGC 3081	40.9	2	42.87 ± 0.07	42.90 ± 0.03	3	41.73 ± 0.31	23.9 ± 0.11	42.53 ± 0.29	43.22 ± 0.03	0	53, 128, 147
NGC 3147	30.1	2	41.72 ± 0.12		3	41.37 ± 0.24	≤ 20.7	41.37 ± 0.22	≤ 42.16	1	92, 148, 149
NGC 3169	18.7	L	40.91 ± 0.20		1	41.02 ± 0.30	23.0 ± 0.45	41.33 ± 0.30	≤ 41.75	1	150
NGC 3227	22.1	1.5	42.47 ± 0.10	42.89 ± 0.03	4	42.10 ± 0.26	22.2 ± 0.71	42.14 ± 0.21	42.81 ± 0.02	0	151, 19, 57, 3
NGC 3393	61.6	2	42.88 ± 0.08		6	41.20 ± 0.20	24.3 ± 0.08	43.27 ± 0.24	43.07 ± 0.10	?	53, 152, 153
NGC 3718	17.0	L	41.29 ± 0.09		3	40.84 ± 0.18	22.1 ± 0.05	40.87 ± 0.17	41.62 ± 0.13	1	154, 154, 154
NGC 3783	48.4	1.5	43.69 ± 0.03	43.83 ± 0.03	5+	43.25 ± 0.07	≤ 20.9	43.24 ± 0.07	43.71 ± 0.01	0	75, 155, 156, 3
NGC 3998	14.1	L	41.63 ± 0.04	41.78 ± 0.04	3	41.33 ± 0.06	21.3 ± 0.99	41.33 ± 0.06	41.55 ± 0.11	1	76, 154, 157
NGC 4051	12.2	1n	42.33 ± 0.04		5+	41.55 ± 0.17	≤ 20.1	41.55 ± 0.17	41.85 ± 0.03	0	158, 159, 160, 3
NGC 4074	107.0	2	43.35 ± 0.11		1	42.58 ± 0.30	23.3 ± 0.45	42.96 ± 0.30	43.61 ± 0.07	0	16
NGC 4111	15.0	L	40.40 ± 0.10		2	39.46 ± 0.26	23.6 ±	39.90 ± 0.47	≤ 41.56	?	76, 140, 157
NGC 4138	13.8	1.9	41.09 ± 0.06		2	40.71 ± 0.54	22.9 ± 0.45	41.24 ± 0.30	41.83 ± 0.06	?	161, 162
NGC 4151	13.3	1.5	42.84 ± 0.07		5+	42.32 ± 0.23	22.7 ± 0.19	42.52 ± 0.29	43.06 ± 0.00	0	155, 163, 164
NGC 4235	41.2	1.2	42.26 ± 0.07	42.28 ± 0.05	1	41.76 ± 0.30	21.5 ± 0.45	41.77 ± 0.30	42.82 ± 0.06	?	165, 124, 4
NGC 4258	7.6	2	41.26 ± 0.05		5+	40.80 ± 0.18	22.6 ± 0.45	40.99 ± 0.15	41.18 ± 0.07	?	166, 167
NGC 4261	31.7	L	41.60 ± 0.09	41.63 ± 0.02	4	40.72 ± 0.04	23.0 ± 0.25	41.02 ± 0.04	≤ 42.21	1	76, 168, 133
NGC 4278	16.1	L	40.29 ± 0.10		5+	40.01 ± 0.43	20.5 ± 0.15	40.06 ± 0.45	≤ 41.62	1	150, 169, 133
NGC 4374	17.1	2/L	≤ 40.84		1	39.56 ± 0.30	21.2 ± 0.45	39.55 ± 0.55	≤ 41.67	1	76, 10, 140
NGC 4388	19.2	2	42.32 ± 0.07	42.75 ± 0.01	5	41.80 ± 0.24	23.5 ± 0.07	42.26 ± 0.23	43.09 ± 0.01	?	53, 16, 170, 3
NGC 4395	4.3	1.8	39.71 ± 0.08		3	39.92 ± 0.21	22.4 ± 0.32	39.84 ± 0.11	40.75 ± 0.06	0	161, 171, 172
NGC 4507	57.5	2	43.78 ± 0.04		5+	42.64 ± 0.25	23.7 ± 0.19	43.21 ± 0.17	43.87 ± 0.01	?	173, 16, 174, 3
NGC 4579	16.8	L	41.80 ± 0.03	41.74 ± 0.05	4	41.12 ± 0.06	20.6 ± 0.27	41.16 ± 0.03	41.48 ± 0.22	1	157, 161, 175
NGC 4593	45.6	1	43.15 ± 0.07	43.18 ± 0.01	5+	42.86 ± 0.31	20.4 ± 0.45	42.86 ± 0.31	43.34 ± 0.02	0	37, 155, 176, 3
NGC 4594	9.1	L	40.04 ± 0.12		4	39.94 ± 0.12	21.4 ± 0.45	39.94 ± 0.12	≤ 41.12	1	76, 93, 177
NGC 4941	21.2	2	42.00 ± 0.05	42.30 ± 0.03	4	40.92 ± 0.41	23.8 ± 0.17	41.53 ± 0.18	42.04 ± 0.11	?	147, 143, 157
NGC 4992	119.0	1/2/L/N	43.51 ± 0.09		3	42.60 ± 0.01	23.9 ± 0.12	43.39 ± 0.18	43.96 ± 0.04	?	60, 4, 178
NGC 5033	18.1	1.2	41.21 ± 0.06		3	40.99 ± 0.28	≤ 20.4	41.00 ± 0.28	41.34 ± 0.10	?	161, 165, 93
NGC 5135	66.0	2	43.23 ± 0.08		2	41.20 ± 0.30	24.4 ± 0.45	43.21 ± 0.60	≤ 42.84	1	179, 180
NGC 5252	109.0	1.9	43.39 ± 0.04		3	43.07 ± 0.13	22.6 ± 0.19	43.11 ± 0.12	44.22 ± 0.02	?	181, 4, 3
NGC 5273	15.3	1.5	41.15 ± 0.09		2	40.98 ± 0.47	22.3 ± 0.45	40.97 ± 0.46	41.59 ± 0.15	0	161, 182
NGC 5506	31.6	2	43.41 ± 0.03	43.52 ± 0.04	5+	43.06 ± 0.10	22.4 ± 0.10	43.12 ± 0.11	43.46 ± 0.01	0	83, 83, 155
NGC 5548	80.7	1.5	43.39 ± 0.21		5+	43.38 ± 0.25	≤ 20.2	43.38 ± 0.25	43.79 ± 0.02	0	183, 184, 155
NGC 5728	45.4	1.9/2	42.48 ± 0.06	42.70 ± 0.11	2	41.56 ± 0.30	24.1 ± 0.45	42.82 ± 0.60	43.34 ± 0.03	?	60, 185
NGC 5995	117.0	1.9	44.13 ± 0.06		3	43.46 ± 0.19	22.0 ± 0.45	43.45 ± 0.15	43.85 ± 0.06	?	186, 24, 14
NGC 6251	112.0	1/2/L	42.75 ± 0.10		5+	42.77 ± 0.06	20.7 ± 0.45	42.77 ± 0.06	≤ 43.30	1	187, 188, 189
NGC 6300	14.3	2	42.53 ± 0.11		3	41.61 ± 0.39	23.3 ± 0.01	42.09 ± 0.44	42.39 ± 0.02	?	190, 191, 137
NGC 6814	20.1	1.5	42.06 ± 0.10	42.08 ± 0.04	5+	41.82 ± 0.31	≤ 20.5	41.82 ± 0.31	42.57 ± 0.03	0	53, 43, 14, 3
NGC 6860	65.8	1.5	43.42 ± 0.05	43.42 ± 0.02	5+	42.94 ± 0.20	22.0 ± 0.46	42.94 ± 0.19	43.44 ± 0.04	0	192, 192, 14, 3
NGC 7172	34.8	2	42.83 ± 0.04		4	42.70 ± 0.15	22.9 ± 0.11	42.79 ± 0.16	43.39 ± 0.01	0	101, 16, 19, 3
NGC 7213	23.0	1.5/L	42.51 ± 0.04	42.62 ± 0.06	4	42.20 ± 0.07	20.3 ± 0.45	42.19 ± 0.06	42.43 ± 0.05	1	193, 194, 195, 3
NGC 7314	18.3	1.9/2	41.79 ± 0.08	42.06 ± 0.03	4	41.95 ± 0.35	22.0 ± 0.09	41.98 ± 0.27	42.32 ± 0.04	?	114, 196, 197, 3
NGC 7469	67.9	1/1.5	43.83 ± 0.04	44.03 ± 0.05	5+	43.19 ± 0.07	≤ 20.7 0.45	43.19 ± 0.07	43.57 ± 0.03	?	14, 75, 155
NGC 7626	45.4	L:	≤ 42.06		1	40.97 ± 0.30	≤ 22.0	40.97 ± 0.30	≤ 42.52	1	198
NGC 7674	126.0	2	44.26 ± 0.05	44.43 ± 0.01	3	42.07 ± 0.09	≥ 24.4	44.02 ± 0.55	≤ 43.41	0	199, 200, 19
PG 0026+129	691.0	1.2	44.66 ± 0.04		3	44.57 ± 0.16	21.2 ±	44.57 ± 0.16	44.85 ± 0.15	0	201, 202, 14
PG 0052+251	759.0	1.2	44.68 ± 0.12		3	44.69 ± 0.02	≤ 20.7	44.69 ± 0.02	44.98 ± 0.14	0	203, 201, 14
PG 0844+349	302.0	1	44.03 ± 0.15		5+	43.52 ± 0.33	≤ 20.4	43.52 ± 0.33	43.63 ± 0.33	?	87, 204, 205
PG 2130+099	288.0	1.5	44.67 ± 0.05		3	43.74 ± 0.23	≤ 20.7	43.74 ± 0.23	≤ 44.12	0	206, 207, 202
Pictor A	161.0	1.5/L	43.76 ± 0.04	43.83 ± 0.06	4	43.49 ± 0.05	20.6 ± 0.45	43.48 ± 0.04	44.08 ± 0.04	1	208, 43, 22, 3
PKS 1417-19	586.0	1.5	44.31 ± 0.18		2	44.27 ± 0.30	≤ 21.0	44.27 ± 0.30	≤ 44.74	1	52, 14
PKS 1814-63	302.0	2	43.88 ± 0.08		2	43.92 ± 0.45	22.3 ± 0.45	43.90 ± 0.43	44.00 ± 0.22	1	101, 209
Z 41-20	170.0	2	43.40 ± 0.04		3	43.28 ± 0.07	23.1 ± 0.14	43.52 ± 0.17	43.86 ± 0.09	0	63, 25, 3

– Notes: (1), (2), (3), (4), and (5) short object name, distance, optical class, nuclear 12 and 18  $\mu\text{m}$  luminosities from Asmus et al. (2014); (6) number of 2–10 keV epochs used; (7) average observed 2–10 keV luminosity; (8) average X-ray column density; (9) average absorption-

corrected 2–10 keV luminosity; (10) average observed 14–195 keV luminosity from *Swift*/BAT by combining the data of the 54 and 70 month source catalogues (Cusumano et al. 2010; Baumgartner et al. 2013); (11) radio-loudness flag (see Sect. 4.6 for explanation); (12) references for the 2–10 keV luminosities and column densities: 1: Fabian et al. (2005); 2: Turner et al. (2009); 3: Winter et al. (2009a); 4: Vasudevan et al. (2013a); 5: Vasudevan et al. (2013b); 6: Fioretti et al. (2013); 7: Massaro et al. (2012); 8: Kraft et al. (2007); 9: Torresi et al. (2009); 10: Evans et al. (2006); 11: Rinn, Sambruna & Gliozzi (2005); 12: this work (CSC); 13: Balmaverde, Capetti & Grandi (2006); 14: this work (XSPEC); 15: Isobe et al. (2005); 16: Noguchi, Terashima & Awaki (2009); 17: Hodges-Kluck et al. (2010); 18: Massaro et al. (2010); 19: Brightman & Nandra (2011a); 20: Cowperthwaite & Reynolds (2012); 21: Ogle et al. (2005); 22: Hardcastle, Croston & Kraft (2007); 23: Cusumano et al. (2010); 24: Warwick, Saxton & Read (2012); 25: Fukazawa et al. (2011); 26: Chernyakova et al. (2007); 27: Hardcastle, Evans & Croston (2006); 28: Hardcastle, Evans & Croston (2009); 29: Donato, Sambruna & Gliozzi (2004); 30: Kataoka et al. (2008); 31: Goodger et al. (2008); 32: Gliozzi et al. (2007); 33: Sambruna et al. (2011); 34: Sambruna et al. (2009); 35: Kraft et al. (2005); 36: Tazaki et al. (2011); 37: Horst et al. (2008); 38: Braitto et al. (2011); 39: Reeves et al. (2010); 40: Shelton, Hardcastle & Croston (2011); 41: Evans et al. (2008c); 42: Vasudevan & Fabian (2009); 43: Winter et al. (2012); 44: Evans et al. (2004); 45: Markowitz et al. (2007); 46: Smith & Wilson (2001); 47: Arévalo et al. (2014); 48: Yang et al. (2009); 49: Young et al. (2002); 50: Ueda et al. (2007); 51: Vignali et al. (1998); 52: Saxton et al. (2008); 53: Gandhi et al. (2009); 54: Gondoin, Orr & Lumb (2003); 55: Ueda et al. (2001); 56: Porquet et al. (2004); 57: Shu, Yaqoob & Wang (2010); 58: Laha, Dewangan & Kembhavi (2014); 59: Panessa et al. (2008); 60: Comastri et al. (2010); 61: Landi et al. (2007); 62: Miniutti et al. (2014); 63: Winter et al. (2008); 64: Gallo et al. (2006); 65: Winter et al. (2009b); 66: Tombesi et al. (2010); 67: Emmanoulopoulos et al. (2011); 68: Lobban & Vaughan (2014); 69: Ricci et al. (2010); 70: Beckmann et al. (2009); 71: Kim & Fabbiano (2003); 72: Ashton et al. (2006); 73: Longinotti et al. (2009); 74: Coffey et al. (2014); 75: Nandra et al. (2007); 76: González-Martín et al. (2009b); 77: Russell et al. (2013); 78: Satyapal, Sambruna & Dudik (2004); 79: Fabbiano et al. (2003); 80: Dadina (2007); 81: Brenneman et al. (2014); 82: Risaliti, Elvis & Nicastro (2002); 83: LaMassa et al. (2011); 84: Vasudevan et al. (2009); 85: Malizia et al. (2007); 86: Holczer, Behar & Kaspi (2007); 87: Piconcelli et al. (2005); 88: Eguchi et al. (2009); 89: de Rosa et al. (2008); 90: Parisi et al. (2009); 91: Balokovic et al. (in prep.); 92: Panessa et al. (2006); 93: Ho et al. (2001); 94: Markoff et al. (2008); 95: Baumgartner et al. (2013); 96: Trippe et al. (2011); 97: Malizia et al. (2002); 98: Rodriguez, Tomsick & Bodaghee (2010); 99: Noguchi et al. (2010); 100: Miniutti et al. (2007b); 101: Awaki et al. (2006); 102: Reeves et al. (2007); 103: Balestra, Bianchi & Matt (2004); 104: Miniutti et al. (2007a); 105: Ponti et al. (2004); 106: Gofford et al. (2011); 107: Ramírez et al. (2008); 108: Kaspi et al. (2004); 109: Awaki et al. (2008); 110: Levenson et al. (2006); 111: Bianchi et al. (2005); 112: Piconcelli et al. (2004); 113: Teng & Veilleux (2010); 114: Shinozaki et al. (2006); 115: Ponti et al. (2009); 116: Longinotti et al. (2007); 117: Rivers et al. (2012); 118: Petrucci et al. (2007); 119: Bianchi et al. (2004); 120: Rivers, Markowitz & Rothschild (2011b); 121: Turner et al. (1997); 122: Teng et al. (2005); 123: Boller et al. (2002); 124: Bianchi et al. (2009a); 125: Grupe, Mathur & Komossa (2004); 126: Miyazawa, Haba & Kunieda (2009); 127: Marchese et al. (2012a); 128: Eguchi et al. (2011); 129: Sambruna, Eracleous & Mushotzky (1999); 130: Marinucci et al. (2012a); 131: Krongold et al. (2009); 132: Krongold et al. (2005); 133: Hernández-García et al. (2013); 134: Bauer et al. (2014); 135: Nemmen et al. (2006); 136: Greenhill, Tilak & Madejski (2008); 137: Beckmann et al. (2006); 138: Risaliti et al. (2009); 139: Brenneman et al. (2013); 140: Flohic et al. (2006); 141: Blanton, Sarazin & Irwin (2001); 142: Levenson et al. (2009); 143: Kawamuro et al. (2013); 144: Evans et al. (2007); 145: Yaqoob et al. (2007); 146: Shu et al. (2010); 147: Maiolino et al. (1998); 148: Matt et al. (2012); 149: Bianchi et al. (2008a); 150: Terashima & Wilson (2003); 151: Markowitz et al. (2009); 152: Fabbiano et al. (2011); 153: Koss et al. (2015); 154: Younes et al. (2011); 155: Rivers, Markowitz & Rothschild (2011a); 156: Brenneman et al. (2011); 157: Terashima et al. (2002); 158: King et al. (2011); 159: McHardy et al. (2004); 160: Vaughan et al. (2011); 161: Cappi et al. (2006); 162: Zhang et al. (2009); 163: Wang et al. (2010); 164: Lubiński et al. (2010); 165: Papadakis et al. (2008); 166: Fruscione et al. (2005); 167: Reynolds et al. (2009); 168: Satyapal et al. (2005); 169: Younes et al. (2010); 170: Shirai et al. (2008); 171: González-Martín et al. (2006); 172: Moran et al. (2005); 173: Braitto et al. (2013); 174: Marinucci et al. (2013); 175: Eracleous et al. (2002); 176: Markowitz & Reeves (2009); 177: Li et al. (2011); 178: Sazonov et al. (2005); 179: Levenson et al. (2004); 180: Singh et al. (2012); 181: Dadina et al. (2010); 182: Capetti & Balmaverde (2005); 183: Andrade-Velázquez et al. (2010); 184: Krongold et al. (2010); 185: Zhang et al. (2006); 186: Panessa & Bassani (2002); 187: Evans et al. (2005); 188: Gliozzi et al. (2004); 189: Gliozzi, Papadakis & Sambruna (2008); 190: Matsumoto et al. (2004); 191: Guainazzi (2002); 192: Winter & Mushotzky (2010); 193: Lobban et al. (2010); 194: Bianchi et al. (2003); 195: Bianchi et al. (2008b); 196: Ebrero et al. (2011); 197: Yaqoob et al. (2003); 198: Ho (2009); 199: Malaguti et al. (1998); 200: Gandhi et al. (in prep.); 201: Ueda et al. (2005); 202: Lawson & Turner (1997); 203: D’Ammando et al. (2008); 204: Brinkmann et al. (2003); 205: Gallo et al. (2011); 206: Gallo (2006); 207: Cardaci et al. (2009); 208: Shi et al. (2005); 209: Mingo et al. (2014);

## APPENDIX A: XRT SPECTRAL FITS

For 19 sources, we analysed *Swift*/XRT data using the online data products and tools from the UK Swift Science Data Centre (Evans et al. 2009). These were used to build average calibrated 0.3–10 keV spectra of all XRT observations for each object, which were then fitted with an absorbed power-law in the 1 to 10 keV range using the XSPEC package v12.8.2 (Arnaud 1996). The fitting results are summarised in the following Table A1. Galactic absorption was taken into account, and in case the fitted intrinsic absorption was smaller, we used the former as upper limit for  $N_{\text{H}}$ . Two objects with strong absorption/low S/N are individually discussed in Appendix B4.

## APPENDIX B: THE REMAINING SOURCES FROM THE AGN MIR ATLAS

In the following sections, the remaining objects from the MIR AGN atlas that were not included in the reliable sample are discussed in three groups:

- **X-ray unreliable AGN:** objects that are known securely to host AGN without significant star formation contamination, but do not have reliable  $L^{\text{int}}(2\text{--}10\text{ keV})$  estimates, see Section B1;
- **AGN/starburst composites:** objects that have certain AGN but possibly suffer from significant star formation contamination, see Section B2;
- **uncertain AGN:** objects with controversial or insufficient evidence for the presence of an AGN (similar to Asmus et al. 2014), see Section B3.

In addition, particularly interesting objects are further discussed in App. B4 individually.

### B1 The X-ray unreliable and Compton-thick AGN

Using Equations 6 and 2, we can now predict  $N_{\text{H}}$  and  $L^{\text{int}}(2\text{--}10\text{ keV})$  for the 45 AGN from the AGN MIR atlas that we had to discard because of uncertain  $L^{\text{int}}(2\text{--}10\text{ keV})$  and/or  $N_{\text{H}}$  values (see Table B1). Of these, 22 are previously classified as CT or CT candidates and are shown in Fig. 23. Only two of these objects are incompatible with being CT within the uncertainties using our  $N_{\text{H}}$  diagnostic (NGC 1667 and NGC 5363). Both objects have more than 1 dex lower predicted  $L^{\text{int}}(2\text{--}10\text{ keV})$  than stated in the literature assuming they are CT (see Fig. B1). NGC 7743 has not been detected in the MIR but the resulting upper limit on the predicted  $L^{\text{int}}(2\text{--}10\text{ keV})$  is also significantly lower than the value stated in the literature assuming CT obscuration.

Of the 23 objects previously not classified as Compton-thick, seven are compatible with being CT within the uncertainties (ESO 253-3, IC 4518W, IRAS 01003-2238, IRAS 05189-2524, NGC 34, NGC 3982, and NGC 4736). All these objects have indeed predicted  $L^{\text{int}}(2\text{--}10\text{ keV})$  values significantly higher than the values found in the literature for non-CT scenarios. Finally, our diagnostics predict  $L^{\text{int}}(2\text{--}10\text{ keV})$  and  $N_{\text{H}}$  in good agreement with the literature values for the remaining sources, where the latter is available (apart from one exception: NGC 5005). Therefore, it is not surprising that all the other X-ray unreliable objects are lying close to the MIR–X-ray correlation as shown in Fig. B1.

Note that 13 of the 22 objects listed as bona-fide CT in Gandhi et al. (2014) are included in the atlas as well (NGC 7582 is excluded because it turned out to be a changing look AGN; see, e.g., Asmus et al. 2014). All of them apart from NGC 4945 (see next section)

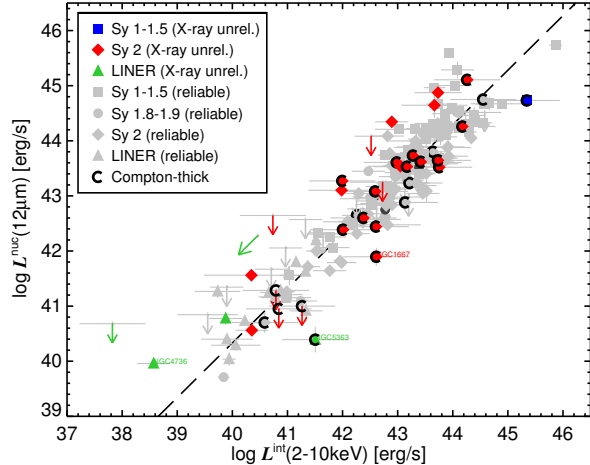


**Figure B1.** Distribution of the X-ray unreliable AGN in the observed  $12\ \mu\text{m}$  to intrinsic  $2\text{--}10\text{ keV}$  plane. Symbols are as in Fig. 3. All reliable AGN are in light gray and the long dashed line is their `linmix_err` fit. X-ray unreliable sources are plotted with colours.

follow the general MIR–X-ray correlation, which indicates that this will also be the case for the whole local CT population.

### B2 Contamination of AGN/starburst composites

The AGN MIR atlas contains 18 AGN/starburst composite objects with verified AGN (Asmus et al. 2014). They were excluded from the reliable sample because the intense nuclear and/or circum-nuclear star formation possibly contaminates or even dominates their high angular resolution MIR photometry. Indeed, often the nuclear MIR emission is extended on subarcsecond scales, making it difficult to separate AGN and starburst contributions. Even worse, the star formation can significantly contribute also to the X-ray emission in the case of low-luminosity AGN, and/or obscure the AGN even if it is very powerful. In fact, at least five of the 18 composite sources are CT obscured (NGC 2623, NGC 3690W, NGC 4945, NGC 6240S, and NGC 7130). Therefore, the composite objects are not well suited for determinations of the MIR–X-ray correlation. However, we can use the MIR–X-ray correlation to possibly obtain a better understanding of the dominant power source in these objects. For this purpose, their X-ray properties are collected from the literature as for the other objects of the atlas (as described in Sect. 2). The corresponding properties and references are given in Table B2. For three sources (ESO 420-13, Mrk 897 and NGC 7496), unfortunately, no X-ray observation has been published, while the nucleus of NGC 5953 remained undetected in hard X-rays during *Chandra* snapshot observations. Therefore, we can predict only their  $L^{\text{int}}(2\text{--}10\text{ keV})$  under the assumption that their subarcsecond MIR luminosities are AGN dominated (listed in Table B2). Furthermore, three AGN/starburst composites either suffer CT obscuration or have complex X-ray properties that do not allow for any intrinsic X-ray luminosity estimates (III Zw 35, NGC 7592W and UGC 5101). For these, the available observed X-ray luminosities predict CT obscuration using Equation 6 and the above assumption of AGN MIR dominance.

The remaining 11 AGN/starburst composites are plotted in the  $12\ \mu\text{m}$ – $2\text{--}10\text{ keV}$  plane next to the reliable AGN in Fig. B2 using their unresolved nuclear MIR emission. For comparison, the pure

**Table A1.** XRT spectral fits

Object	$\log N_{\text{H,Gal}}$ [ $\text{cm}^{-2}$ ]	$\log N_{\text{H,abs}}$ [ $\text{cm}^{-2}$ ]	$\Gamma$	$\chi^2$	DOF	$\log F^{\text{obs}}(2\text{-}10\text{ keV})$ [ $\text{erg/s/cm}^2$ ]	$\log L^{\text{int}}(2\text{-}10\text{ keV})$ [ $\text{erg/s}$ ]
(1)	(2)	(3)	(4)	(5)	(6)	(7)	(8)
3C 93	21.29	$\leq 21.29$	1.51	898.4	432	-12.05	44.58
ESO 33-2	21.10	22.27	1.62	561.7	503	-11.09	42.88
ESO 141-55	20.81	$\leq 20.81$	2.1	302.2	405	-10.76	43.77
ESO 253-3	20.61	23.48	2.56	154.8	160	-12.26	42.93
ESO 416-2	20.25	21.91	2.11	192.6	182	-11.38	43.64
Fairall 51	20.98	22.45	1.42	352.9	425	-10.73	43.02
IRAS 13349+2438	20.02	20.85	1.49	1042.2	607	-11.54	43.92
I Zw 1	20.77	$\leq 20.77$	2.12	551.1	517	-11.39	43.55
Mrk 915	20.82	21.65	1.26	727.8	554	-10.95	43.16
Mrk 926	20.52	$\leq 20.52$	1.68	619.3	572	-10.32	44.41
NGC 1566	19.95	21.01	1.67	806.1	623	-11.48	40.91
NGC 5995	21.20	22.14	1.64	882.9	677	-10.81	43.43
NGC 6814	21.17	$\leq 21.17$	1.56	968.2	701	-11.18	41.50
NGC 6860	20.56	21.77	1.31	837.1	631	-10.80	42.91
NGC 7469	20.73	$\leq 20.73$	1.74	1121.7	834	-10.63	43.12
PG 0026+129	20.80	21.30	2.08	693.0	490	-11.32	44.42
PG 0052+251	20.71	$\leq 20.71$	1.8	868.5	440	-11.14	44.70
PKS 1417-19	21.00	$\leq 21.00$	1.86	602.5	541	-11.30	44.31
PKS 2158-380	20.14	$\geq 22.00$	...	...	...	-12.66	...

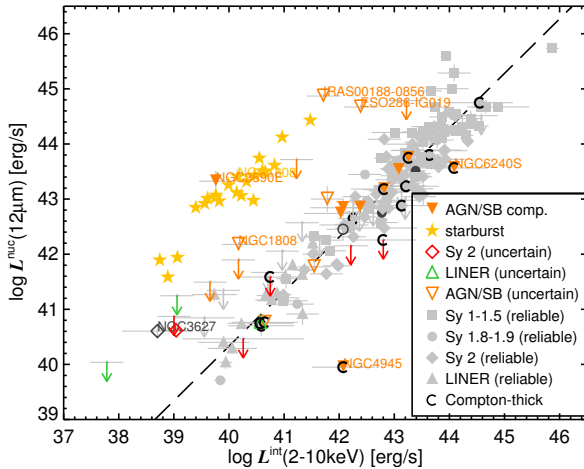


**Figure B2.** Distribution of AGN/SB composite objects and uncertain AGN in the observed  $12\ \mu\text{m}$  to intrinsic  $2\text{-}10\text{ keV}$  plane. Symbols are as in Fig. 3. All reliable AGN are in light gray and the long dashed line is their  $\text{linmix\_err}$  fit. AGN/starburst composites are shown as orange triangles and the starburst galaxies from Ranalli, Comastri & Setti (2003) as yellow stars. Objects with uncertain AGN are shown as open symbols.

starburst galaxies from Ranalli, Comastri & Setti (2003) are plotted as well. For those the total MIR and X-ray luminosities are used in the absence of nuclear compact emission (see also Asmus et al. 2011). These sources follow their own MIR–X-ray correlation with a similar slope but an MIR–X-ray ratio of  $\sim 3$  dex, which is  $\sim 2.7$  dex higher than that of the reliable AGN. Therefore, we expect composite sources to also exhibit high MIR–X-ray ratios, lying close to the pure starbursts in the MIR–X-ray plane. However, most of the verified composite sources, 9 out of 11, are surprisingly close to the correlation of the reliable AGN, indicating that their nuclear MIR emission is not dominated by star formation.

One exception is NGC 3690E with a very high MIR–X-ray ratio similar to a pure starburst. However, this source is a good candidate for Compton-thick obscuration (see Appendix B4), which would mean an order of magnitude higher intrinsic X-ray luminosity and thus lower MIR–X-ray ratio. Unfortunately, the available data in the MIR and X-ray are not sufficient to distinguish whether the nuclear MIR emission is star formation contaminated or the nucleus is Compton-thick obscured in X-rays. At least, deep silicate absorption features in the lower resolution *Spitzer* MIR spectrum of NGC 3690E indicates indeed heavy absorption but also strong PAH emission (typical for star formation).

The other extreme outlier is NGC 4945, which exhibits instead an extremely low MIR–X-ray ratio ( $R_X^M = -2.54$ ), i.e. being either MIR under-luminous or X-ray over-luminous by almost three orders of magnitude (see also discussion in Gandhi et al. 2015). As discussed in Asmus et al. (2014), this very nearby object;  $D \sim 4$  Mpc) shows very extended nuclear MIR emission dominated by star formation with a relatively faint core. This makes the estimation of the nuclear AGN-related MIR emission very difficult. However, this complication is not sufficient to alone explain the low MIR–X-ray ratio.

For example, the object distance could also contribute. Artificially moving NGC 4945 to the median distance of the AGN MIR atlas (72 Mpc), all emission within  $\sim 7''$  would be unresolved. In that case the  $F^{\text{nuc}}(12\ \mu\text{m})$  would be between  $\sim 400$  to 2000 mJy (the fluxes in the *Spitzer*/IRS and *ISO*/PHT-S spectra; Spoon et al. 2000; Pérez-Beaupuits et al. 2011), and thus 20–100 times higher (1.3–2 dex). Thus, a possible intrinsic resolution effect can also not explain the MIR–X-ray ratio by itself. This is, in fact, unlikely because firstly it would mean that the MIR emission of AGN in general is dominated by unresolved circumnuclear star formation contradicting, e.g., Asmus et al. (2011) and Asmus et al. (2014), and secondly because other comparably close and powerful objects like Circinus show even higher than average MIR–X-ray ratios ( $R_X^M = 0.39$ ).

On the other hand, NGC 4945 is Compton-thick obscured in X-rays exhibiting a highly variable and complex spectrum (e.g.,

Table B1. Properties of X-ray unreliable AGN.

Object	$D$ [Mpc]	Opt. class	$\log L^{\text{nuc}}$ (12 $\mu\text{m}$ ) [erg/s]	$\log L^{\text{obs}}$ (2–10 keV) [erg/s]	Lit. $\log N_{\text{H}}$ [ $\text{cm}^{-2}$ ]	Lit. $\log L^{\text{int}}$ (2–10 keV) [erg/s]	Pred. $\log N_{\text{H}}$ [ $\text{cm}^{-2}$ ]	Pred. $\log L^{\text{int}}$ (2–10 keV) [erg/s]	$\log L^{\text{obs}}$ (14–195 keV) [erg/s]	2–10 keV Ref.
(1)	(2)	(3)	(4)	(5)	(6)	(7)	(8)	(9)	(10)	(11)
3C 135	620.0	2	$\leq 44.08$	$42.47 \pm 0.30$	$22.3 \pm 0.45$	$42.52 \pm 0.30$		$\leq 44.08$	$\leq 44.79$	1
3C 305	192.0	2	$\leq 42.64$	$40.30 \pm 0.30$	$21.2 \pm 0.34$	$40.74 \pm 0.60$		$\leq 42.71$	$\leq 43.77$	2, 3
3C 321	460.0	2	$44.65 \pm 0.24$	$42.34 \pm 0.30$	$24.0 \pm 0.45$	$43.67 \pm 0.60$	$24.5 \pm 0.5$	$44.24 \pm 0.44$	$\leq 44.53$	4, 5
3C 327	505.0	1	$44.73 \pm 0.11$	$42.28 \pm 0.30$	$\geq 24.3$	$45.34 \pm 0.60$	$24.6 \pm 0.5$	$44.33 \pm 0.39$	$\leq 44.61$	6, 7
3C 424	613.0	2	$\leq 43.25$	$42.43 \pm 0.30$	$22.7 \pm 0.45$	$42.73 \pm 0.60$		$\leq 43.29$	$\leq 44.78$	8
3C 449	72.4	L	$\leq 42.28$	$\leq 40.48$		$\leq 40.46$		$\leq 42.37$	$\leq 42.92$	4, 9, 10
ESO 138–1	41.8	2	$43.61 \pm 0.02$	$41.62 \pm 0.30$	$\geq 24.3$	$42.98 \pm 0.60$	$24.3 \pm 0.4$	$43.26 \pm 0.37$	$42.61 \pm 0.10$	11, 12
ESO 253–3	196.0	2	$44.34 \pm 0.08$	$42.40 \pm 0.30$	$23.5 \pm 0.45$	$42.93 \pm 0.30$	$24.2 \pm 0.4$	$43.96 \pm 0.38$	$\leq 43.79$	7
ESO 428–14	28.2	2	$42.44 \pm 0.06$	$40.56 \pm 0.30$	$\geq 24.3$	$42.61 \pm 0.60$	$24.2 \pm 0.4$	$42.15 \pm 0.37$	$\leq 42.11$	13
IC 3639	53.6	2	$43.52 \pm 0.04$	$40.84 \pm 0.56$	$\geq 25.0$	$43.75 \pm 0.60$	$24.7 \pm 0.6$	$43.17 \pm 0.37$	$\leq 42.66$	11, 14, 15
IC 4518W	76.1	2	$43.54 \pm 0.06$	$42.73 \pm 0.79$	$23.3 \pm 0.11$	$43.05 \pm 0.59$	$23.5 \pm 0.9$	$43.19 \pm 0.38$	$43.28 \pm 0.07$	16, 17, 18
IRAS 01003–2238	565.0	2	$45.31 \pm 0.04$	$41.58 \pm 0.43$			$25.5 \pm 0.5$	$44.88 \pm 0.37$	$\leq 44.71$	19, 20
IRAS 04103–2838	567.0	2	$45.11 \pm 0.07$	$42.01 \pm 0.30$	$\geq 24.3$	$44.26 \pm 0.60$	$25.0 \pm 0.4$	$44.68 \pm 0.38$	$\leq 44.71$	21, 20
IRAS 05189–2524	196.0	2	$44.87 \pm 0.15$	$42.71 \pm 0.76$	$22.8 \pm 0.02$	$43.73 \pm 0.43$	$24.4 \pm 0.8$	$44.46 \pm 0.40$	$43.76 \pm 0.15$	22, 23, 24
Mrk 266SW	128.0	2	$42.46 \pm 0.08$	$41.44 \pm 0.30$	$\geq 24.0$		$23.6 \pm 0.4$	$42.17 \pm 0.38$	$\leq 43.42$	25
Mrk 573	73.1	2	$43.53 \pm 0.07$	$41.13 \pm 0.30$	$\geq 24.2$	$43.17 \pm 0.60$	$24.6 \pm 0.4$	$43.18 \pm 0.38$	$\leq 42.93$	15, 26, 27
NGC 34	83.5	2	$43.10 \pm 0.05$	$41.36 \pm 0.30$	$23.7 \pm 0.45$	$41.98 \pm 0.60$	$24.1 \pm 0.4$	$42.78 \pm 0.37$	$\leq 43.05$	22, 15, 26
NGC 424	49.5	2	$43.73 \pm 0.11$	$41.51 \pm 0.23$	$25.0 \pm 0.45$	$43.28 \pm 0.60$	$24.4 \pm 0.4$	$43.38 \pm 0.39$	$42.78 \pm 0.08$	28, 29, 30
NGC 676	19.5	2	$\leq 41.28$	$38.87 \pm 0.30$	$\geq 24.3$	$40.79 \pm 0.60$		$\leq 41.42$	$\leq 41.79$	31, 32, 33
NGC 1386	16.5	2	$42.39 \pm 0.08$	$39.92 \pm 0.09$	$\geq 24.3$	$42.01 \pm 0.60$	$24.6 \pm 0.3$	$42.10 \pm 0.38$	$\leq 41.64$	13, 22, 34
NGC 1667	67.8	2	$41.90 \pm 0.16$	$40.69 \pm 0.30$	$\geq 24.3$	$42.61 \pm 0.60$	$23.7 \pm 0.5$	$41.63 \pm 0.40$	$\leq 42.87$	22, 31, 35
NGC 3166	25.3	L	$41.05 \pm 0.11$					$40.83 \pm 0.39$	$\leq 42.01$	
NGC 3281	52.8	2	$43.62 \pm 0.04$	$41.93 \pm 0.30$	$24.3 \pm 0.45$	$43.42 \pm 0.60$	$24.1 \pm 0.4$	$43.27 \pm 0.37$	$43.46 \pm 0.02$	11
NGC 3312	48.4	L	$41.74 \pm 0.07$	$\leq 41.16$			$\leq 23.6$	$41.48 \pm 0.38$	$\leq 42.57$	36
NGC 3368	10.6	L	$\leq 40.70$	$39.31 \pm 0.60$				$\leq 40.86$	$\leq 41.26$	37, 38, 39
NGC 3623	12.8	L	$\leq 40.92$	$38.75 \pm 0.30$				$\leq 41.07$	$\leq 41.42$	40, 37
NGC 3982	21.4	2	$41.56 \pm 0.06$	$39.65 \pm 0.31$	$23.3 \pm 0.45$	$40.35 \pm 0.87$	$24.2 \pm 0.5$	$41.31 \pm 0.38$	$\leq 41.87$	31, 41, 22
NGC 4501	17.9	2	$40.56 \pm 0.06$	$39.59 \pm 0.30$	$23.3 \pm 0.45$	$40.35 \pm 0.30$	$23.6 \pm 0.4$	$40.36 \pm 0.37$	$\leq 41.71$	32, 42, 41
NGC 4636	15.6	L	$\leq 40.68$	$37.82 \pm 0.60$	$\leq 21.0$	$37.82 \pm 0.60$		$\leq 40.85$	$\leq 41.59$	40, 43, 44
NGC 4698	24.4	2	$\leq 40.95$	$39.06 \pm 0.60$	$\geq 24.3$	$40.84 \pm 0.60$		$\leq 41.10$	$\leq 41.98$	40, 32, 45
NGC 4736	4.9	L	$39.96 \pm 0.08$	$38.57 \pm 0.30$	$20.6 \pm 0.45$	$38.57 \pm 0.30$	$23.9 \pm 0.4$	$39.79 \pm 0.38$	$\leq 40.58$	40
NGC 5005	16.9	L	$40.78 \pm 0.12$	$39.83 \pm 0.30$	$21.0 \pm 0.45$	$39.88 \pm 0.30$	$23.6 \pm 0.5$	$40.57 \pm 0.39$	$\leq 41.66$	40, 45, 46
NGC 5347	38.1	2	$43.08 \pm 0.04$	$40.58 \pm 0.30$	$\geq 24.3$	$42.59 \pm 0.60$	$24.6 \pm 0.4$	$42.76 \pm 0.37$	$\leq 42.37$	13
NGC 5363	21.0	L	$40.39 \pm 0.23$	$40.00 \pm 0.30$	$\geq 24.3$	$41.50 \pm 0.60$	$\leq 23.7$	$40.20 \pm 0.44$	$\leq 41.85$	40, 45
NGC 5427	29.4	2	$\leq 41.71$	$\leq 40.06$				$\leq 41.83$	$\leq 42.14$	15
NGC 5643	20.9	2	$42.53 \pm 0.10$	$40.59 \pm 0.06$	$\geq 24.3$		$24.2 \pm 0.3$	$42.23 \pm 0.38$	$\leq 41.97$	47, 48, 49
NGC 6890	33.8	1.9/2	$42.60 \pm 0.09$	$40.59 \pm 0.30$	$\geq 24.3$	$42.38 \pm 0.60$	$24.3 \pm 0.4$	$42.30 \pm 0.38$	$\leq 42.26$	22
NGC 7212	116.0	2	$43.64 \pm 0.12$	$41.98 \pm 0.16$	$\geq 24.3$	$43.73 \pm 0.60$	$24.1 \pm 0.4$	$43.29 \pm 0.39$	$43.26 \pm 0.20$	13, 15, 50
NGC 7479	30.0	2	$43.27 \pm 0.06$	$40.67 \pm 0.36$	$24.3 \pm 0.45$	$41.99 \pm 0.60$	$24.7 \pm 0.5$	$42.94 \pm 0.37$	$42.34 \pm 0.12$	33, 22, 31
NGC 7743	19.2	2/L	$\leq 41.00$	$39.29 \pm 0.22$	$\geq 24.3$	$41.26 \pm 0.60$		$\leq 41.15$	$\leq 41.77$	51, 31, 45
PKS 1932–46	1191.0	1.9	$\leq 43.94$					$\leq 43.94$	$\leq 45.36$	
PKS 2158–380	149.0	2	$43.11 \pm 0.07$	$41.77 \pm 0.60$	$\geq 22.0$		$23.8 \pm 0.7$	$42.78 \pm 0.38$	$\leq 43.55$	7
PKS 2354–35	222.0	L	$\leq 42.47$	$\leq 39.67$				$\leq 42.55$	$\leq 43.90$	52
Superantennae S	291.0	2	$44.75 \pm 0.11$	$42.40 \pm 0.30$	$24.5 \pm 0.45$	$44.55 \pm 0.60$	$24.5 \pm 0.5$	$44.34 \pm 0.39$	$\leq 44.13$	53, 54, 55
UGC 12348	110.0	2	$43.55 \pm 0.06$					$43.20 \pm 0.38$	$43.08 \pm 0.19$	

– Notes: (1), (2), (3), and (4), short object name, distance, optical class, and nuclear 12  $\mu\text{m}$  luminosities from Asmus et al. (2014); (5) average observed 2–10 keV luminosity; (6) average X-ray column density from the literature; (7) average absorption-corrected 2–10 keV luminosity from the literature; (8) predicted X-ray column density using Eq. 6; (9) predicted absorption-corrected 2–10 keV luminosity using Eq. 2; (10) average observed 14–195 keV luminosity from *Swift*/BAT by combining the data of the 54 and 70 month source catalogues (Cusumano et al. 2010; Baumgartner et al. 2013); (11) references for the 2–10 keV luminosities and column densities: 1: Massaro et al. (2010); 2: Evans et al. (2008c); 3: Hardcastle et al. (2012); 4: Evans et al. (2006); 5: Evans et al. (2008b); 6: Hardcastle, Croston & Kraft (2007); 7: this work (XSPEC); 8: Massaro et al. (2012); 9: Balmaverde, Capetti & Grandi (2006); 10: Donato, Sambruna & Gliozzi (2004); 11: Gandhi et al. (2009); 12: Piconcelli et al. (2011); 13: Levenson et al. (2006); 14: Miyazawa, Haba & Kunieda (2009); 15: Guainazzi, Matt & Perola (2005); 16: de Rosa et al. (2008); 17: Pereira-Santaella et al. (2011); 18: Rodriguez, Tomsick & Chaty (2008); 19: Nardini & Risaliti (2011); 20: Teng et al. (2005); 21: Teng et al. (2008); 22: Brightman & Nandra (2011a); 23: Teng & Veilleux (2010); 24: Teng et al. (2009); 25: Mazzarella et al. (2012); 26: Shu et al. (2007); 27: Paggi et al. (2012); 28: Matt et al. (2003); 29: Marinucci et al. (2011); 30: Baloković et al. (2014); 31: Panessa et al. (2006); 32: Cappi et al. (2006); 33: Akylas & Georgantopoulos (2009); 34: Maiolino et al. (1998); 35: Marinucci et al. (2012a); 36: Hudaverdi et al. (2006); 37: Satyapal, Sambruna & Dudik (2004); 38: Liu (2011); 39: Ueda et al. (2001); 40: González-Martín et al. (2009b); 41: LaMassa et al. (2011); 42: Brightman & Nandra (2008); 43: Flohic et al. (2006); 44: Baldi et al. (2009); 45: González-Martín et al. (2009a); 46: Younes et al. (2011); 47: Bianchi, Guainazzi & Chiaberge (2006); 48: Matt et al. (2013); 49: Guainazzi et al. (2004); 50: Awaki et al. (2000); 51: Kharb et al. (2012); 52: Russell et al. (2013); 53: Braitto et al. (2009); 54: Teng et al. (in prep.); 55: Braitto et al. (2003);

Yaqoob 2012; Marinucci et al. 2012b). In fact, the intrinsic 2–10 keV luminosity estimates span two orders of magnitude (Yaqoob 2012). However, the most recent NuSTAR observations are consistent with the average luminosity adopted here (Puccetti et al. 2014). Despite this, the source is possibly beamed, in which case the isotropic emission estimates would be an order of magnitude too high (Yaqoob 2012). The X-ray spectral analysis also indicates that the CT obscurer has a small filling factor of only 0.1–0.15 and thus is relatively compact (e.g., Yaqoob 2012; Puccetti et al. 2014). In that case, the MIR emission of that obscurer would also be significantly lower compared to typical obscurers with filling factors of  $\sim 0.5$ .

Finally, data at multiple wavelengths provide ample evidence for unusually high foreground extinction towards the AGN in NGC 4945 even covering the narrow-line region (Moorwood et al. 1996; Spoon et al. 2000; Pérez-Beaupuits et al. 2011). This is, for example, evident from the extremely deep silicate absorption feature at  $9.7\ \mu\text{m}$ , implying an attenuation factor of  $\sim 25$  (1.4 dex) at  $12\ \mu\text{m}$  with large uncertainties of the order of 1 dex (Pérez-Beaupuits et al. 2011). A similar correction factor based on the ratio of the  $6.2$  to  $7.7\ \mu\text{m}$  PAH features was already used by Krabbe, Böker & Maiolino (2001) to correct the MIR emission of NGC 4945.

In conclusion, none of the effects described above can explain by themselves the extraordinary low MIR–X-ray of NGC 4945. Because of this high extinction also towards the narrow line region, corresponding intrinsic power estimates based on the emission lines [O III], [O IV], or [Ne V] can not be used to constrain the intrinsic MIR and X-ray luminosities either. It is beyond the scope of this work to further investigate the obviously complicated situation of this source. Note however, that interestingly, the ratio of the observed MIR to observed 2–10 keV ratio is consistent with the MIR–X-ray correlation.

Finally, this discussion suggests that other objects could also be affected by high foreground extinction which would be indicated by an extremely deep silicate  $9.7\ \mu\text{m}$  absorption feature. Indeed, the average MIR–X-ray ratio of sources with deep silicate features is lower than those of the type II and X-ray obscured AGN ( $\langle R_X^M \rangle = 0.15$ ,  $\sigma_X^M = 0.35$ ). However, of the three with the deepest silicate absorption in the reliable sample (ESO 506-27, NGC 4992, and NGC 7172), ESO 506-27 exhibits a high MIR–X-ray ratio ( $R_X^M = 0.52$ ). Furthermore, only NGC 5728 of the four objects with  $R_X^M < -0.3$  exhibits deep silicate  $9.7\ \mu\text{m}$  absorption (NGC 1144, NGC 3169, ESO 297-18 and NGC 5728; Asmus et al. 2014). Because of this ambiguity and the large difficulties to derive reliable attenuation factors, we refrain from applying an MIR absorption correction to the objects in this work. The numbers above demonstrate that such a correction would not alter the overall results derived here significantly.

### B3 Classification of uncertain AGN

The MIR Atlas of Asmus et al. (2014) also includes 38 uncertain AGN, galactic nuclei with insufficient or contradicting evidence for an accreting supermassive black hole being the main source of emission from those galactic nuclei. Most of these are nearby sources with low-luminosities. We have searched the literature for X-ray measurements of the objects with the same procedure as in Sect. 2. The properties of all uncertain AGN relevant here are summarized in Table B3, including predicted  $L^{\text{int}}(2\text{--}10\ \text{keV})$  and  $N_{\text{H}}$  from Equations 2 and 6 (whenever possible).

Eleven nuclei do not have any published X-ray de-

tection with sufficient counts for estimating even the observed flux in the 2–10 keV range (ESO 500-34, ESO 602-25, IRAS08572+3915, NGC 1433, NGC 3094, NGC 3607, NGC 3628, NGC 4746, NGC 5258, NGC 6221 and NGC 7590). Therefore,  $L^{\text{int}}(2\text{--}10\ \text{keV})$  can only be predicted, or constrained in case of MIR non-detections, for those objects. Note that two of X-ray non-detections, ESO 500-34 and NGC 6221, have actually been detected with *Swift*/BAT at 14–195 keV. Their predicted  $L^{\text{int}}(2\text{--}10\ \text{keV})$  values agree well with the expectation from the 2–10 keV–14–195 keV correlation (Sect. 4.2).

Another seven nuclei have no or contradicting intrinsic luminosity estimates (IC 883, IRAS 11095-0238, IRAS 15250+3609, NGC 3521, NGC 4418, NGC 5866 and NGC 6810). Three of these (IC 883, NGC 3521 and NGC 5866) are undetected in the MIR at subarcsecond scales, and again only  $L^{\text{int}}(2\text{--}10\ \text{keV})$  can be predicted. For the others also  $N_{\text{H}}$  predictions are possible and indicate Compton-thick obscuration for the nuclei in all four cases. However, for the three AGN/starburst composite candidates among them (IRAS 11095-0238, IRAS 15250+3609 and NGC 6810) again our diagnostics can not distinguish between CT obscured and star formation dominated nuclei.

The remaining 20 uncertain AGN have estimates for  $L^{\text{int}}(2\text{--}10\ \text{keV})$  directly from the X-ray data and are plotted as well in Fig. B2. Ten of these have only upper limits on their nuclear MIR luminosities, all of which are consistent with the MIR–X-ray correlation and thus with being real AGN. However, we note that 3C 264 and NGC 4785 exhibit quite low MIR–X-ray ratios ( $R_X^M < -0.15$ ), indicating that these sources are possibly not AGN powered. On the other hand, for NGC 4785 firm evidence for the presence of a CT AGN is presented by Gandhi et al. (2015) and used here for  $L^{\text{int}}(2\text{--}10\ \text{keV})$ . Thus, it is possible that NGC 4795 is also extinguished in the MIR similar to NGC 4945. Note that this scenario is very unlikely for 3C 264 as there is no evidence for significant obscuration (Appendix B4). From the other ten objects with both nuclear MIR detections and intrinsic X-ray luminosity estimates, six exhibit very high MIR–X-ray ratios ( $R_X^M > 1.2$ ). Among those are the AGN/starburst composites candidates IRAS 00188-0856, ESO 286-19, Mrk 266NE and NGC 1808. The former three are possibly CT obscured, while the latter, NGC 1808 is unlikely to host a heavily obscured AGN. Thus, we conclude that NGC 1808 is star formation dominated even on subarcsecond scales. The other two sources with high MIR–X-ray ratios are NGC 3627 and NGC 4303. Both do not show signs of heavy obscuration in the X-rays, and therefore we can conclude that their nuclear activity is not AGN-dominated. This finally leaves four uncertain AGN which exhibit nuclear MIR–X-ray ratios typical of AGN (NGC 613, NGC 3660, NGC 4438 and NGC 4457). NGC 613 and NGC 3660 are indeed good candidates for AGN-dominated nuclei, while for NGC 4438 and NGC 4457 large uncertainties remain owing to their possibly CT nature (see Appendix B4).

In summary, we note that the ambiguity in the MIR–X-ray ratio between a star formation dominated nucleus and CT AGN dominated nucleus severely constrain the diagnostic power of the MIR–X-ray correlation for many objects. Despite this, we manage to identify four nuclei (3C 264, NGC 1808, NGC 3627 and NGC 4303) as presumably not AGN powered and confirm AGN in another two (NGC 613 and NGC 3660).

**Table B2.** Properties of confirmed AGN/starburst composites.

Object	$D$ [Mpc]	Opt. class	$\log L^{\text{nuc}}$ (12 $\mu\text{m}$ ) [erg/s]	$\log L^{\text{obs}}$ (2–10 keV) [erg/s]	Lit. $\log N_{\text{H}}$ [ $\text{cm}^{-2}$ ]	Lit. $\log L^{\text{int}}$ (2–10 keV) [erg/s]	Pred. $\log N_{\text{H}}$ [ $\text{cm}^{-2}$ ]	Pred. $\log L^{\text{int}}$ (2–10 keV) [erg/s]	$\log L^{\text{obs}}$ (14–195 keV) [erg/s]	2–10 keV Ref.
(1)	(2)	(3)	(4)	(5)	(6)	(7)	(8)	(9)	(10)	(11)
3C 459	1125.0	Cp	$\leq 44.79$	$43.10 \pm 0.30$	$22.8 \pm 0.45$	$43.22 \pm 0.30$		$\leq 44.75$	$\leq 45.31$	1, 2
ESO 420-13	52.7	Cp	$43.20 \pm 0.08$					$42.87 \pm 0.38$	$\leq 42.65$	
III Zw 35N	121.0	Cp	$43.36 \pm 0.17$	$39.98 \pm 0.30$			$25.2 \pm 0.5$	$43.02 \pm 0.41$	$\leq 43.37$	3, 4
Mrk 520	115.0	Cp	$43.53 \pm 0.11$	$43.00 \pm 0.30$	$22.4 \pm 0.45$	$43.08 \pm 0.30$	$\leq 23.7$	$43.18 \pm 0.39$	$43.68 \pm 0.07$	5
Mrk 897	115.0	Cp	$42.51 \pm 0.12$					$42.22 \pm 0.39$	$\leq 43.33$	
NGC 2623	87.3	Cp	$43.61 \pm 0.20$	$40.96 \pm 0.30$	$\geq 24.3$		$24.7 \pm 0.5$	$43.26 \pm 0.42$	$\leq 43.09$	6, 7
NGC 3690E	49.1	Cp	$43.32 \pm 0.19$	$39.72 \pm 0.30$	$22.1 \pm 0.45$	$39.76 \pm 0.30$	$25.4 \pm 0.5$	$42.99 \pm 0.42$	$\leq 42.59$	8, 9
NGC 3690W	48.2	Cp	$43.75 \pm 0.21$	$41.49 \pm 0.30$	$24.6 \pm 0.45$	$43.26 \pm 0.60$	$24.5 \pm 0.5$	$43.39 \pm 0.43$	$\leq 42.57$	10
NGC 4945	3.7	Cp	$39.95 \pm 0.12$	$39.85 \pm$	$\geq 24.3$	$42.07 \pm 0.57$	$\leq 23.3$	$39.78 \pm 0.39$	$41.66 \pm 0.01$	11, 12
NGC 5953	31.4	Cp	$\leq 41.94$	$\leq 38.85$				$\leq 42.04$	$\leq 42.20$	13
NGC 6240N	114.0	Cp	$42.84 \pm 0.15$	$42.07 \pm 0.30$	0.45	$42.07 \pm 0.60$	$23.4 \pm 0.5$	$42.53 \pm 0.40$	$\leq 44.00$	14
NGC 6240S	113.0	Cp	$43.56 \pm 0.05$	$42.33 \pm 0.30$	$\geq 24.3$	$44.09 \pm 0.60$	$23.8 \pm 0.4$	$43.22 \pm 0.37$	$44.04 \pm 0.04$	15, 4, 16
NGC 7130	68.9	Cp	$43.18 \pm 0.08$	$40.84 \pm 0.30$	$\geq 24.3$	$42.81 \pm 0.60$	$24.5 \pm 0.4$	$42.85 \pm 0.38$	$42.96 \pm 0.18$	4, 17
NGC 7496	21.1	Cp	$42.35 \pm 0.03$					$42.07 \pm 0.37$	$\leq 41.85$	
NGC 7582	23.0	Cp	$42.85 \pm 0.07$	$41.42 \pm 0.27$	$23.1 \pm 0.25$	$42.38 \pm 0.25$	$23.9 \pm 0.4$	$42.53 \pm 0.38$	$42.71 \pm 0.02$	18, 16, 19
NGC 7592W	105.0	Cp	$43.65 \pm 0.14$	$40.72 \pm 0.30$			$24.9 \pm 0.5$	$43.30 \pm 0.39$	$\leq 43.25$	20
NGC 7679	71.7	Cp	$42.74 \pm 0.11$	$42.04 \pm 0.70$	$20.3 \pm 0.45$	$42.03 \pm 0.67$	$23.4 \pm 0.8$	$42.43 \pm 0.39$	$42.97 \pm 0.15$	21, 22
UGC 5101	182.0	Cp	$44.35 \pm 0.07$	$41.68 \pm 0.30$			$24.7 \pm 0.4$	$43.96 \pm 0.38$	$43.49 \pm 0.21$	16, 4

– *Notes:* (1), (2), (3), and (4), short object name, distance, optical class, and nuclear 12  $\mu\text{m}$  luminosities from Asmus et al. (2014); (5) average observed 2–10 keV luminosity; (6) average X-ray column density from the literature; (7) average absorption-corrected 2–10 keV luminosity from the literature; (8) predicted X-ray column density using Eq. 6; (9) predicted absorption-corrected 2–10 keV luminosity using Eq. 2; (10) average observed 14–195 keV luminosity from *Swift*/BAT by combining the data of the 54 and 70 month source catalogues (Cusumano et al. 2010; Baumgartner et al. 2013); (11) references for the 2–10 keV luminosities and column densities: 1: Massaro et al. (2012); 2: Mingo et al. (2014); 3: González-Martín et al. (2009b); 4: González-Martín et al. (2009a); 5: Winter et al. (2009a); 6: Evans et al. (2008a); 7: Maiolino et al. (2003); 8: Zezas, Ward & Murray (2003); 9: Ballo et al. (2004); 10: Ptak et al. (2015); 11: Yaqoob (2012); 12: Puccetti et al. (2014); 13: Guainazzi, Matt & Perola (2005); 14: Komossa et al. (2003); 15: Puccetti et al. (in prep); 16: Brightman & Nandra (2011a); 17: Levenson et al. (2005); 18: Bianchi et al. (2009b); 19: Dong et al. (2004); 20: Wang & Gao (2010); 21: Della Ceca et al. (2001); 22: Yankulova, Golev & Jockers (2007).

**Table B3.** Properties of uncertain AGN.

Object	<i>D</i> [Mpc]	Opt. class	$\log L^{\text{nuc}}$ (12 $\mu\text{m}$ ) [erg/s]	$\log L^{\text{obs}}$ (2-10 keV) [erg/s]	Lit. $\log N_{\text{H}}$ [ $\text{cm}^{-2}$ ]	Lit. $\log L^{\text{int}}$ (2-10 keV) [erg/s]	Pred. $\log N_{\text{H}}$ [ $\text{cm}^{-2}$ ]	Pred. $\log L^{\text{int}}$ (2-10 keV) [erg/s]	$\log L^{\text{obs}}$ (14-195 keV) [erg/s]	2-10 keV Ref.
(1)	(2)	(3)	(4)	(5)	(6)	(7)	(8)	(9)	(10)	(11)
3C 264	103.0	2:	$\leq 42.15$	$42.21 \pm 0.31$	$\leq 22.0$	$42.21 \pm 0.31$		$\leq 42.25$	$\leq 43.23$	1, 2
ESO 286-19	195.0	Cp:	$44.67 \pm 0.04$	$41.91 \pm 0.30$	$23.7 \pm 0.45$	$42.39 \pm 0.30$	$24.8 \pm 0.4$	$44.27 \pm 0.37$	$\leq 43.79$	3, 4, 5
ESO 500-34	60.2	Cp	$\leq 42.70$			$\pm$		$\leq 42.77$	$42.72 \pm 0.20$	
ESO 602-25	109.0	Cp:	$43.08 \pm 0.15$			$\pm$		$42.75 \pm 0.40$	$\leq 43.28$	
IC 883	109.0	Cp	$\leq 43.90$	$40.97 \pm 0.30$		$\pm$		$\leq 43.90$	$\leq 43.28$	6
IRAS 00188-0856	620.0	Cp	$44.87 \pm 0.04$	$41.87 \pm 0.30$	$\leq 21.0$	$41.71 \pm 0.30$	$25.0 \pm 0.4$	$44.46 \pm 0.37$	$\leq 44.79$	7, 8
IRAS 08572+3915	275.0	Cp	$45.13 \pm 0.09$	$\leq 41.36$		$\pm$	$25.5 \pm 0.3$	$44.71 \pm 0.38$	$\leq 44.08$	9, 10
IRAS 11095-0238	519.0	Cp:	$44.83 \pm 0.13$	$41.41 \pm$		$\pm$	$25.2 \pm 0.3$	$44.42 \pm 0.39$	$\leq 44.64$	8
IRAS 15250+3609	258.0	Cp:	$44.64 \pm 0.04$	$40.95 \pm 0.36$		$\pm$	$25.4 \pm 0.5$	$44.23 \pm 0.37$	$\leq 44.03$	7, 8
Mrk 266NE	130.0	Cp	$43.00 \pm 0.23$	$41.24 \pm 0.56$	$22.9 \pm 0.04$	$41.78 \pm 0.30$	$24.1 \pm 0.7$	$42.68 \pm 0.44$	$\leq 43.43$	11, 12, 13
NGC 1433	8.3	2:	$\leq 40.20$			$\pm$		$\leq 40.39$	$\leq 41.05$	
NGC 1614	71.0	Cp:	$\leq 43.72$	$41.20 \pm 0.30$	$21.3 \pm 0.45$	$41.23 \pm 0.30$		$\leq 43.73$	$\leq 42.91$	3
NGC 1808	12.3	Cp:	$42.18 \pm 0.04$	$40.13 \pm 0.30$	$22.1 \pm 1.16$	$40.17 \pm 0.30$	$24.3 \pm 0.4$	$41.90 \pm 0.37$	$\leq 41.38$	14, 3
NGC 253	3.2	Cp:	$\leq 41.49$	$38.80 \pm 0.51$	$23.5 \pm 0.30$	$39.66 \pm 0.30$		$\leq 41.62$	$\leq 40.21$	15, 16, 17
NGC 3094	40.8	2:	$43.71 \pm 0.04$			$\pm$		$43.35 \pm 0.37$	$\leq 42.43$	
NGC 3185	20.3	2:	$\leq 41.59$	$38.99 \pm 0.30$	$\geq 24.3$	$40.75 \pm 0.60$		$\leq 41.71$	$\leq 41.82$	18
NGC 3379	10.6	L	$\leq 40.04$	$37.80 \pm 0.30$	$\leq 22.0$	$37.78 \pm 0.30$		$\leq 40.24$	$\leq 41.26$	11, 12, 19
NGC 3486	13.7	2/L	$\leq 40.46$	$39.36 \pm 0.30$	$\leq 21.5$	$40.26 \pm 1.11$	$40.3 \pm 0.6$	$\leq 40.64$	$\leq 41.48$	18, 20, 3
NGC 3521	11.5	L/H	$\leq 40.60$	$38.67 \pm 0.30$		$\pm$		$\leq 40.77$	$\leq 41.33$	21
NGC 3607	21.4	2/L	$\leq 41.28$	$\leq 37.76$		$\pm$		$\leq 41.41$	$\leq 41.87$	11, 12, 19
NGC 3627	10.1	2/L	$40.60 \pm 0.11$	$38.72 \pm 0.62$	$20.7 \pm 0.45$	$38.70 \pm 0.64$	$24.2 \pm 0.7$	$40.40 \pm 0.39$	$\leq 41.21$	18, 22
NGC 3628	12.2	L/H	$\leq 40.66$	$\leq 37.10$		$\pm$		$\leq 40.83$	$\leq 41.37$	19
NGC 3660	60.8	1.8/2/L/H	$42.45 \pm 0.20$	$42.07 \pm 0.30$	$20.5 \pm 0.45$	$42.07 \pm 0.30$	$\leq 23.7$	$42.16 \pm 0.42$	$\leq 42.77$	20, 23
NGC 4303	15.2	2	$40.62 \pm 0.05$	$39.04 \pm 0.30$	$\leq 22.0$	$39.04 \pm 0.30$	$24.0 \pm 0.4$	$40.42 \pm 0.37$	$\leq 41.57$	24, 25
NGC 4418	37.8	2	$43.79 \pm 0.05$	$39.47 \pm 0.30$	$\geq 24.0$	$\pm$	$25.9 \pm 0.4$	$43.43 \pm 0.37$	$\leq 42.36$	26
NGC 4438	13.7	L/H	$40.76 \pm 0.11$	$39.02 \pm$	$\geq 24.3$	$40.65 \pm 0.60$	$24.1 \pm 0.3$	$40.55 \pm 0.38$	$\leq 41.48$	27, 12, 19
NGC 4457	17.4	L	$40.75 \pm 0.10$	$38.89 \pm 0.30$	$\geq 24.3$	$40.57 \pm 0.60$	$24.2 \pm 0.5$	$40.54 \pm 0.38$	$\leq 41.69$	11, 12, 19
NGC 4472	17.1	2/L	$\leq 40.87$	$39.00 \pm 0.30$		$39.00 \pm 0.30$		$\leq 41.03$	$\leq 41.67$	28, 18
NGC 4746	33.5	L/H	$\leq 41.56$			$\pm$		$\leq 41.69$	$\leq 42.26$	
NGC 4785	59.0	2	$\leq 42.26$	$41.00 \pm 0.30$	$\geq 24.3$	$42.80 \pm 0.60$		$\leq 42.35$	$\leq 42.75$	29
NGC 5258	107.0	L/H	$\leq 42.82$			$\pm$		$\leq 42.88$	$\leq 43.26$	
NGC 5813	29.7	L:	$\leq 41.25$	$39.06 \pm 0.30$	$21.1 \pm 0.45$	$39.06 \pm 0.30$		$\leq 41.38$	$\leq 42.15$	30, 12
NGC 5866	14.1	L/H	$\leq 40.72$	$38.32 \pm 0.14$		$\pm$		$\leq 40.88$	$\leq 41.50$	19, 11, 12
NGC 613	26.6	Cp	$41.77 \pm 0.11$	$40.96 \pm 0.30$	$23.6 \pm 0.45$	$41.55 \pm 0.30$	$23.5 \pm 0.5$	$41.51 \pm 0.39$	$\leq 42.05$	31
NGC 6221	10.7	Cp	$41.55 \pm 0.08$			$\pm$		$41.30 \pm 0.38$	$41.44 \pm 0.10$	
NGC 6810	28.6	Cp	$42.04 \pm 0.11$	$39.89 \pm$		$\pm$	$24.4 \pm 0.3$	$41.76 \pm 0.39$	$\leq 42.12$	3
NGC 7552	20.4	L/H	$\leq 41.90$	$40.13 \pm 0.04$	$\leq 21.0$	$40.17 \pm 0.30$		$\leq 42.00$	$\leq 41.82$	3, 21
NGC 7590	26.5	2:	$\leq 41.35$	$\leq 38.71$	$\geq 24.3$	$\pm$		$\leq 41.48$	$\leq 42.05$	32, 33, 34

– Notes: (1), (2), (3), and (4), short object name, distance, optical class, and nuclear 12  $\mu\text{m}$  luminosities from Asmus et al. (2014); (5) average observed 2-10 keV luminosity; (6) average X-ray column density from the literature; (7) average absorption-corrected 2-10 keV luminosity from the literature; (8) predicted X-ray column density using Eq. 6; (9) predicted absorption-corrected 2-10 keV luminosity using Eq. 2; (10) average observed 14-195 keV luminosity from *Swift*/BAT by combining the data of the 54 and 70 month source catalogues (Cusumano et al. 2010; Baumgartner et al. 2013); (11) references for the 2-10 keV luminosities and column densities: 1: Evans et al. (2006); 2: Donato, Sambruna & Gliozzi (2004); 3: Brightman & Nandra (2011a); 4: Franceschini et al. (2003); 5: Misaki et al. (1999); 6: Modica et al. (2012); 7: Teng et al. (2005); 8: Teng & Veilleux (2010); 9: Teng et al. (2009); 10: LaMassa et al. (2011); 11: González-Martín et al. (2009b); 12: González-Martín et al. (2009a); 13: Mazzarella et al. (2012); 14: Jiménez-Bailón et al. (2005); 15: Lehmer et al. (2013); 16: Weaver et al. (2002); 17: Müller-Sánchez et al. (2010); 18: Panessa et al. (2006); 19: Flohic et al. (2006); 20: Brightman & Nandra (2008); 21: Grier et al. (2011); 22: Hernández-García et al. (2013); 23: Bianchi et al. (2012); 24: Jiménez-Bailón et al. (2003); 25: Tzanavaris & Georgantopoulos (2007); 26: Maiolino et al. (2003); 27: Machacek, Jones & Forman (2004); 28: Maccarone, Kundu & Zepf (2003); 29: Gandhi et al. (2015); 30: Hernández-García et al. (2014); 31: Castangia et al. (2013); 32: Bassani et al. (1999); 33: Shu, Liu & Wang (2010); 34: Shu et al. (2012).



## B4 Notes on selected objects

### B4.1 3C 264 – NGC 3862

3C 264 is a FRI radio source harboured in NGC 3862 with a tentative Sy 2/LINER classification. It has not been detected at sub-arcsecond resolution in the MIR. The *XMM-Newton* and *Chandra* data (Donato, Sambruna & Gliozzi 2004; Evans et al. 2006) suggest an unabsorbed X-ray luminosity that is still consistent with the expected upper limit value from the MIR–X-ray correlation but does not leave much room for the MIR flux of an actively accreting nucleus in 3C 264.

### B4.2 3C 305

Evans et al. (2008c) did not detect the nucleus of 3C 305 in *XMM-Newton* data. Hardcastle et al. (2012) detect the nucleus embedded in extended soft emission based on *Chandra* observations. While they provide an unabsorbed fit ( $\log L^{\text{int}}(2\text{--}10\text{ keV}) = 40.3$ ), they state that the source might be highly obscured. Therefore, the source is excluded from the reliable sample. The MIR–X-ray correlation provides an upper limit on  $\log L^{\text{int}}(2\text{--}10\text{ keV}) = 42.7$ , not constraining the highly obscured scenario.

### B4.3 3C 327

3C 327 was observed with *Chandra* (Evans et al. 2007). We analyzed the data and find the source to be most likely Compton-thick obscured with a strong Fe K $\alpha$  line. Unfortunately, the S/N of the detection is insufficient for a proper modelling of the X-ray spectrum. Therefore, we assume a similar geometry of the reflector to other well known CT AGN with an albedo of 0.022 and a reflection fraction of 0.04 (similar to NGC 1068). Owing to all these assumptions and uncertainties, 3C 327 is excluded from the reliable sample. The resulting intrinsic luminosity estimate from our X-ray analysis ( $\log L^{\text{int}}(2\text{--}10\text{ keV}) = 45.3$ ) is  $\sim 1$  dex higher than the expectation from the MIR–X-ray correlation, while the Compton-thickness is verified.

### B4.4 3C 424

The nucleus of 3C 424 was only faintly detected with *Chandra* (Massaro et al. 2012). Reliable modelling of the intrinsic X-ray luminosity is not possible, and thus, 3C 424 is excluded from the reliable sample.

### B4.5 3C 449

The X-ray emission of 3C 449 is dominated by soft extended emission and no nuclear hard point source was detected during *Chandra* observations (Balmaverde, Capetti & Grandi 2006). Thus, the lower resolution *XMM-Newton* data can not be used to analyse the AGN (Donato, Sambruna & Gliozzi 2004), and 3C 449 is excluded from the reliable sample.

### B4.6 ESO 253-3

No X-ray properties are published for ESO 253-3 but it has been observed with *Swift*/XRT. The corresponding X-ray spectrum suffers from low S/N and shows heavy obscuration. It can be fit with the combination of an absorbed and an unabsorbed power-law ( $\Gamma_1 = 2.56; \Gamma_2 = 1.75; \log L^{\text{int}}(2\text{--}10\text{ keV}) = 42.9; \log N_{\text{H}} = 23.5$ ).

As noted in Asmus et al. (2014), ESO 253-3 possibly hosts a double AGN which would be unresolved with XRT. Owing to this, the low S/N, and thus ill constrained obscuration, we conservatively exclude ESO 253-3 from the reliable sample. Indeed, the MIR–X-ray correlation predicts a value of  $\log L^{\text{int}}(2\text{--}10\text{ keV})$  more than an order of magnitude higher and possibly CT obscuration.

### B4.7 ESO 286-19

Ptak et al. (2003) do not find any evidence for an AGN in the relatively deep *Chandra* data of the AGN candidate ESO 286-19 (see also Iwasawa et al. 2011). On the other hand, Franceschini et al. (2003) and Brightman & Nandra (2011a) claim the detection of an obscured AGN in the shallower *XMM-Newton* data. This claim is backed up by the analysis of deep *ASCA* data also finding an AGN component (Misaki et al. 1999). The average intrinsic X-ray luminosity found is  $\log L^{\text{int}}(2\text{--}10\text{ keV}) = 42.39$ . The nuclear MIR emission predicts a much higher  $\log L^{\text{int}}(2\text{--}10\text{ keV}) = 44.3$  and Compton-thick obscuration,  $\log N_{\text{H}} = 24.8 \pm 0.44$ , assuming the  $L^{\text{obs}}(2\text{--}10\text{ keV})$  from Brightman & Nandra (2011a). Heavy obscuration is also indicated by the very deep silicate absorption features in the MIR spectrum. However, significant star formation might be present since ESO 286-19 is a merger system. Clearly more data are needed to determine the dominating power source in this system.

### B4.8 ESO 500-34

We did not find any 2-10 keV X-ray data on the AGN candidate in ESO 500-34 but it was detected at 14-195 keV in the 54 month BAT catalogue with a luminosity of  $L^{\text{obs}}(14\text{--}195\text{ keV}) = 42.72$  (Cusumano et al. 2010; but not in the 70 month). The nuclear MIR emission upper limit provides an upper limit on the intrinsic X-ray luminosity of  $\log L^{\text{int}}(2\text{--}10\text{ keV}) \leq 42.8$  through the MIR–X-ray correlation. This agrees well with the expectation from the 14-195 keV luminosity.

### B4.9 IC 883

IC 883 is an infrared luminous galaxy with an uncertain AGN/starburst composite nucleus. For the nuclear MIR flux only an upper limit is available. Iwasawa et al. (2011) present *Chandra* data on this object showing a complex morphology with indication but no clear evidence of an AGN (see also discussion in Modica et al. 2012). The upper limit on the intrinsic X-ray luminosity of any AGN in IC 883 from the MIR–X-ray correlation is  $\log L^{\text{int}}(2\text{--}10\text{ keV}) \leq 43.9$ , so leaves sufficient room for a highly obscured AGN.

### B4.10 IC 4518W

de Rosa et al. (2008) and Pereira-Santaella et al. (2011) analyse the *XMM-Newton* data on IC 4518W that were taken only few days apart but find more than one dex different values for  $L^{\text{obs}}(2\text{--}10\text{ keV})$  (and also  $L^{\text{int}}(2\text{--}10\text{ keV})$ ). The analysis by Rodriguez, Tomsick & Chaty (2008) of *Swift*/XRT data yields intermediate results between the above values. All works agree on a high obscuration ( $\log N_{\text{H}} = 23.29$ ). Owing to the inconsistency of the different measurements, IC 4518W is excluded from the reliable sample. Interestingly, the predictions for  $L^{\text{int}}(2\text{--}10\text{ keV})$  and  $N_{\text{H}}$  are in best agreement with Rodriguez, Tomsick & Chaty (2008) and thus the average of all the above measurements.

*B4.11 III Zw 35*

González-Martín et al. (2009b) analysed the *Chandra* and *XMM-Newton* data of the AGN/starburst composite III Zw 35 and faintly detected the northern nucleus, which holds the AGN in this merger system. However, the S/N is insufficient to perform a spectral analysis and the X-ray luminosity can only be estimated ( $\log L^{\text{obs}}(2-10 \text{ keV}) = 40$ ). Based on the very low X-ray-[O III] ratio, González-Martín et al. (2009a) then suggests that the AGN might be Compton-thick obscured. This scenario would agree with the prediction from the MIR–X-ray correlation ( $\log L^{\text{int}}(2-10 \text{ keV}) = 43.0 \pm 0.4$ ;  $\log N_{\text{H}} = 25.2 \pm 0.5$ ). On the other hand, the spectral information in the MIR at subarcsecond scales is insufficient to exclude significant star formation contamination of the nuclear MIR luminosity estimate.

*B4.12 IRAS 00188-0856*

The ultra luminous infrared galaxy IRAS 00188-0856 possibly contains an AGN/starburst composite nucleus, which was detected in the MIR at subarcsecond scales. It was also detected with *Chandra* but with an insufficient S/N for spectral analysis (Teng et al. 2005). The deeper *XMM-Newton* data have a better S/N and are fitted with an unabsorbed model in Teng & Veilleux (2010) resulting in  $\log L^{\text{int}}(2-10 \text{ keV}) = 41.71$ , without further discussion. The resultant very high MIR–X-ray ratio of IRAS 00188-0856 suggests that this source is either completely star formation dominated or contains a Compton-thick AGN with an intrinsic X-ray luminosity of  $\log L^{\text{int}}(2-10 \text{ keV}) = 44.5 \pm 0.4$ . Note that the very deep silicate absorption features in the MIR indicate heavy obscuration towards the nucleus consistent with the CT scenario.

*B4.13 IRAS 01003-2238*

IRAS 01003-2238 was only detected below 5 keV during *XMM-Newton* observations (Nardini & Risaliti 2011). The detection with *Chandra* was too faint for any extraction of AGN properties (Teng et al. 2005). Nardini & Risaliti (2011) interpret the data as IRAS 01003-2238 hosting a Compton-thick obscured AGN. Conversely, it is excluded from the reliable sample. The scenario of heavy obscuration is supported by the predictions from the MIR–X-ray correlations and the deep silicate absorption features (Asmus et al. 2014).

*B4.14 IRAS 04103-2838*

IRAS 04103-2838 was only very weakly detected with *Chandra* (Teng et al. 2005). More information can be extracted from *XMM-Newton* data which indicate that the AGN is CT obscured (Teng et al. 2008). Therefore, no reliable  $L^{\text{int}}(2-10 \text{ keV})$  estimate is possible and the source is excluded from the reliable sample. The diagnostics based on the MIR–X-ray correlation support the CT scenario.

*B4.15 IRAS 05189-2524*

X-ray observations of IRAS 05189-2524 provide very different results (Teng et al. 2009; Teng & Veilleux 2010; Brightman & Nandra 2011a). In particular, Teng et al. (2009) note that during the latest *Suzaku* observations, the observed flux was a factor of 30 lower because of the AGN either turning off or a dramatic increase in obscuration. Owing to this, the average intrinsic X-ray luminosity of

IRAS 05189-2524 is very uncertain, and thus the object is excluded from the reliable sample. The MIR–X-ray correlation in fact predicts a high intrinsic luminosity ( $\log L^{\text{int}}(2-10 \text{ keV}) = 44.5 \pm 0.4$ ) and CT obscuration. The most recent X-ray observations with *NuSTAR* however suggest that the AGN is not CT obscured (Teng et al., in prep.).

*B4.16 IRAS 08572+3915*

IRAS 08572+3915 is another ultra luminous infrared galaxy with an uncertain AGN/starburst composite nucleus. While, it was detected in the mid-infrared at subarcsecond scales, no X-ray detection could be achieved with *XMM-Newton* and *Suzaku*. Only in the soft X-ray band, the source is detected in *Chandra* observations (Teng et al. 2009). Under the assumption that the nuclear MIR emission is AGN-dominated, the intrinsic X-ray luminosity is predicted to be  $\log L^{\text{int}}(2-10 \text{ keV}) = 44.7 \pm 0.4$  with  $\log N_{\text{H}} = 25.0 \pm 0.4$  according to the MIR–X-ray correlation. This scenario would also be consistent with the deep silicate absorption features present in the MIR.

*B4.17 IRAS 11095-0238*

The ultra luminous infrared galaxy IRAS 11095-0238 was only very weakly detected with *Chandra*, not allowing a detailed spectral analysis (Teng & Veilleux 2010). The observed X-ray luminosity is  $\log L^{\text{obs}}(2-10 \text{ keV}) = 41.41$  while the MIR–X-ray correlation predicts an intrinsic X-ray luminosity of  $\log L^{\text{int}}(2-10 \text{ keV}) = 44.55 \pm 0.39$  and Compton-thick obscuration ( $\log N_{\text{H}} = 25.24 \pm 0.35$ ) if a powerful AGN is indeed present in this object. Heavy obscuration is also indicated by the extremely deep silicate absorption features in the MIR spectrum. However, strong star formation even dominating the MIR can not be excluded with the current data.

*B4.18 IRAS 15250+3609*

IRAS 15250+3609, an ultra luminous infrared galaxy and AGN candidate, was first detected in X-rays with *Chandra* (Teng et al. 2005). However, the detection was too faint for any further analysis. A better detection was achieved with later *XMM-Newton* observations, indicating that the object is Compton-thick obscured in X-rays (Teng & Veilleux 2010). Therefore, no reliable intrinsic luminosity estimate could be given. The MIR–X-ray correlation indicates  $\log L^{\text{int}}(2-10 \text{ keV}) = 44.36 \pm 0.37$  and also Compton-thickness ( $\log N_{\text{H}} = 25.43 \pm 0.48$ ). The MIR spectrum shows heavy obscuration through deep silicate absorption features as well. Similar to IRAS 11095-0238, star formation can not be excluded as main driver of the nuclear MIR emission however, and thus the results are not sufficient to proof the presence of a Compton-thick AGN in IRAS 15250+3609.

*B4.19 Mrk 266*

Mrk 266 is a merger system hosting possibly a double AGN, the confirmed Sy2 Mrk 266SW, and the composite candidate Mrk 266NE. A comprehensive study of both nuclei based on *XMM-Newton* and *Chandra* data is presented in Mazzarella et al. (2012) and is used here. Only in *Chandra*, the emission from both nuclei is resolved and can be disentangled. Mrk 266SW turns out to be the apparently fainter nucleus in X-rays. The low S/N of the

detection does not allow for a detailed spectral fitting. The observed X-ray luminosity is  $\log L^{\text{obs}}(2\text{-}10\text{ keV}) = 41.44$ . However, the flat spectral slope and presence of a strong Fe  $K\alpha$  line indicate that Mrk 266SW is heavily obscured. Thus, the X-ray properties of Mrk 266SW are not reliable. The nuclear MIR luminosity predicts an intrinsic X-ray luminosity of  $\log L^{\text{int}}(2\text{-}10\text{ keV}) = 42.14 \pm 0.38$  and heavy but Compton-thin obscuration ( $\log N_{\text{H}} = 23.6 \pm 0.4$ ). The brighter observed X-ray spectrum of Mrk 266NE, on the other hand, can be modelled with an absorbed power-law with a moderate column density,  $\log N_{\text{H}} = 22.91$ , resulting in an intrinsic X-ray luminosity of  $\log L^{\text{int}}(2\text{-}10\text{ keV}) = 41.74$ . González-Martín et al. (2009b) find a similar  $L^{\text{int}}(2\text{-}10\text{ keV})$  and  $N_{\text{H}}$  from analysing the same data despite stating a significantly higher observed 2–10 keV flux. On the other hand, González-Martín et al. (2009a) mention that Mrk 266NE might be Compton-thick obscured based on the X-ray–[O III] ratio with a much higher intrinsic X-ray luminosity ( $\log L^{\text{int}}(2\text{-}10\text{ keV}) = 43.56$ ). The predicted  $\log L^{\text{int}}(2\text{-}10\text{ keV}) = 42.69 \pm 0.44$  from the MIR–X-ray correlation is in between both obscuration scenarios while the predicted column density is in fact mildly CT ( $\log N_{\text{H}} = 24.12 \pm 0.69$ ). Unfortunately there is no MIR spectral information available at subarcsecond scales, which would give information about nuclear star formation and obscuration. However, both are strong on larger scales (Asmus et al. 2014), so that we can not distinguish whether the nuclear MIR emission of Mrk 266NE is star formation dominated, or whether it is AGN dominated with heavy obscuration.

#### B4.20 NGC 34

Unfortunately, only one X-ray observation has been analyzed and published so far for NGC 34. Guainazzi, Matt & Perola (2005) and Brightman & Nandra (2011a) model the object as highly obscured (but Compton-thin), while Shu et al. (2007) claim that the obscuration is Compton-thick. The latter is supported by the low X-ray–[O III] ratio but on the other hand no Fe  $K\alpha$  line was detected. Esquej et al. (2012) argue that the nucleus of NGC 34 is instead starburst dominated which is consistent with the MIR data (see also Asmus et al. 2014). Therefore, NGC 34 is excluded from the reliable sample. Owing to the possible star formation contamination of the subarcsecond MIR luminosity, the prediction for  $L^{\text{int}}(2\text{-}10\text{ keV})$  from MIR–X-ray correlation is not reliable.

#### B4.21 NGC 253

The presence of an AGN in the nearby starburst galaxy NGC 253 has been controversially discussed throughout the literature. In X-rays, an obscured point source, X-1, was detected close to the nucleus with *Chandra* (Weaver et al. 2002). While it does not coincide with the compact non-thermal radio source it is within the range of possible location for the dynamical centre of NGC 253 (Müller-Sánchez et al. 2010). Interestingly, during the deep *Chandra*/*NuSTAR* monitoring in 2012, X-1 was not detected but a similarly bright source  $\sim 1$  arcsec away (Lehmer et al. 2013). This new source however, has a different X-ray spectrum and its location is incompatible with X-1. Its properties are typical for an ultraluminous X-ray binary. In addition, the high energy emission detected by *NuSTAR* does not match expectations from an AGN as source. Combining all results, it is not clear whether X-1 is an X-ray binary or obscured AGN. Since no compact MIR source was detected at subarcsecond scales at the centre of NGC 253, its AGN nature is still unclear. The corresponding MIR upper limit puts through the

MIR–X-ray correlation an upper limit on the intrinsic X-ray luminosity of  $\log L^{\text{int}}(2\text{-}10\text{ keV}) \leq 41.52$ , well compatible with the estimates from Weaver et al. (2002) and Müller-Sánchez et al. (2010).

#### B4.22 NGC 613

The AGN candidate in NGC 613 has been observed with *XMM-Newton* and shows a heavily obscured but Compton-thin X-ray spectrum with an intrinsic luminosity of  $\log L^{\text{int}}(2\text{-}10\text{ keV}) = 41.55$ . The predicted value from the MIR–X-ray correlation is in good agreement, as well as the predicted X-ray column density. Together with the compact MIR morphology at subarcsecond scales, this strongly favours the presence of an AGN in NGC 613 in addition to the circumnuclear star formation.

#### B4.23 NGC 1614

Risaliti et al. (2000) were the first to claim the existence of an AGN in the starburst galaxy NGC 1614 from *BeppoSAX* observations. Brightman & Nandra (2011a) provide the analysis of newer *XMM-Newton* data and find a merely obscured AGN with  $\log L^{\text{int}}(2\text{-}10\text{ keV}) = 41.23$ . However, Herrero-Illana et al. (2014) argue using recent *Chandra* data that there is no evidence for an AGN in NGC 1614. An AGN was also not clearly detected in the subarcsecond MIR observations. The corresponding upper limit from the MIR–X-ray correlation is  $\log L^{\text{int}}(2\text{-}10\text{ keV}) \leq 43.79$  and thus not constraining the presence of an AGN.

#### B4.24 NGC 1667

NGC 1667 appears to be Compton-thick obscured in the *ASCA*, *XMM-Newton* and *Suzaku* observations (Panessa et al. 2006; Brightman & Nandra 2011a; Marinucci et al. 2012a). However, no *Chandra* data have been published for this low-luminosity AGN and it remains uncertain how strongly the lower resolution data of the other telescopes are affected by extended host emission. No reliable intrinsic X-ray luminosity estimate is available for NGC 1667 and it is thus excluded from reliable sample. The predictions from the MIR–X-ray correlation agree better with Compton-thin obscuration but would as well be affected by host contamination of  $L^{\text{obs}}(2\text{-}10\text{ keV})$ .

#### B4.25 NGC 1808

A long-term variable hard X-ray source in the starburst galaxy NGC 1808 was first detected by Awaki et al. (1996) using *ASCA*. Jiménez-Bailón et al. (2005) then used *Chandra* and *XMM-Newton* to resolve the individual sources in this galaxy and find a central ultra luminous X-ray source or low-luminosity AGN without significant obscuration. Brightman & Nandra (2011a) analysed only the *XMM-Newton* data and find a slightly more powerful and moderately obscured AGN. In the MIR, a compact but resolved source was detected at subarcsecond scales. As indicated by the corresponding MIR spectrum, the emission is still star formation dominated at these scales (see also González-Martín et al. 2013). This explains the offset position of NGC 1808 in the MIR–X-ray plane close to pure starburst galaxies. Conversely, the predicted intrinsic X-ray luminosity from the MIR–X-ray correlation of  $\log L^{\text{int}}(2\text{-}10\text{ keV}) = 41.85$  and obscuring column density  $\log N_{\text{H}} = 24.31$  have to be regarded as upper limits for the AGN in NGC 1808.

*B4.26 NGC 2623*

The AGN/starburst composite NGC 2623 harbours most likely a Compton-thick obscured AGN. This is indicated by the observed X-ray spectral properties, like the extremely hard spectral index, as found from *Chandra* data (Maiolino et al. 2003). Unfortunately, the *XMM-Newton* observations were not sufficiently deep for a detailed spectral analysis (Evans et al. 2008a). The CT scenario is supported by the predictions from the MIR–X-ray correlation ( $\log L^{\text{int}}(2-10 \text{ keV}) = 43.31 \pm 0.42$ ;  $\log N_{\text{H}} = 24.72 \pm 0.48$ ), which are close to the intrinsic luminosity estimate from Maiolino et al. (2003) assuming one per cent reflection efficiency. We note however that the nuclear MIR emission might still be significantly star formation contaminated (Asmus et al. 2014). Therefore, our predictions could be overestimations.

*B4.27 NGC 3185*

The optically borderline AGN in NGC 3185 has so far only been observed with *XMM-Newton*. The corresponding data were analysed in Cappi et al. (2006) and Panessa et al. (2006) who claim a Compton-thick source based on the data. It was not detected in the MIR at subarcsecond resolution but the upper limit on the intrinsic X-ray luminosity estimated from the MIR–X-ray correlation is consistent with the  $L^{\text{int}}(2-10 \text{ keV})$  estimate in Panessa et al. (2006). From the current data no further conclusion about the AGN nature of NGC 3185 can be drawn.

*B4.28 NGC 3312*

The only publication of X-ray data for NGC 3312 is still Hudaverdi et al. (2006) who state the global luminosity only. Therefore, we remove NGC 3312 from the reliable sample.

*B4.29 NGC 3379*

The uncertain LINER AGN in NGC 3379 shows several comparable X-ray point sources in the nuclear region, and Flohic et al. (2006) identifies the most central but not brightest one as low-luminosity AGN with an observed X-ray luminosity of  $\log L^{\text{obs}}(2-10 \text{ keV}) = 37.23$ . González-Martín et al. (2009b) estimate a higher X-ray luminosity ( $\log L^{\text{obs}}(2-10 \text{ keV}) = 38.1$ ) from the same data but note that the low S/N makes reliable estimates difficult. Based on the low X-ray–[O III] ratio, González-Martín et al. (2009a) argue that the LLAGN in NGC 3379 is in fact Compton-thick obscured with  $\log L^{\text{int}}(2-10 \text{ keV}) = 39.91$ . The upper limit on the intrinsic X-ray luminosity from the MIR–X-ray correlation would be compatible with this scenario ( $\log L^{\text{int}}(2-10 \text{ keV}) = 40.04$ ).

*B4.30 NGC 3486*

NGC 3486 hosts a borderline Sy2/LINER nucleus with uncertain power source. The nucleus remains undetected in a *Chandra* snapshot survey (Ho et al. 2001) and only appears in the much deeper *XMM-Newton* data (Cappi et al. 2006). While Brightman & Nandra (2008) favours a Compton-thick obscuration scenario for the source, Brightman & Nandra (2011a) provide only an unobscured fit to the *XMM-Newton* data without further discussion. The luminosity estimates range from  $39.63 \leq \log L^{\text{int}}(2-10 \text{ keV}) \leq 41.5$  depending on the assumed model. The subarcsecond scale MIR upper limit together with the MIR–X-ray correlation predicts

$L^{\text{int}}(2-10 \text{ keV}) \geq 40.47$ , which is inconsistent with the CT scenario if NGC 3486 is indeed AGN powered.

*B4.31 NGC 3521*

Grier et al. (2011) list the observed 0.3–8 keV flux for the uncertain LINER AGN in NGC 3521 using the deeper of the two *Chandra* observations, unfortunately without providing any further details on the X-ray analysis. We assume a power-law with  $\Gamma = 1.7$  to calculate an  $\log L^{\text{obs}}(2-10 \text{ keV}) = 38.67$ . The upper limit on the intrinsic X-ray luminosity of any AGN in NGC 3521 is  $\log L^{\text{int}}(2-10 \text{ keV}) \leq 40.61$  as predicted from the MIR–X-ray correlation.

*B4.32 NGC 3607*

As already reported in Asmus et al. (2014), the AGN candidate in NGC 3607 has not been detected in X-rays (Terashima et al. 2002; Flohic et al. 2006), nor in the sub-arcsecond MIR observations. González-Martín et al. (2009a) argue that a Compton-thick AGN could be present indicated by the X-ray to [O III] flux ratio. Unfortunately, the upper limit in the MIR and the MIR–X-ray correlation are not constraining enough to favour any scenario for NGC 3607.

*B4.33 NGC 3627*

NGC 3627 contains a low-luminosity AGN candidate, which remained undetected in the first snapshot *Chandra* observations (Ho et al. 2001). Furthermore, Panessa et al. (2006) argue that the *XMM-Newton* data on this source is significantly contaminated by off-nuclear emission and thus not usable to extract information about the nucleus. They derive an upper limit on the observed X-ray luminosity of  $\log L^{\text{obs}}(2-10 \text{ keV}) \leq 38.25$ . On the other hand, Hernández-García et al. (2013) analyse a deeper *Chandra* observation from 2008 and find  $\log L^{\text{obs}}(2-10 \text{ keV}) = 39.15$ . They attribute this  $\sim 1$  dex difference to the different model used but do not comment on the fact that the earlier value was also an upper limit. The nuclear MIR flux suggests an even higher intrinsic X-ray luminosity and heavy obscuration ( $\log L^{\text{int}}(2-10 \text{ keV}) = 40.25 \pm 0.39$ ;  $\log N_{\text{H}} = 24.2 \pm 0.71$ ). However, in Asmus et al. (2014), we point out that even the subarcsecond measurement of the nuclear MIR flux is presumably contaminated by nuclear star formation (see also Masegosa et al. 2011). While our results here are consistent with the presence of an AGN in NGC 3627, it presumably is not energetically important even on nuclear scales.

*B4.34 NGC 3628*

Flohic et al. (2006) analysed the deepest of the *Chandra* observations of the AGN candidate NGC 3628 and does not detect a nuclear point source but only diffuse emission due to star formation. They derive an upper limit on the observed X-ray luminosity of  $\log L^{\text{obs}}(2-10 \text{ keV}) = 37.1$ . Owing to the number of relatively bright circumnuclear sources, the *XMM-Newton* data are not usable to determine the properties of the putative AGN. The MIR–X-ray relation puts an upper limit on the intrinsic X-ray emission of any AGN to  $\log L^{\text{int}}(2-10 \text{ keV}) = 40.67$ .

## B4.35 NGC 3660

Based on *ASCA* observations which show an unabsorbed and variable powerful source in NGC 3660, Brightman & Nandra (2008) classified this object as a true Seyfert 2 candidate. This finding was supported by new *XMM-Newton* data presented in Bianchi et al. (2012). However, in Asmus et al. (2014), we conservatively classified NGC 3660 only as candidate AGN because of the controversial optical classifications spanning everything between H II region and Sy 1.8 (see also Shi et al. (2010)). This controversy is likely caused by a nuclear starburst that dilutes the optical spectra. Its position directly on the MIR–X-ray correlation supports the AGN nature but would favour the existence of a dusty nuclear structure as well. However, as pointed out in Asmus et al. (2014), the nuclear MIR emission is likely contaminated or even dominated by a nuclear starburst. While this could mean the absence of a torus in NGC 3660, Shi et al. (2010) argue that broad optical emission lines are actually present and thus NGC 3660 would not be a true Seyfert 2 in any case.

## B4.36 NGC 3690 – Arp 299

NGC 3690 is a merger system with two AGN, NGC 3690E (Arp 299A; sometimes wrongly called IC 694; see NED and Yamaoka et al. 1998) and NGC 3690W (Arp 299B). First evidence for the presence of an highly obscured AGN came from *BepoSAX* observations (Della Ceca et al. 2002), while the presence of a double AGN was then later postulated on the basis of *Chandra* and *XMM-Newton* observations (Zezas, Ward & Murray 2003; Ballo et al. 2004). Recently, NGC 3690 was observed with *NuSTAR*, where only NGC 3690W was detected above 10 keV and thus contributes at least 90 per cent of the observed hard X-rays (Ptak et al. 2015). Its intrinsic luminosity is estimated to be  $\log L^{\text{int}}(2-10 \text{ keV}) = 43.26$  with an obscuring column density of  $\log N_{\text{H}} = 24.6$ . NGC 3690E, on the other hand, has to be much fainter or even more obscured (see also Alonso-Herrero et al. 2013). The predicted X-ray properties from the MIR–X-ray correlation ( $\log L^{\text{int}}(2-10 \text{ keV}) = 43.45 \pm 0.43$ ;  $\log N_{\text{H}} = 24.46 \pm 0.49$ ) for NGC 3690W match very well the direct estimates from *NuSTAR*, while those for NGC 3690E ( $\log L^{\text{int}}(2-10 \text{ keV}) = 43.02 \pm 0.43$ ;  $\log N_{\text{H}} = 25.37 \pm 0.49$ ) agree with the highly CT scenario. However, as pointed out in Asmus et al. (2014), the nuclear MIR fluxes of both nuclei might still be significantly contaminated by star formation. In particular, NGC 3690E might be completely star formation dominated.

## B4.37 NGC 3982

The nucleus of NGC 3982 was detected only with a few counts above 2 keV (Guainazzi, Matt & Perola 2005; LaMassa et al. 2011). It is embedded in extended host emission, which heavily contaminates lower resolution X-ray data from *ASCA* (Panessa et al. 2006) and *XMM-Newton* (Brightman & Nandra 2011a). Still, the nucleus might be heavily obscured (Ghosh et al. 2007). Therefore,  $L^{\text{int}}(2-10 \text{ keV})$  is highly uncertain, and we have to exclude NGC 3982 from the reliable sample. The predictions from the MIR–X-ray correlation are consistent with heavy obscuration.

## B4.38 NGC 4303

The case of NGC 4303 was already discussed in Asmus et al. (2011) in the context of the MIR–X-ray correlation. The existence

of a low-luminosity AGN in this object as indicated in X-rays (Jiménez-Bailón et al. 2003; Tzanavaris & Georgantopoulos 2007) can not be verified owing to the presence of a nuclear star cluster, which presumably dominates the subarcsecond MIR emission in this object. We conclude that if an AGN is present in NGC 4303 it is not energetically important even on nuclear scales.

## B4.39 NGC 4418

Little information is available about the X-ray properties of the Sy 2 candidate NGC 4418. Apparently it remained undetected during *ASCA* observations in 1994. Maiolino et al. (2003) published *Chandra* data from 2003 in which the nucleus is faintly detected, insufficient for a detailed spectral analysis. They conclude that NGC 4418 is probably Compton-thick and infer an intrinsic 2–10 keV luminosity of  $\sim 10^{41.2} \text{ erg/s}$  based on the assumption of one per cent reflection sensitivity for a non-stated object distance. In addition, *Suzaku* data were taken in 2006 but remain unpublished so far. The observed MIR–X-ray ratio supports the CT scenario predicting an X-ray column density of  $\log N_{\text{H}} = 25.85 \pm 0.44$ . The intrinsic 2–10 keV luminosity estimated from the MIR–X-ray correlation would be  $\log L^{\text{int}}(2-10 \text{ keV}) = 43.49 \pm 0.37$  so four orders of magnitude higher than what is observed. However, owing to the large uncertainty in the X-ray properties, the MIR–X-ray correlation can not be used to verify the AGN nature of NGC 4418.

## B4.40 NGC 4438

Machacek, Jones & Forman (2004) claim the detection of an X-ray nucleus embedded into diffuse emission in the AGN candidate NGC 4438 from *Chandra* observations, which was then verified by Flohic et al. (2006) using the same data. The derived observed X-ray luminosity is  $\log L^{\text{obs}}(2-10 \text{ keV}) = 39.02$ . On the other hand, Satyapal et al. (2005) and González-Martín et al. (2009b) claim that the nucleus is not detect again from the same data. However, their upper limit is consistent with the above value. Finally, González-Martín et al. (2009a) argue that the AGN might in fact be Compton-thick obscured based on the X-ray spectral slope, the low X-ray–[O III] ratio, and the high upper limit on the equivalent width of any Fe K $\alpha$  line. While this scenario would be consistent with the MIR–X-ray correlation putting NGC 4438 very close to it, one has to note that relatively strong circum nuclear star formation is present in this object, which might easily also dominate the subarcsecond MIR luminosity (see also Mason et al. 2012). Better high angular resolution MIR data are required to distinguish between AGN and starburst dominance.

## B4.41 NGC 4457

The LINER AGN candidate in NGC 4457 shows significant circumnuclear star formation in the MIR and X-rays but also a nuclear X-ray point source (Satyapal et al. 2005). Its observed X-ray luminosity is  $\log L^{\text{obs}}(2-10 \text{ keV}) = 38.89$  (Flohic et al. 2006; González-Martín et al. 2009b), while González-Martín et al. (2009a) argue that the source has  $\log L^{\text{int}}(2-10 \text{ keV}) = 40.57$  assuming that it is Compton-thick obscured owing to the low X-ray spectral index and X-ray–[O III] ratio. The expectations from the MIR–X-ray correlation on  $L^{\text{int}}(2-10 \text{ keV})$  and  $N_{\text{H}}$  are consistent with this scenario. However, the nuclear MIR luminosity used might still be affected or even dominated by star formation, so this result is not robust (see also Mason et al. 2012).

*B4.42 NGC 4501*

Off-nuclear emission is contaminating lower resolution X-ray data of NGC 4501 such as from *XMM-Newton* (Brightman & Nandra 2008). Furthermore, the nucleus is only barely detected at hard energies (Satyapal et al. 2005; LaMassa et al. 2011). Brightman & Nandra (2008) note that the AGN could be Compton-thick obscured. Owing to this uncertain nature of the X-ray properties, NGC 4501 is excluded from the reliable sample. The  $L^{\text{int}}(2\text{-}10\text{ keV})$  and  $N_{\text{H}}$  predictions from the MIR–X-ray diagnostics indicate indeed heavy (but Compton-thin) obscuration for the AGN.

*B4.43 NGC 4698*

According to González-Martín et al. (2009b), the *XMM-Newton* data of NGC 4698 are dominated by off nuclear emission (but see Cappi et al. 2006). The low X-ray–[O III] ratio based on *Chandra* observations indicates that the AGN might be Compton-thick obscured according to González-Martín et al. (2009a). Therefore,  $L^{\text{int}}(2\text{-}10\text{ keV})$  is highly uncertain, and NGC 4698 is excluded from the reliable sample. The MIR–X-ray correlation diagnostic does not constrain the nature of the AGN in this object.

*B4.44 NGC 4736*

NGC 4736 possesses many off-nuclear X-ray point sources and the identification of which belongs to the AGN is uncertain (González-Martín et al. 2009b). For the same reason, the *XMM-Newton* data can not be used to measure the AGN properties. Therefore, we exclude NGC 4736 from the reliable sample.

*B4.45 NGC 4785*

NGC 4785 harbours a Sy 2 candidate which most likely is CT in X-rays. A detailed analysis of the X-ray data and its relation to the high angular resolution MIR data are presented in Gandhi et al. (2015) and thus not repeated here. Owing to the large uncertainty of the X-ray properties and the non-detection in the MIR, no conclusion about the AGN nature of this object can be drawn from the MIR–X-ray correlation.

*B4.46 NGC 5005*

Based on *Chandra* and *XMM-Newton* data, González-Martín et al. (2009b) and Younes et al. (2011) claim the detection of an unobscured nucleus in NGC 5005. However, González-Martín et al. (2009a) argue that the source could be Compton-thick obscured based on the low X-ray–[O III] ratio, which is also supported by a low X-ray–[O IV] ratio. At the same time a strong nuclear starburst is present in NGC 5005, complicating the analysis of the AGN. Therefore,  $L^{\text{int}}(2\text{-}10\text{ keV})$  remains uncertain, and the object is excluded from the reliable sample. Owing to the likely star formation contamination also to the subarcsecond MIR luminosity (Mason et al. 2012; Asmus et al. 2014), the MIR–X-ray correlation does not help to constrain the AGN properties.

*B4.47 NGC 5363*

Unfortunately, no *Chandra* observations are available for the low-luminosity AGN in NGC 5363. The *XMM-Newton* data can be fit well with an unobscured power law (González-Martín et al. 2009b),

while the low X-ray spectral index and X-ray–[O III] ratio indicate Compton-thick obscuration of the nucleus (González-Martín et al. 2009a). Thus,  $L^{\text{int}}(2\text{-}10\text{ keV})$  is very uncertain, and we exclude NGC 5363 from the reliable sample. The diagnostics based on the MIR–X-ray correlation contradict the CT scenario (see also Mason et al. 2012).

*B4.48 NGC 5813*

Hernández-García et al. (2014) analysed all archival *Chandra* and *XMM-Newton* data of several epochs for the uncertain LINER AGN in NGC 5813. Bright diffuse X-ray emission renders the *XMM-Newton* data unusable to determine the AGN properties. The *Chandra* data do not show any long-term variation, and a simultaneous fit provides  $\log L^{\text{obs}}(2\text{-}10\text{ keV}) = 39.07$ . González-Martín et al. (2009a) identify NGC 5813 as Compton-thick candidate based on the low X-ray–[O III] ratio and high upper limit on the equivalent width of an Fe  $K\alpha$  line. As already mentioned in Asmus et al. (2011), the upper limit on the intrinsic X-ray luminosity through the MIR–X-ray correlation of  $\log L^{\text{int}}(2\text{-}10\text{ keV}) \leq 41.27$  does not help to distinguish the different scenarios for NGC 5813.

*B4.49 NGC 5866*

While Satyapal et al. (2005) do not detect any nuclear source with *Chandra* in NGC 5866, possibly harbouring an AGN, Flohic et al. (2006) claim the faint detection of such a source from the same data. Although too faint for spectral analysis, the estimate the observed X-ray luminosity to be  $\log L^{\text{obs}}(2\text{-}10\text{ keV}) = 38.42$ . González-Martín et al. (2009b) also detect a nuclear source, provide a similar observed luminosity, but classify NGC 5866 as non-AGN from the X-ray point of view. On the other hand, González-Martín et al. (2009a) classify it as a Compton-thick AGN candidate based on the low X-ray–[O III] ratio. The MIR–X-ray puts an upper limit on the intrinsic X-ray emission of any AGN in NGC 5866 to  $\log L^{\text{int}}(2\text{-}10\text{ keV}) = 40.74$ , which is compatible with all the above scenarios.

*B4.50 NGC 6221*

So far NGC 6221 has not been observed at 2–10 keV but it is detected in the 70 month BAT catalogue with a 14–195 keV luminosity of  $\log L^{\text{obs}}(14\text{-}195\text{ keV}) = 41.44$  (Baumgartner et al. 2013). From the MIR–X-ray correlation, we expect an intrinsic 2–10 keV luminosity of  $\log L^{\text{int}}(2\text{-}10\text{ keV}) = 41.21 \pm 0.38$ , agreeing well with the expectation from  $L^{\text{obs}}(14\text{-}195\text{ keV})$ . Without more data, we can not prove or verify the AGN nature of the nucleus of NGC 6221 however.

*B4.51 NGC 6240*

NGC 6240 is an ultra luminous infrared merger system with the best case of a double AGN found so far. The latter was discovered in X-rays by *Chandra* observations (Komossa et al. 2003). Both nuclei are heavily obscured and surrounded by star formation, which makes precise luminosity estimates difficult. However, Puccetti et al. (in prep.) utilized the new *NuSTAR* to analyse the hardest part of the X-ray emission. While *NuSTAR* can not resolve both nuclei, most of the emission should be associated with the more powerful southern nucleus, NGC 6240S. They find  $\log L^{\text{int}}(2\text{-}10\text{ keV}) = 44.09$  and Compton-thick obscuration,

which is consistent from more uncertain previous estimates based on *Chandra* (González-Martín et al. 2009b,a). The MIR–X-ray correlation predicts  $\log L^{\text{int}}(2-10 \text{ keV}) = 43.27 \pm 0.37$  and only mild Compton-thickness for NGC 6240S ( $\log N_{\text{H}} = 23.76 \pm 0.44$ ).

The northern nucleus, NGC 6240N, appears to be fainter in X-rays (Komossa et al. 2003) but is presumably highly obscured as well, as indicated by the low X-ray spectral index and infrared spectra (Risaliti et al. 2006). However, no intrinsic luminosity estimate is available and we simply use the observed luminosity from the unobscured fit of Komossa et al. (2003),  $\log L^{\text{obs}}(2-10 \text{ keV}) = 42.07$ . Here, the MIR–X-ray correlation predicts an intrinsic luminosity of  $\log L^{\text{int}}(2-10 \text{ keV}) = 42.53 \pm 0.4$  and at best only mild Compton-thickness for NGC 6240N ( $\log N_{\text{H}} = 23.44 \pm 0.47$ ).

Therefore the MIR–X-ray correlation suggests that a significant part of the *NuSTAR* detected emission might be coming from the northern nucleus. However, we can not exclude that the obscuration in both nuclei is in fact so high that the MIR is also significantly absorbed as in NGC 4945, in which case the MIR–X-ray correlation would lose its predictive power.

#### B4.52 NGC 6810

Strickland (2007) find no evidence for the presence of an AGN in NGC 6810 based on X-ray data from *XMM-Newton* and other data at other wavelengths. Brightman & Nandra (2011a), on the other hand, present an unabsorbed AGN spectral fit to the same data with an X-ray luminosity of  $\log L^{\text{int}}(2-10 \text{ keV}) = 39.99$ , unfortunately without further discussion. The nuclear MIR luminosity predicts a much higher  $\log L^{\text{int}}(2-10 \text{ keV}) = 41.71 \pm 0.39$  while assuming the observed 2–10 keV flux from Brightman & Nandra (2011a) would imply a CT obscuration ( $\log N_{\text{H}} = 24.38 \pm 0.34$ ). However, the subarcsecond MIR emission used might still be affected or dominated by star formation. With the current data it is therefore to distinguish whether indeed a CT AGN is present or the nucleus is pure star formation.

#### B4.53 NGC 7479

NGC 7479 was observed two times with *XMM-Newton* and both data sets were modelled with the emission of an absorbed (but Compton-thin) AGN (Panessa et al. 2006; Akylas & Georgantopoulos 2009). On the other hand, Brightman & Nandra (2011a) show that the AGN might in fact be Compton-thick obscured by using one of the data sets. Also Diamond-Stanic, Rieke & Rigby (2009) argue for this scenario although [OIV] emission remained undetected in NGC 7479. On the other hand, the MIR spectrum is highly obscured (Asmus et al. 2014). Conclusively,  $L^{\text{int}}(2-10 \text{ keV})$  remains highly uncertain for this source, and it has to be removed from the reliable sample. The MIR–X-ray correlation diagnostics favour the Compton-thick scenario (see also González-Martín et al. 2013).

#### B4.54 NGC 7590

NGC 7590 has a complex nuclear structure with bright star formation and probably a heavily obscured AGN. The X-ray emission of NGC 7590 is in fact dominated by off-nuclear emission Shu, Liu & Wang (2010). Therefore, only with the most recent *Chandra* data, the nucleus can possibly be isolated but remains undetected however. Shu et al. (2012) interpret this as further support for a

Compton-thick AGN. Unfortunately, the nucleus also remained undetected in the MIR at subarcsecond scales (see also Asmus et al. 2011). The estimated upper limit on the intrinsic X-ray luminosity from the MIR–X-ray correlation is  $\log L^{\text{int}}(2-10 \text{ keV}) \leq 41.37$ , which is  $\sim 2.7$  dex higher than the upper limit on the observed luminosity. Thus, we can not draw any conclusion on the nature of NGC 7590.

#### B4.55 NGC 7592W

The AGN/starburst composite nucleus of NGC 7592W has only been observed once so far in X-rays, namely with *Chandra* (Wang & Gao 2010). The S/N of the detection is too low for a spectral fitting and only the observed flux can roughly be estimated ( $\log L^{\text{obs}}(2-10 \text{ keV}) = 40.72$ ). The MIR–X-ray correlation predicts a much higher intrinsic luminosity ( $\log L^{\text{int}}(2-10 \text{ keV}) = 43.35 \pm 0.39$ ) and Compton-thick obscuration ( $\log N_{\text{H}} = 24.91 \pm 0.46$ ) assuming that the subarcsecond MIR emission is AGN dominated. This, however, remains unsure with the current minimal information on NGC 7592W.

#### B4.56 PKS 2158-380

No X-ray observations of PKS 2158-380 have been published so far. The object was only very weakly detected with *Swift*/XRT and does not allow for spectral fitting analysis. However, a strong Fe K $\alpha$  line appears to be present and indicates heavy obscuration. This is consistent with the predicted  $L^{\text{int}}(2-10 \text{ keV})$  and  $N_{\text{H}}$  from the MIR–X-ray correlation diagnostics.

#### B4.57 Superatennae S – IRAS 19254-7245S

Braito et al. (2009) managed to detect the AGN in Superatennae for the first time at energies  $> 10 \text{ keV}$  using *Suzaku*. These observations indicated that Superatennae S is mildly CT obscured. However, the two epochs of *NuSTAR* observations can be well fit with an unabsorbed power-law, leading Teng et al. (in prep.) to disfavour the CT scenario for this source. Owing to the more than two orders of magnitude differing intrinsic X-ray luminosity estimates of the two scenarios, we exclude Superatennae S from the reliable sample. The diagnostics based on the MIR–X-ray correlation are consistent with the CT scenario but it is possible that the nuclear MIR data is star formation contaminated.

#### B4.58 UGC 5101

The first detection of the AGN/starburst composite nucleus of UGC 5101 in X-rays was presented by Ptak et al. (2003) based on *Chandra* and *ASCA* observations. While they state that the nucleus is too faint for spectral analysis and consistent with a pure starburst, Imanishi (2003) find evidence for an AGN in X-rays in the same *Chandra* data combined with *XMM-Newton* data. The latter work states that the AGN dominates the emission of UGC 5101 and is heavily but not Compton-thick obscured. González-Martín et al. (2009b) and Brightman & Nandra (2011a) come to the same conclusion based on the same data ( $\log L^{\text{int}}(2-10 \text{ keV}) = 42.5$ ;  $\log N_{\text{H}} = 23.7$ ). However, González-Martín et al. (2009a) assume that the nucleus is Compton-thick obscured based on the flat X-ray spectral slope and low X-ray–[OIII] ratio with an intrinsic luminosity of  $\log L^{\text{int}}(2-10 \text{ keV}) = 43.97$ . The Compton-thick scenario would agree well with the prediction of the MIR–X-ray correlation

( $\log L^{\text{int}}(2\text{-}10\text{ keV}) = 44.07 \pm 0.38$ ;  $\log N_{\text{H}} = 24.74 \pm 0.33$ ), assuming that the nuclear subarcsecond-scale MIR emission is AGN-dominated. Unfortunately, this assumption is not verifiable with the current available MIR data. Therefore, it remains unclear whether the AGN in UGC 5101 is indeed CT obscured or not.